



저작자표시-비영리-변경금지 2.0 대한민국

이용자는 아래의 조건을 따르는 경우에 한하여 자유롭게

- 이 저작물을 복제, 배포, 전송, 전시, 공연 및 방송할 수 있습니다.

다음과 같은 조건을 따라야 합니다:



저작자표시. 귀하는 원저작자를 표시하여야 합니다.



비영리. 귀하는 이 저작물을 영리 목적으로 이용할 수 없습니다.



변경금지. 귀하는 이 저작물을 개작, 변형 또는 가공할 수 없습니다.

- 귀하는, 이 저작물의 재이용이나 배포의 경우, 이 저작물에 적용된 이용허락조건을 명확하게 나타내어야 합니다.
- 저작권자로부터 별도의 허가를 받으면 이러한 조건들은 적용되지 않습니다.

저작권법에 따른 이용자의 권리는 위의 내용에 의하여 영향을 받지 않습니다.

이것은 [이용허락규약\(Legal Code\)](#)을 이해하기 쉽게 요약한 것입니다.

[Disclaimer](#)

Ph.D. Dissertation of Oceanography

**Application of Synthetic Aperture
Radar to Coastal Oceanic
Phenomena in the Seas around
Korea**

한반도 주변해 연안 해양현상에 대한
합성개구레이더 활용

August 2016

**Graduate School of Science Education
Seoul National University
Earth Science Major**

Tae-Sung Kim

Application of Synthetic Aperture Radar to Coastal Oceanic Phenomena in the Seas around Korea

지도교수 박 경 애

이 논문을 이학박사 학위논문으로 제출함
2016 년 5 월

서울대학교 대학원
과학교육과 지구과학전공
김 태 성

김태성의 이학박사 학위논문을 인준함
2016 년 8 월

위 원 장 조 양 기 (인)

부위원장 박 경 애 (인)

위 원 김 경 렬 (인)

위 원 김 덕 진 (인)

위 원 Xiaofeng Li (인)

Abstract

In this thesis, the applicability of synthetic aperture radar (SAR) to interpretation of oceanic phenomena at the coastal regions around Korea peninsula is presented. For that, the spatial and temporal variations of SAR-derived coastal wind fields and evolution of disastrous oil spills on SAR images were analyzed in relation to atmospheric and oceanic environmental factors using in-situ measurement and satellite observations.

The SAR wind fields retrieved from the east coast of Korea in August 2007 during the upwelling period revealed a spatial distinction between near and offshore regions. Low wind speeds were associated with cold water regions with dominant coastal upwelling. Time series of in-situ measurements of both wind speed and water temperature indicated that the upwelling was induced by the wind field. SAR data at the present upwelling region showed a relatively large backscattering attenuation to SST ratio of $1.2 \text{ dB } ^\circ\text{C}^{-1}$ compared the known dependence of the water viscosity on the radar backscattering. In addition, wind speed magnitude showed a positive correlation with the difference between SST and air temperature. It implies that the low wind field from SAR was mainly induced by changes in atmospheric stability due to air-sea temperature differences.

Oil spills at the Hebei Spirit accident off the coast of Korea in the

Yellow Sea were identified using SAR data and their evolution was investigated. To quantitatively analyze the spatial and temporal variations of oil spills, objective detection methods based on adaptive thresholding and a neural network were applied. Prior to applying, the results from two methods were compared for verification. It showed good agreement enough for the estimation of the extent of oil patches and their trajectories, with the exception of negligible errors at the boundaries. Quantitative analyses presented that the detected oil slicks moved southeastward, corresponding to the prevailing wind and tidal currents, and gradually dissipated during the spill, except for an extraordinary rapid decrease in onshore regions at the initial stage. It was identified that the initial dissipation of the spilt oil was induced by strong tidal mixing in the tidal front zone from comparison with the tidal mixing index. The spatial and temporal variations of the oil slicks confirmed the influence of atmospheric and oceanic environmental factors. The overall horizontal migration of the oil spills detected from consecutive SAR images was mainly driven by Ekman drift during the winter monsoon rather than the tidal residual current.

Keywords: SAR, wind, upwelling, stability effect, oil spill, Hebei Spirit, neural network, tidal current, Ekman drift

Student Number: 2010-31101

Table of Contents

Chapter 1. Introduction	1
1.1. Study Background	1
1.2. Objectives of the Thesis	14
 Chapter 2. Data Description	 15
2.1. SAR Data	15
2.2. Other Satellite Data	21
2.2.1. Wind Data	21
2.2.2. Sea Surface Temperature Data	21
2.2.3. Ocean Color Data	22
2.3. Reanalysis Data	23
2.4. In-situ Measurements	23
2.5. Land Masking Data	26
2.6. Tidal Current Data	28
 Chapter 3. Methods	 29
3.1. SAR Wind Retrieval	29
3.2. Noise Reduction of ScanSAR Images	37
3.3. Conversion of Wind Speed to Neutral Wind	41

3.4. Estimation of Index of the Tidal Front	43
3.5. Estimation of Ekman Drift and Tidal Residual Current	45
3.6. Feature Detection Methods	46
3.6.1. Adaptive Threshold Method	47
3.6.2. Bimodal Histogram Method	50
3.6.3. Neural Network Method	54
Chapter 4. Coastal Wind Fields and Upwelling Response ..	58
4.1. Variations of Wind Fields during Coastal Upwelling	58
4.2. Stability Effect on Wind Speed	65
4.3. Biological Impact of Upwelling	70
Chapter 5. Characteristics of Objective Feature Detection ..	74
5.1. Comparison of Thresholding Methods	74
5.2. Oil Spill of the Hebei Spirit by Thresholding Method	81
5.3. Oil Spill by the Hebei Spirit by Neural Network Method ...	85
5.4. Differences by Detection Methods	88
Chapter 6. Evolution of Oil Spill at the Coastal Region	90
6.1. Temporal Evolution of the Hebei Spirit Oil Spill	90
6.2. Effect of Artificial Factor on the Evolution	96

Chapter 7. Effect of Environmental Factors on the Oil Spill	98
7.1. Effect of Tidal Mixing	98
7.2. Effect of Wind and Tidal Current	103
 Chapter 8. Summary and Conclusion	 110
 Reference	 114
 Abstract in Korean	 142

List of Tables

Table 2.1. Characteristics of ALOS PALSAR images at the eastern coast of Korea	18
Table 2.2. Characteristics of SAR images used in the Hebei Spirit oil spill detection	19
Table 2.3. Details of in-situ measurement data used in the study	25
Table 3.2. Information of the SAR image used in thresholding detection methods	77
Table 3.3. Estimated extent of the oil spill from SAR images	95

List of Figures

Fig. 1.1. (a) GOCI RGB composite image in the seas around Korea Peninsula and (b) sea surface temperatures from NOAA/AVHRR of the study area	8
Fig. 1.2. (a) Distributions of wind vector cells from QuikSCAT in the seas around Korea and (b) an example of wind field off the east coast of Korea from QuikSCAT	9
Fig. 1.3. Distributions of sea surface temperature in the East/Japan Sea during (a) weak upwelling event and (b) strong upwelling event	10
Fig. 1.4. Study area of coastal upwelling events	11
Fig. 1.5. Images of oil spilling and stranding of the Hebei Spirit	12
Fig. 1.6. (a) Contour of the water depth in the seas around the Korean Peninsula and (b) an enlarged image of the bathymetry contour in the study area	13
Fig. 2.1. ALOS PALSAR images in the eastern coast of Korea	17
Fig. 2.2. Sub-scenes of SAR images at the Hebei Spirit oil spill	20
Fig. 2.3. NRCS distributions in the western coast of Korea after land	

masking by using SRTM DEM and ASTER GDEM	27
Fig. 3.1. Flow chart for sea surface wind retrieval from L-band PALSAR data	34
Fig. 3.2. The normalized radar cross section images of ALOS PALSAR	35
Fig. 3.3. Schematic flow chart of C-band SAR wind retrieval	36
Fig. 3.4. Examples of ScanSAR mode images with band-like noises in the seas around Japan and in the Yellow Sea	39
Fig. 3.5. An example of band-like noises on ALOS PALSAR image and the NRCS image after noise reduction procedure with comparison of NRCS values before and after noise filtering and its differences	40
Fig. 3.6. Flow chart of the oil spill detection process using the adaptive threshold method.	49
Fig. 3.7. Spatial distributions of NRCS at sea areas without and with oil spill and their histograms	52
Fig. 3.8. Flow chart of the oil spill detection process using the bimodal histogram method	53
Fig. 3.9. Schematic diagram of the oil spill detection process based	

on a neural network	57
Fig. 4.1. The normalized radar cross section images of ALOS PALSAR after the noise reduction procedure	61
Fig. 4.2. Distributions of wind vectors retrieved from the PALSAR imagery	62
Fig. 4.3. Distributions of sea surface temperature from NOAA AVHRR	63
Fig. 4.4. Time series of wind vector from AWS measurement of KMA and sea surface temperature from NFRDI coastal station measurements	64
Fig. 4.5. (a) Comparison of sea surface temperature and SAR-derived wind speed along 35.6°N and (b) SAR-derived wind speeds as a function of sea surface temperature	68
Fig. 4.6. (a) Comparison of sea surface and air temperature difference and SAR-derived wind speed along 35.6°N and (b) SAR-derived wind speeds as a function of difference between sea surface temperature and air temperature	69
Fig. 4.7. Distributions of sea surface temperature and its gradient ...	72
Fig. 4.8. Distribution of monthly-averaged chlorophyll-a concentration from SeaWiFS in the East/Japan Sea in August 2007	73

Fig. 5.1. (a) Spatial distribution of ENVISAT backscattering coefficient with oil spill and (b) the analysis results of oil spill pixels using the adaptive threshold method	78
Fig. 5.2. An example of the bimodal histogram method by fitting Gaussian distribution functions with two peaks	79
Fig. 5.3. (a) Spatial distribution of backscattering coefficient with oil spill and the analysis results of oil spill pixels using (b) the adaptive threshold method and (c) the bimodal histogram method, and (d) their differences	80
Fig. 5.4. (a) NRCS distribution of an Envisat ASAR image and (b) the detection results by the adaptive threshold method	83
Fig. 5.5. Time series of in-situ wind measurements from the KMA buoy	84
Fig. 5.6. (a) The detection results from the SAR image by neural network method, and (b) the differences between the results of the two methods	87
Fig. 6.1. Oil slicks detected by (a)-(d) the adaptive threshold method and by (e)-(h) the neural network method from 11 to 15 December 2007	92
Fig. 6.2. A map of incorporated oil slicks during the period	93

Fig. 6.3. (a) Latitude points at the central location of the detected oil spill and (b) estimated extents of the oil spill	94
Fig. 7.1 Comparison of detected oil spills at the initial stage	100
Fig. 7.2. Contour of the tidal mixing parameter	101
Fig. 7.3. The vertical structures of the mean sea water temperature from KODC stations along the section of 36.9°N	102
Fig. 7.4. (a) Distribution of the tidal ellipses off the west coast of Korea and (b) time series of the tidal currents at the collision point of the Hebei Spirit	106
Fig. 7.5. (a) Distributions of the wind vector field off the west coast of Korea from QuikSCAT	107
Fig. 7.6. (a) Directional histograms of scatterometer wind vectors and (b) the relationship between the mean wind speed and the drift velocity of the oil spill.	108
Fig. 7.7. Mean tidal residual current vectors from numerical model data and mean Ekman surface drift currents from QuikSCAT winds and their histograms of the directions and speed from 10 to 15 December 2007	109

Acronyms

ALOS	Advanced Land Observing Satellite
API	American Petroleum Institute
ASAR	Advanced Synthetic Aperture Radar
ASCAT	Advanced Scatterometer
ASTER	Advanced Spaceborne Thermal Emission and Reflection Radiometer
AVHRR	Advanced Very High Resolution Radiometer
AWS	Automatic Weather Station
BVW	Bourassa-Vincent-Wood Model
CF	Calibration Factor
CMOD	C-band Model for Wind Retrieval
DAAC	Distributed Active Archive Center
DEM	Digital Elevation Model
DN	Digital Number
ECMWF	European Center for Medium-range Weather Forecasts
EJS	The East/Japan Sea

ENVISAT	Environmental Satellite
GDEM	Global Digital Elevation Model
GMF	Geophysical Model Function
GSFC	Goddard Space Flight Center
JPL	Jet Propulsion Laboratory
KMA	Korea Meteorological Administration
KODC	Korean Oceanographic Data Center
LKB	Liu-Katsaros-Businger
MABL	Marine Atmospheric Boundary Layer
MCSST	Multi-Channel Sea Surface Temperature
METI	Ministry of Economy, Trade, and Industry of Japan
NASA	National Aeronautics and Space Administration
NDBC	National Data Buoy Center
NFRDI	National Fisheries Research and Development Institute
NIR	Near Infrared
NOAA	National Oceanic and Atmospheric Administration
NRCS	Normalized Radar Cross Section

NSCAT	NASA Scatterometer
PALSAR	Phased Array type L-band Synthetic Aperture Radar
PODAAC	Physical Oceanography Distributed Active Archive Center
PR	Polarization Ratio
QuikSCAT	Quick Scatterometer
RIO/SNU	Research Institute of Oceanography, Seoul National University
SAR	Synthetic Aperture Radar
SeaWiFS	Sea-viewing Wide Field-of-view Sensor
SMI	Standard Mapped Images
SRTM	Shuttle Radar Topography Mission
SST	Sea Surface Temperature
UTC	Universal Time Coordinated

Chapter 1. Introduction

1.1. Study Background

The seas around Korea have been known for unique rapid variabilities. Its coastal regions have shown a variety of oceanic phenomena and distinctive changes in sea water temperatures due to upwelling, eddies, fronts, tides, topographic effects, and frequently-passing atmospheric systems. The eastern coast of Korea in the East/Japan Sea (EJS), leading to be referred to as a miniature ocean (Kim et al., 2001), is one of the places where seasonal coastal upwelling prevails in the Northwest Pacific including the Yellow Sea, the EJS, and the East China Sea (Fig. 1.1). On the other hand, the western coast of Korea in the Yellow Sea is also known for its strong tidal currents and seasonal wind variations, such as summer and winter monsoons. A variety of oceanic phenomena related to its shallow bathymetry and tidal forcing ubiquitously appears along the western coast of Korea.

Basically, satellite sea surface temperature (SST) and wind fields from scatterometer have been widely utilized to demonstrate wind-induced oceanic responses and their dynamics in the open ocean (McClain et al., 1984; Bisagni and Sano, 1993; Zheng et al., 1998; Fragiaco and Parmiggiani, 2002; Park et al., 2006). Wind vector measurements from space have provided us with an opportunity to understand oceanographic phenomena and their scientific processes. Since wind fields over ocean have been obtained

from scatterometer since early 1990's, it has contributed to a variety of researches and applications, especially for climate changes and environmental changes. However, the scatterometer dataset has the limitation in the interpretation of small-scale phenomena at the coastal regions due to its low resolution of 25 km. Fig. 1.2 shows the coverage and observed wind field of the Quick Scatterometer (QuikSCAT) wind measurements of the seas around Korea. As shown, it is unavailable to derive the spatial patterns of wind fields near the coast from scatterometer measurements.

Synthetic Aperture Radar (SAR) is capable of high-resolution imaging, so that the detailed distribution of wind vectors, which is hard to be obtained from scatterometers, can be retrieved even for the coastal regions. It sends a chirp pulse of microwaves mostly at X-, C-, or L-bands to the sea surface and receives a backscattering cross section transmitted back to the sensor in space. The backscattering coefficient can be used to retrieve diverse oceanic variables. Overall, these SAR sensor satellite systems can measure 50-500 km² regions with spatial resolutions of about 1-100 m. Furthermore, it offers a capacity of all-weather imaging for the ocean surface irrespective of atmospheric condition, except for extreme events related to heavy rainfall. These unique imaging availabilities of SAR make it possible to observe various oceanic features such as waves (Beal et al., 1986; Dobson and Vachon, 1994; Kim, 1999), currents (Lyzenga and Marmorino, 1998; Romeiser et al., 2002; Kang and Lee, 2007), internal waves (Gasparovic et al., 1988; da Silva et al., 1997; Liu et al., 2014) and near-coastal and finer-scale wind fields to investigate the spatial variability of wind field (Wackerman et al., 1996; Kerbaol et al., 1998; Vandemark et al., 1998;

Lehner et al., 2000; Friedman et al., 2001; Monaldo et al., 2002; Horstmann et al., 2005; Kim, 2009; Kim et al., 2010; Shimada, 2010; Isoguchi et al., 2011; Kim et al., 2012). SAR-derived wind fields are now being used in various applications such as coastal environment monitoring (Korsbakken et al., 1997; Choisnard et al., 2003; Moon et al., 2010), assimilation of ocean circulation models (Young et al., 2000; Kawamura et al., 2002; Zabeline et al., 2011), and mapping global wind power (Furevik and Espedal, 2002; Hasager et al., 2004; Christiansen et al., 2006; Monaldo et al., 2014). Especially, when considering the high variability of oceanic phenomena in the seas around Korea, the usage of high-resolution SAR data in investigation of its spatial and temporal variations can contribute to enhance our understanding of fine-scale oceanic phenomena at the coastal region.

In the EJS, for example, cold water masses induced by coastal upwelling frequently appear along the east coast of Korea in summertime as shown in Fig. 1.3 (Lee, 1983; Lee and Na, 1985). These coastal upwelling commonly occurs in regions where steady wind blows parallel to the coastline (Smith, 1968). Worldwide, the west coast of United States, the coast of Peru and Chile, the northwest and southwest coasts of Africa, as well as Iberian coast are all known to be upwelling-favorable places (Bakun, 1990). Upwelling, as one of the most important coastal phenomena, leads to significant changes in water mass structure and primary production in the upper layer. Due to its oceanographic impact and close relationship to human activity, many researchers have attempted to monitor these upwelling processes and identify their mechanisms (Van Camp et al., 1991; Nykjaer and Van Camp, 1994; Thomas et al., 2001; Marín et al., 2003; Barth and Wheeler, 2005; Santos

et al., 2005; Pradhan et al., 2006; Lathuilière et al., 2008).

Much of the previous literature has covered the appearance of cold water masses induced by coastal upwelling along the east coast of Korea and its responses (An, 1974; Lee, 1978; Lee et al., 1998; Suh et al., 2001; Kim et al., 2003; Lee et al., 2003; Kim and Kim, 2008; Lee et al., 2009; Kim et al., 2010; Lee, 2011). Unlike the common upwelling events, an unprecedented coastal upwelling event occurred recently along the east coast of Korea over 37°N, which was much farther north than the usual upwelling sites (Park and Kim, 2010). Park and Kim (2010) demonstrated that the existence of this unusual cold water mass was highly correlated with the behavior of the Northwest Pacific High which is a subtropical high pressure in the northwest Pacific controlling the East Asian summer monsoon system and can be explained in terms of long-term large-scale variations due to global warming.

To investigate the presence of coastal upwelling and its dynamics, some of previous researches has been attempted to utilize SAR data (Hsu et al., 1995; Clemente-Colón and Yan, 1999; Clemente-Colón, 2001; Svejksky and Shandley, 2001; Li et al., 2009). Those demonstrated that upwelling regions are associated with low backscattering on SAR images by comparing SAR observations with SST measurements. However, upwelling investigations using SAR data have been very limited at the specific regions due to lack of coastal wind fields, in-situ measurement and coincident thermal and other satellite observations. For the reason, none of studies has paid attention to utilize SAR data for detection and analysis of coastal upwelling in the EJS so far. In this study, we focused on the modification of SAR-derived coastal

wind data in relation to upwelling in the east coast of Korea and investigated its mechanism using SAR data, in-situ measurement, and other satellite observations (Fig. 1.4).

On the other hand, the coastal regions in the seas around Korea are frequently covered with clouds and even severe fogs appeared occasionally (Cho et al., 2000). As mentioned, SAR is capable of imaging the ocean surface irrespective of atmospheric clouds and moisture, with the exception of extreme events (Kim et al., 2010; Li et al., 2012). In this respect, monitoring of evolution of oil spills with devastating hazards along coastal regions is regarded as one of the most essential SAR oceanic application.

Oil spills on the sea surface have increasingly occurred, leading to devastating environmental hazards in the ocean. Spills have significantly influenced the biological ecology on short-term and long-term scales in local seas. Many endeavors are required for the removal and cleanup of oil spill contamination from soil and marine ecosystems. Aerial observations and satellite images monitor oil spills using diverse methodologies for detection. Very recently, a few methods were developed that use satellite optical images and microwave images. SAR images are among the most representative images to identify oil spills regardless of atmospheric conditions, such as clouds, fog, other meteorological phenomena, and sun illumination.

An unprecedented oil spill accident occurred due to a collision (126.05°E, 36.86°N) between the crude oil tanker Hebei Spirit and a towed crane barge in an off-coastal region off the Korean coast at 22:15 (Universal Time Coordinated, UTC) on 6 December 2007. Due to the collision, a

considerable amount of three types of crude oil immediately began to leak from three damaged tanks: Upper Zakum crude (density: 0.856 g cm^{-3} , American Petroleum Institute (API) gravity: 33.7); Kuwait export crude (0.868 g cm^{-3} , API gravity: 30.9); and Iranian heavy crude (0.870 g cm^{-3} , API gravity: 31.1). The oil leaks lasted for about one and half days until 14:40 UTC on 8 December 2007. As a result, a total of approximately 10,900 tons of crude oil spilled into the sea (MLTM, 2008). The oil slick rapidly spread to the southeast from the area of the collision and caused considerable damage because of the extensive contamination of offshore and coastal regions along the western coast of Korea due to the strong winds and current at that time (Fig. 1.5). It was evaluated as the largest and worst oil spill in the seas around Korea.

Previous research attempted to monitor these types of widely dispersed oil spills and their variations by utilizing SAR images (e.g., Yang et al., 2009; Kim et al., 2010; Kim et al., 2014). Some of the studies used both spaceborne optical data and SAR images to simulate the dispersion of the oil slicks through numerical model experiments (Yang et al., 2009; Kim et al., 2014). In addition, theoretical damping ratios for the detection of oil slicks were applied to the Hebei Spirit incident for a brief overview (Kim et al., 2010). However, all of the previous studies performed for the Hebei Spirit used subjective methods that were ultimately based on visual inspections, although they exploited a theoretical simulation to determine a damping ratio for the detection (Kim et al., 2010). Some of the studies attempted to demonstrate certain aspects of the evolution of the Hebei Spirit oil spill with time, but no studies clarified the temporal variations of the oil

spill and its scientifically potential causes by considering specific atmospheric and oceanic conditions in the study region.

The western coast of Korea in the Yellow Sea shows various oceanic phenomena related to tidal currents and shallow water depths, with a mean value of approximately 44 m (Fig. 1.6). The specific coastal region near Taean, where the Hebei Spirit oil spill occurred, is one of the spots where dominant mixing prevails, depending mainly on semi-diurnal tides. Under these circumstances, the spilled oil droplets can be quickly scattered or considerably dispersed. For example, in the case of the Braer oil spill in 1993 off the Shetland Coast, it was reported that a substantial volume of oil as much as 44% was infused into the water column by the effect of tidal streams (Turrell, 1994; Turrell, 1995). Thus, we hypothesized that the oil spill might evolve by the effects of the prevailing wind field and tidal mixing at the shallow regions of this particular region. None of the previous studies addressed the relationship between the abrupt reduction of oil spills over a short period of time at this region and the potential causes that depict the temporal evolution of oil spills from a series of SAR images based on an objective method. In this study, we investigated the spatial and temporal variations of oil spills and its mechanism by analyzing the objectively detected results from SAR images with environmental parameters.

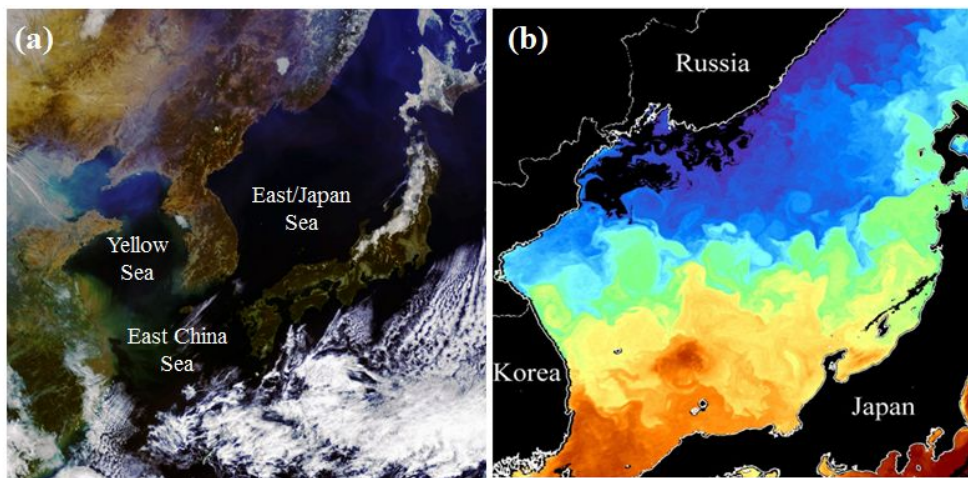


Fig. 1.1. (a) GOCI RGB composite image in the seas around Korea Peninsula on 5 April 2011 and (b) sea surface temperatures from NOAA/AVHRR of the study area on the same date of (a).

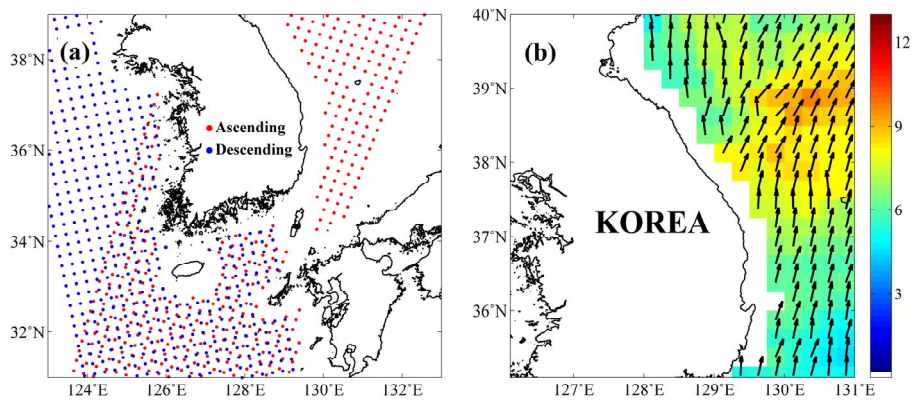


Fig. 1.2. (a) Distributions of wind vector cells from QuikSCAT in the seas around Korea, where the red and blue circles represent those from ascending and descending modes for a day, respectively, and (b) an example of wind field off the east coast of Korea from QuikSCAT, where the background color and arrow indicate the magnitude of wind speed and the direction of wind vector, respectively.

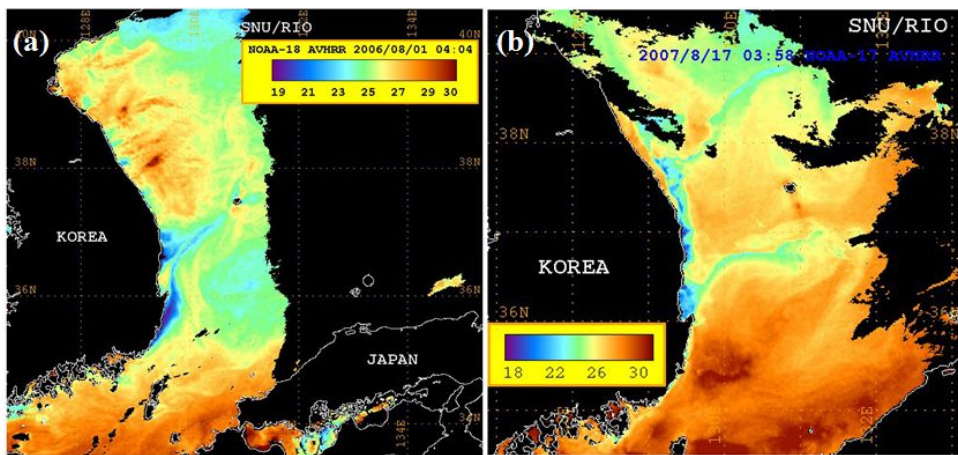


Fig. 1.3. Distributions of sea surface temperature in the East/Japan Sea during (a) weak upwelling event (1 August 2006) and (b) strong upwelling event (17 August 2007) [Park and Kim, 2010].

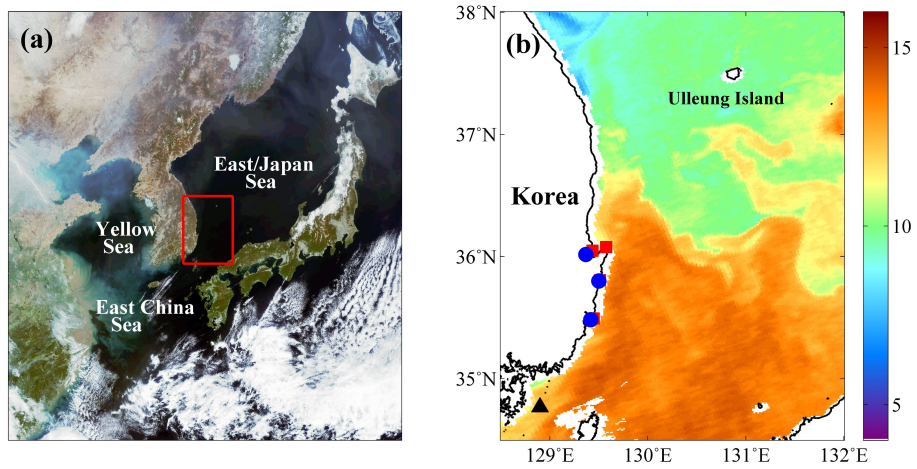


Fig. 1.4. Study area of coastal upwelling events. (a) GOCI image in the seas around Korea Peninsula on 5 April 2011 and (b) SSTs from NOAA/AVHRR of the study area on the same date of (a), where the symbols of rectangle (red), circle (blue), and triangle (black) indicate the locations of NFRDI coastal station, AWS station of Korea Meteorological Administration (KMA), and oceanic buoy station of KMA, respectively.



Fig. 1.5. Images of (a-b) oil spilling of the Hebei Spirit, (c) oil stranding on beach, and (d) spreading on sea surface [MLTM, 2008].

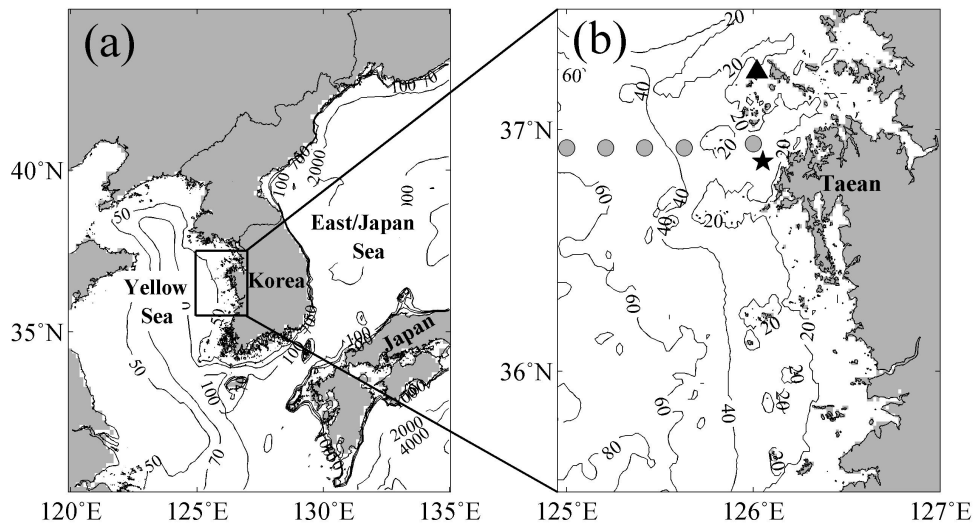


Fig. 1.6. (a) Contour of the water depth (m) in the seas around the Korean Peninsula, where the black box indicates the study area, and (b) an enlarged image of the bathymetry contour in the study area, where the black star symbol and the black triangle symbol indicate the collision point of the Hebei Spirit and the location of the KMA buoy station, respectively. Gray circles along the section at 36.9°N indicate the stations where the in-situ measurements of the KODC were taken.

1.2. Objectives of the Thesis

In this study, the applicability of SAR to interpretation of coastal oceanic features was investigated. The utilization of SAR data gives opportunities to identify the characteristics of oceanic dynamics related to air-sea interaction at coastal areas. At first, the modification of SAR-derived coastal wind fields and its mechanisms were analyzed in relation to upwelling in the east coast of Korea using in-situ measurement and satellite observations. This study attempted to identify the causes of spatial distinctions among wind fields along the coastal region in the EJS, as well as the physical and biological impacts of upwelling activity through multi-satellite observations.

Furthermore, the evolution of a disastrous oil spill was demonstrated by utilizing SAR imagery. Detection techniques for oil spills have long been in development, with most of the previous literature relying upon the thresholding method, due to its simplicity in terms of calculation. However, the threshold determined with this method tends to be subjective in most of cases. In this study, we introduced unsupervised methods based on neural network and then compared their results with those from the thresholding methods. The influence of atmospheric and oceanic factors on the spatial and temporal variations of the oil slicks were analyzed as well.

Chapter 2. Data Description

2.1. SAR Data

For the investigation of oceanic features on the SAR imagery at the coastal region in the seas around Korea, various kinds of SAR images from Environmental Satellite's (ENVISAT) Advanced Synthetic Aperture Radar (ASAR), Advanced Land Observing Satellite (ALOS) Phased Array type L-band Synthetic Aperture Radar (PALSAR), and Radarsat-1 were utilized. All of these SAR images were preprocessed to extract parameters including incidence angles, geodetic coordinates, and normalized radar cross section (NRCS) values according to their own procedures of each SAR instruments.

To derive coastal winds during upwelling events, ALOS PALSAR images were used (Fig. 2.1). Details of PALSAR images for this study were summarized in Table 2.1. We utilized PALSAR images along the east coast of Korea from the summer of 2007. These PALSAR data at L-band (23.6-cm wavelength) with HH-polarization (horizontally transmitted and horizontally received) were obtained in ScanSAR mode with a swath of 370 km and a spatial resolution of 100 m. The looking angle of the PALSAR images ranges from 17.5° to 43.2° . The PALSAR images were acquired at 02h 00m on 6 August 2007 and at 02h 02m (UTC) on 26 August 2007, with the centers of the images being located at 128.97°E , 35.50°N , and 128.43°E , 35.51°N , respectively.

In addition, to illustrate the evolution of the oil that leaked from the

Hebei Spirit, we collected a number of SAR images from ENVISAT ASAR, ALOS PALSAR, and Radarsat-1. The details of the SAR images are summarized in Table 2.2. We utilized SAR images off the western coast of Korea captured from 9 to 15 December 2007. For the Hebei Spirit oil spill case, all of the SAR images were acquired in a single-polarized state. While most of the images were acquired with HH-polarization, the ENVISAT images were acquired with VV-polarization (vertically transmitted and vertically received). Fig. 2.2 shows the distributions of the NRCS values in sub-scenes from the SAR images used in this study. These SAR data were obtained at the C- or L-band (5.6- and 23.6-cm wavelength, respectively) with different polarized states in various imaging modes. Depending on the image acquisition mode, the spatial resolutions and swath widths of the SAR images ranged from a few meters (less than 10 m) to 100 m at most and from 70 km to more than 400 km, respectively.

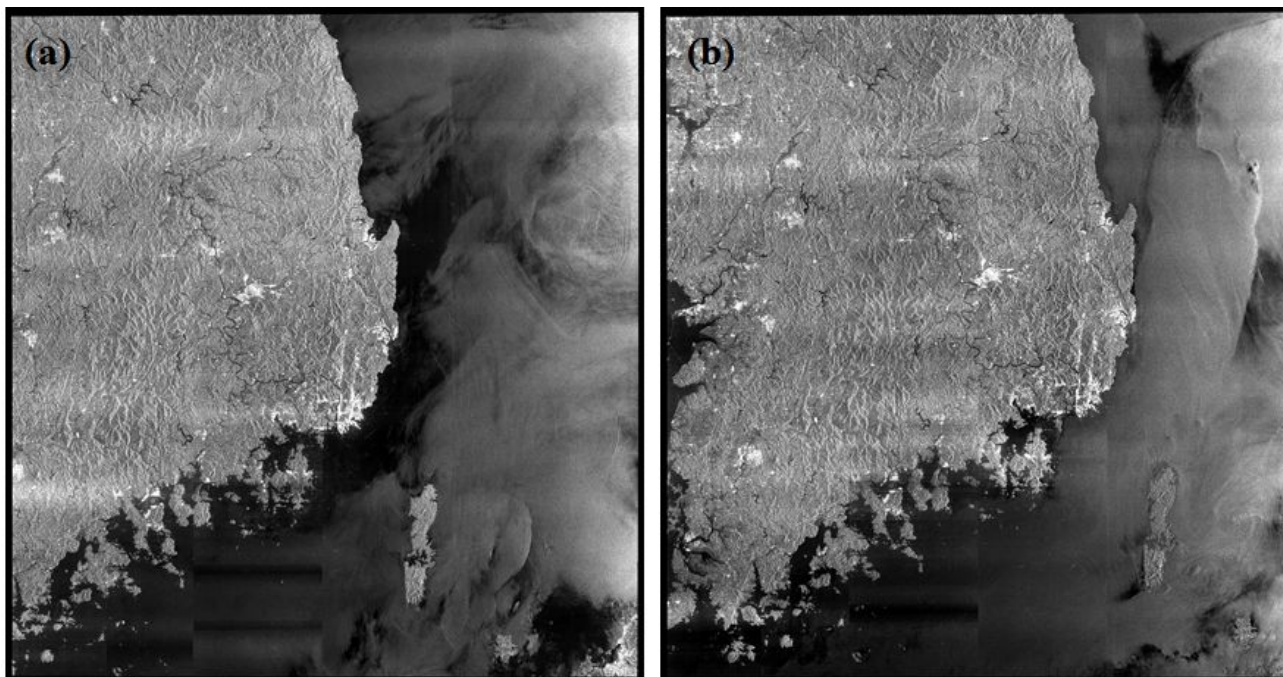


Fig. 2.1. ALOS PALSAR images in the eastern coast of Korea acquired on (a) 6 August 2007 and (b) 23 August 2007.

Table 2.1. Characteristics of ALOS PALSAR images at the eastern coast of Korea

Parameter	ALOS PALSAR Image	
	Image A	Image B
Frequency (MHz)	1270 (L-band)	
Polarization state	HH-polarized	
Swath width (km) × Azimuthal range (km)	370 ×390	
Resolution (m)	100 ×100	
Look angle (deg)	17.5° to 43.2°	17.5° to 43.2°
Acquired time	02h 00m 11s, 6 Aug 2007 (UTC)	02h 02m 17s, 23 Aug 2007 (UTC)
Central location	128.97°E, 35.50°N	128.43°E, 35.51°N

Table 2.2. Characteristics of SAR images used in the Hebei Spirit oil spill detection

Satellite /Sensor	ALOS PALSAR	ENVISAT ASAR	Radarsat-1	ALOS PALSAR	ENVISAT ASAR	ALOS PALSAR	Radarsat-1
Acquisition time	2007.12.09 14h 02m	2007.12.11 01h 40m	2007.12.11 09h 31m	2007.12.11 13h 45m	2007.12.14 01h 45m	2007.12.15 02h 09m	2007.12.15 21h 30m
Frequency (GHz)	1.27 (L-band)	5.33 (C-band)	5.3 (C-band)	1.27 (L-band)	5.33 (C-band)	1.27 (L-band)	5.3 (C-band)
Polarization	HH	VV	HH	HH	VV	HH	HH
Width (km) × Length (km)	70 × 60	420 × 450	160 × 160	65 × 70	420 × 610	370 × 390	130 × 145
Resolution (m × m)	6.25 × 6.25	75 × 75	4.9 × 11.5	12.5 × 12.5	75 × 75	100 × 100	5.3 × 11.5
Incidence angles (deg)	36.4 - 40.7	16.0 - 42.8	29.8 - 39.3	7.6 - 13.2	15.9 - 42.8	17.6 - 43.2	38.9 - 45.4
Central location	125.98°E 36.64°N	127.09°E 36.87°N	127.87°E 33.63°N	126.05°E 36.48°N	127.83°E 33.52°N	126.85°E 37.98°N	126.19°E 36.32°N

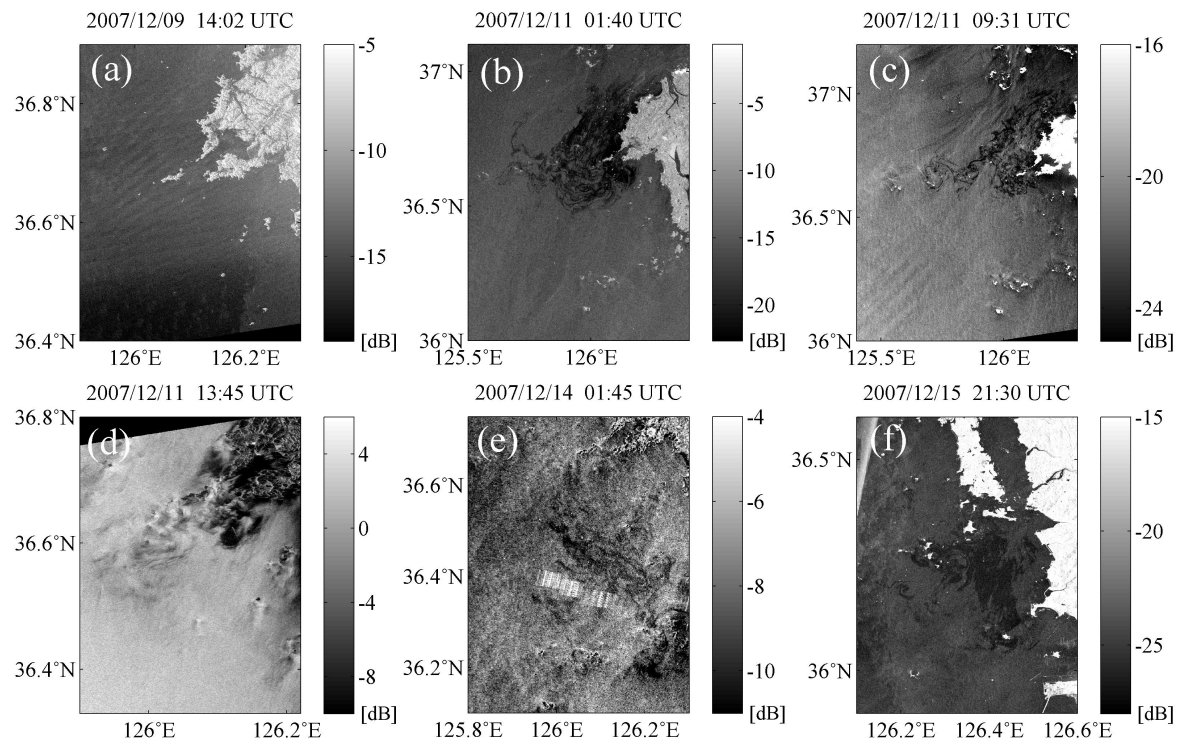


Fig. 2.2. Sub-scenes of SAR images at the Hebei Spirit oil spill on (a) 9 December 2007 (PALSAR), (b) 11 December 2007 (ASAR), (c) 11 December 2007 (Radarsat-1), (d) 11 December 2007 (PALSAR), (e) 14 December 2007 (ASAR), and (f) 15 December 2007 (Radarsat-1).

2.2. Other Satellite Data

2.2.1. Wind Data

Data of the SeaWinds scatterometer onboard the QuikSCAT satellite were utilized to investigate the spatial distribution of sea surface wind vectors during the time of the Hebei Spirit oil spill. The QuikSCAT was launched in 1999 to minimize the gap created by the loss of the National Aeronautics and Space Administration (NASA) Scatterometer (NSCAT). Using a rotating dish antenna radiating microwave pulses at a frequency of 13.4 GHz (Ku-band) in a circular pattern, it observes 1800 km swath during each orbit. Until the end of the mission in 2009 due to an age-related mechanical failure, the QuikSCAT provides approximately 90% of the global ocean surface wind field at least two times a day, with a spatial resolution of 25 km over 10 years. In this study, we used the level-3 daily gridded ocean wind vectors obtained through the Physical Oceanography Distributed Active Archive Center (PO.DAAC) at the Jet Propulsion Laboratory (JPL).

2.2.2. Sea Surface Temperature Data

High resolution SST images from the National Oceanic and Atmospheric Administration (NOAA) Advanced Very High Resolution Radiometer (AVHRR) were utilized to investigate the spatial distribution of sea surface temperature. The AVHRR is a cross-track scanning imager carried on the NOAA's polar-orbiting satellites for measuring the reflectance of the Earth

surface with multi spectral bands. The latest version of the instrument, AVHRR/3, having 6 channels with a resolution of 1.1 km observes the surface of the Earth twice per day with a wide swath of approximately 2500 km. Although depending on the region and period of interest, the accuracy of the AVHRR-derived SSTs is generally known to be below 1 °C (Strong and McClain, 1984; McClain, 1989; Li et al., 2001; Park et al., 2015). We acquired the AVHRR data of NOAA-16, 17, and 18 from the Research Institute of Oceanography (RIO), Seoul National University (SNU), and derived SSTs by using a split window Multi-Channel SST (MCSST) algorithm (McClain et al., 1985).

2.2.3. Ocean Color Data

Sea-viewing Wide Field-of-view Sensor (SeaWiFS) chlorophyll-a concentration data were used in order to investigate the biological impact of coastal upwelling. SeaWiFS is an optical scanner which was designed primarily to monitor the concentration of marine phytoplankton from space. It observes approximately 90% of the ocean surface every two days with eight bands including six visible bands, which range from 412 nm to 670 nm, and two near infrared (NIR) bands of 765 nm and 865 nm. We utilized the level-3 Standard Mapped Images (SMI) obtained from the NASA Goddard Space Flight Center (GSFC) Distributed Active Archive Center (DAAC). The level-3 SeaWiFS chlorophyll-a concentration data have a spatial resolution of 9×9 km and are composited of level-2 data for a day, 8 days, a month, or a year (Hooker et al., 1992, Campbell et al., 1995). Due to lack of data, we used monthly composited SMI data.

2.3. Reanalysis Data

For the determination of wind direction, reanalysis data from the European Center for Medium-range Weather Forecasts (ECMWF) were obtained. The reanalysis winds were near-surface winds at 10 m with a spatial resolution of $0.75^\circ \times 0.75^\circ$. Time differences between the model winds and SAR images were within 2 hours.

2.4. In-situ Measurements

In order to assess the accuracy of SAR-derived wind fields and investigate the upwelling response, in-situ measurements from a meteorological buoy station belonging to Korea Meteorological Administration (KMA), as well as coastal stations of the National Fisheries Research and Development Institute (NFRDI), were used (Fig. 1.4b). While satellite-derived wind speeds were referenced to a height of 10 m, the wind data of KMA buoy were measured at a height of 4.3 m which is less than 10 m. For precise comparison with SAR winds, the measured wind speeds of buoy were converted to 10-m neutral wind by using a wind profile model which includes air-sea stability effects (Brown and Liu, 1982; Businger and Shaw, 1984; Liu, 1984; Kara et al., 2008). Since the oceanic buoy stations were far from the coastal regions where upwelling events

occurred, we also relied upon wind measurements from ground-based Automatic Weather Stations (AWSs) of the KMA which were located close to the upwelling regions.

For the quantitative analysis of effect of environmental factors on oil spill, additional in-situ measurement data from the nearest KMA meteorological buoy station at the collision point and serial oceanographic observations by the Korean Oceanographic Data Center (KODC) of the NFRDI were used as well. Details of in-situ measurement dataset were summarized in Table 2.3. KODC serial oceanographic observations were conducted bimonthly since 1961 to measure oceanic parameters, including the water temperature, salinity, and dissolved oxygen at predetermined depths at each of the 207 fixed stations along 25 lines. In this study, we used the measurements from the KODC data of line number 307 to identify the vertical structure of the sea water temperature distribution in the regions affected by the oil spill. The locations of the KMA buoy stations and the KODC serial observation stations are marked by the black triangle and the gray circle, respectively, in Fig. 1.6b.

Table 2.3. Details of in-situ measurement data used in the study

	Ocean buoy	Ground-based AWS	Coastal station	Serial observations
Variables	Wind speed Wind direction SST Humidity	Wind speed Wind direction Air temperature	Air temperature SST	Water temperature
Temporal resolution	1 hour	10 minutes	1 day	2 months
Location	128.90°E, 34.76°N 126.02°E, 37.24°N	129.50°E, 35.78°N 129.36°E, 36.01°N 129.43°E, 35.48°N	129.43°E, 36.04°N 129.57°E, 36.07°N 129.51°E, 35.80°N 129.44°E, 35.49°N	36.9°N (Line No. 307)
Agency	KMA	KMA	NFRDI	NFRDI

2.5. Land Masking Data

Advanced Spaceborne Thermal Emission and Reflection Radiometer (ASTER) Global Digital Elevation Model (GDEM) data that were jointly generated and distributed by the Ministry of Economy, Trade, and Industry (METI) of Japan and by the NASA of USA were used to mask the land areas. In general, digital elevation model (DEM) data from the Shuttle Radar Topography Mission (SRTM) in 2000 is commonly used in the field, as it has a sufficient resolution of 3 arc-seconds (approximately 90 m) for land masking in high-resolution SAR images. However, the preprocessed results using SRTM DEM data present some large discrepancies, especially along the western coast of Korea, due to extensive land-fill projects by the Korean government that have recently reclaimed land from tidal wetlands (Fig. 2.3). For this reason, ASTER GDEM data with a high spatial resolution of 1 arc-second (approximately 30 m), initially released in 2009 and recently updated in 2011, was used in this study.

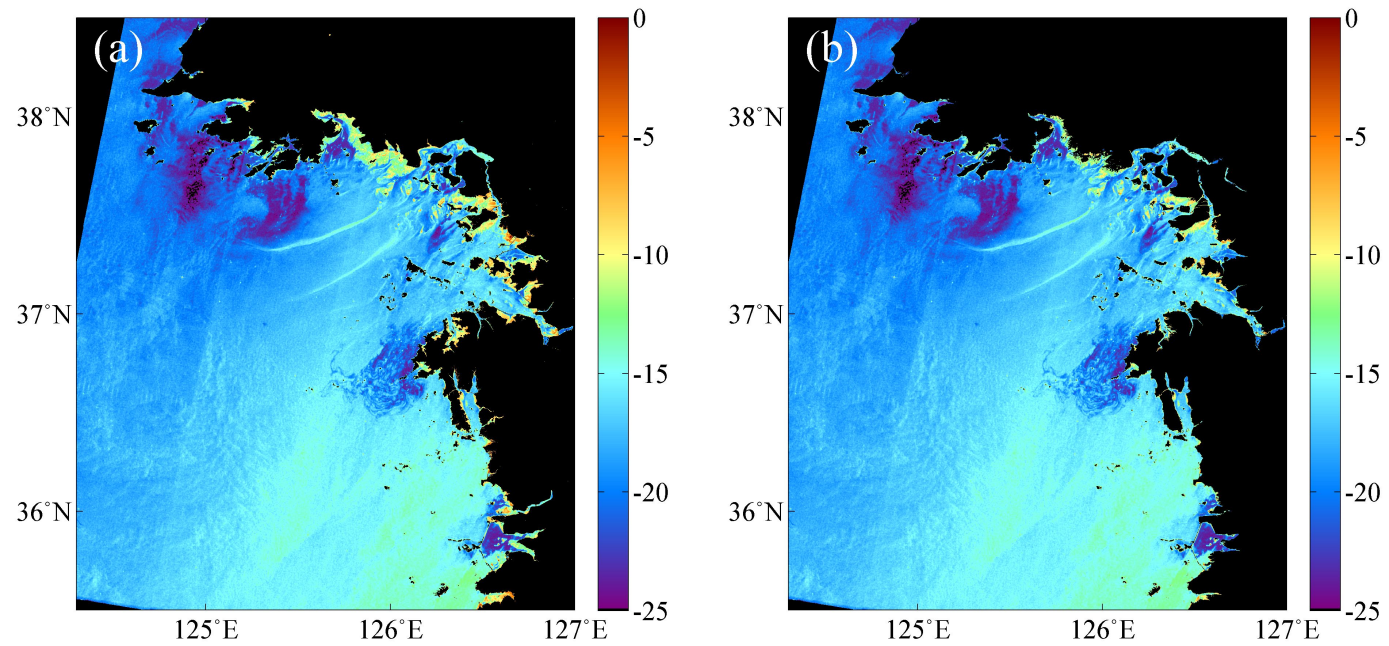


Fig. 2.3. NRCS distributions in the western coast of Korea after land masking by using (a) SRTM DEM data and (b) ASTER GDEM data.

2.6. Tidal Current Data

The coastal region near the Taean peninsula is remarkable for the complexity of its tidal patterns, with a large tidal range. To obtain information on the distribution of tidal currents in the study area, we performed a tidal model based on the Environmental Fluid Dynamics Code (Hamrick, 1996) with a grid spacing of 1 km. For the open boundary condition of the tidal simulation, results from the Nao99jb model (Matsumoto et al., 2000) were used for 15 tidal constituents (M2, S2, N2, K2, 2N2, μ 2, ν 2, L2, K1, O1, P1, Q1, OO1, M1, and J1) with a horizontal resolution of $1/12^\circ$. The index of the tidal front and the tidal residual currents in the study area were derived from the estimated parameters.

Chapter 3. Methods

3.1. SAR Wind Retrieval

Fig. 3.1 presents the schematic flow chart of L-band SAR wind retrieval from PALSAR images. Before applying the SAR wind retrieval algorithm, SAR data were preprocessed to extract the NRCS, incidence angles, and ancillary information such as the geolocation of pixels and radiometric parameters. For the PALSAR level 1.5 data, NRCS values were derived from a pixel value (digital number, DN) according to the following formula;

$$NRCS = 10\log_{10}\langle DN^2 \rangle + CF, \quad (3.1)$$

where $\langle \rangle$ indicates the ensemble averaging of a pixel value, and CF is a calibration factor. In the case of the PALSAR data used in this study, the calibration factor CF was given a value of -83 dB. Fig. 3.2 shows the distributions of the calculated NRCS from the PALSAR images during the coastal upwelling in 2007.

The SAR wind retrieval model requires the input of wind directions prior to the estimation of wind speed. If wind-induced streaks are apparent on the image, then wind direction can be directly estimated from the SAR image using 2-D Fourier transform spectrum analysis (Wackerman et al., 1996; Vachon and Dobson, 2000). In this case, although the wind direction can be

extracted directly from the SAR imagery, there is still a problem related to 180° ambiguity. Otherwise, the directions can be obtained from other external data such as in-situ buoy measurements, scatterometer wind data, or numerical model products. In this study, wind directions were obtained from ECMWF reanalysis wind datasets due to the lack of streaks (Fig. 2.1).

In order to derive wind speed from SAR data, the model functions were used by considering NRCS and wind speed, incidence angle, polarization state, and relative wind direction which presents the angle between the radar look direction and the local wind direction. We used the robust L-band SAR geophysical model function (GMF) developed by Isoguchi and Shimada (2009) that has been widely used for L-band SAR wind retrieval (Leite et al., 2010; Isoguchi et al., 2011; Kim et al., 2012).

The L-band HH GMF algorithm has been developed by comparison of the PALSAR observations with Advanced Scatterometer (ASCAT) winds, ECMWF reanalysis data, and National Data Buoy Center (NDBC) measurements. The functional form of relationship between NRCS and wind vector is as follows:

$$\sigma_0 = A_0(v, \theta)(1 + A_1(v, \theta)\cos\phi + A_2(v, \theta)\cos 2\phi), \quad (3.2)$$

$$A_0 = 10^{(a_0 + a_1W + a_2W^2 + a_3W^3)/10}, \quad (3.3)$$

$$A_1 = c_{13} + c_{14}x + c_{15}x^2 + (c_{16} + c_{17}x + c_{18}x^2)v, \quad (3.4)$$

$$A_2 = \frac{b_0 + b_1 v + b_2 v^2}{1 + \exp(b_3 + b_4 v)}, \quad (3.5)$$

where σ_0 is the NRCS, v is the wind speed in 10-m height, θ is the incidence angle, and ϕ is the direction of viewing relative to the wind direction which is $\phi = 0^\circ$ when viewing upwind. The A_n and B_n are functions of the wind speed term $W = 10 \log_{10} v$ and the incidence angle term $x = (\theta - 30)/15$. The coefficients C_n are derived from the match-up dataset (Isoguchi and Shimada, 2009).

To input the environmental parameters using the neural network method, the wind speeds were derived from C-band SAR images as well. Fig. 3.3 presents a schematic flow chart of the C-band SAR wind retrieval process. Among the GMFs for the C-band wind retrieval, the C-band Model version 5 (CMOD5) algorithm (Hersbach et al., 2007) was used in this study. The CMOD5 algorithm was developed for more precise C-band wind retrieval based on the CMOD4 GMF (Stoffelen and Anderson, 1997) by correcting an inherent deficiency in which high wind speeds are underestimated (Hersbach et al., 2007). The functional form of the relationship between the NRCS and the wind vector is as follows:

$$\sigma_0 = A_0(v, \theta)(1 + A_1(v, \theta)\cos\phi + A_2(v, \theta)\cos 2\phi)^{1.6}, \quad (3.6)$$

$$A_0 = 10^{a_0 + a_1 v} f(a_2 v, s_0), \quad (3.7)$$

$$f(s, s_0) = \begin{cases} (s/s_0)^\alpha g(s_0), & s < s_0 \\ g(s), & s \geq s_0 \end{cases}, \quad (3.8)$$

where A_n and f are respectively functions of the wind speed and the incidence angle term, where $g(s) = 1/(1 + \exp(-s))$ and $\alpha = s_0(1 - g(s_0))$. The coefficients a_n depend only on the incidence angle.

Since the CMOD5 GMF was developed for C-band VV-polarized data, NRCSs acquired at HH polarization should be converted to VV-polarized values using a polarization ratio (PR). Generally, a PR is determined as

$$PR = \frac{(1 + \alpha \tan^2 \theta)^2}{(1 + 2 \tan^2 \theta)^2}, \quad (3.9)$$

where α is an adjustable parameter (Thompson et al., 1998). For the Radarsat-1 HH-polarized SAR data, certain values which range 0.4 to 1.2 have been suggested as an optimized value (Horstmann et al., 2000; Vachon and Dobson, 2000; Monaldo et al., 2001). However, general applications of C-band HH-polarized SAR wind retrieval have set to 1, as this value shows the highest level of accuracy in most cases (Vachon and Dobson, 2000; Horstmann and Koch, 2004; Feng et al., 2004; Shen et al., 2007). In this study, we used the same value when applying PR. As a surface roughness in the region of interest assumed to be modulated by the damping effect, wind directions were obtained from ECMWF reanalysis wind datasets. In general, the wind speeds derived from HH-polarized SAR data were in good agreements with in-situ buoy measurements and scatterometer

winds by showing the accuracy of less than 2 m s^{-1} (Yang et al., 2011; Yang et al., 2011; Liu et al., 2013).

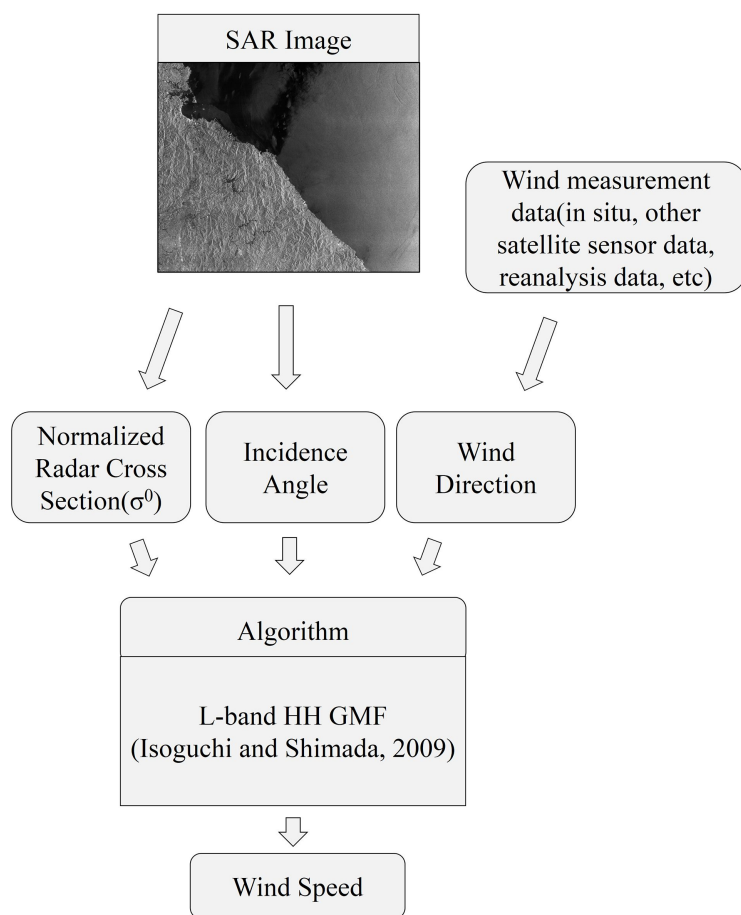


Fig. 3.1. Flow chart for sea surface wind retrieval from L-band PALSAR data.

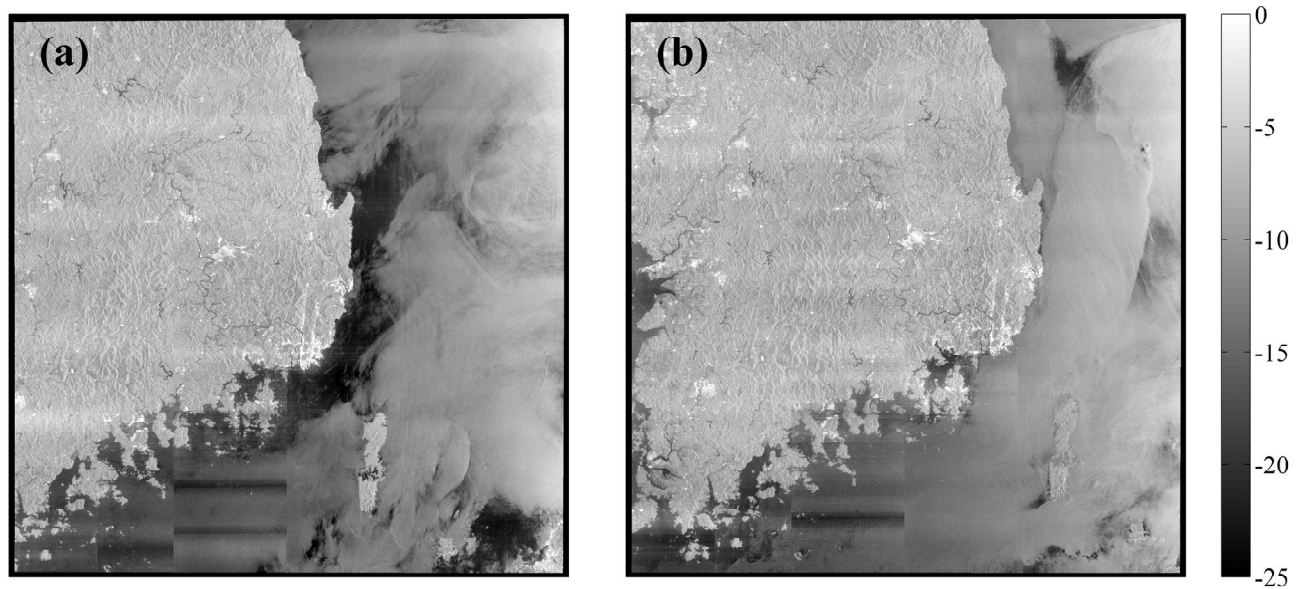


Fig. 3.2. The normalized radar cross section (dB) images of ALOS PALSAR acquired on (a) 6 August 2007 and (b) 23 August 2007.

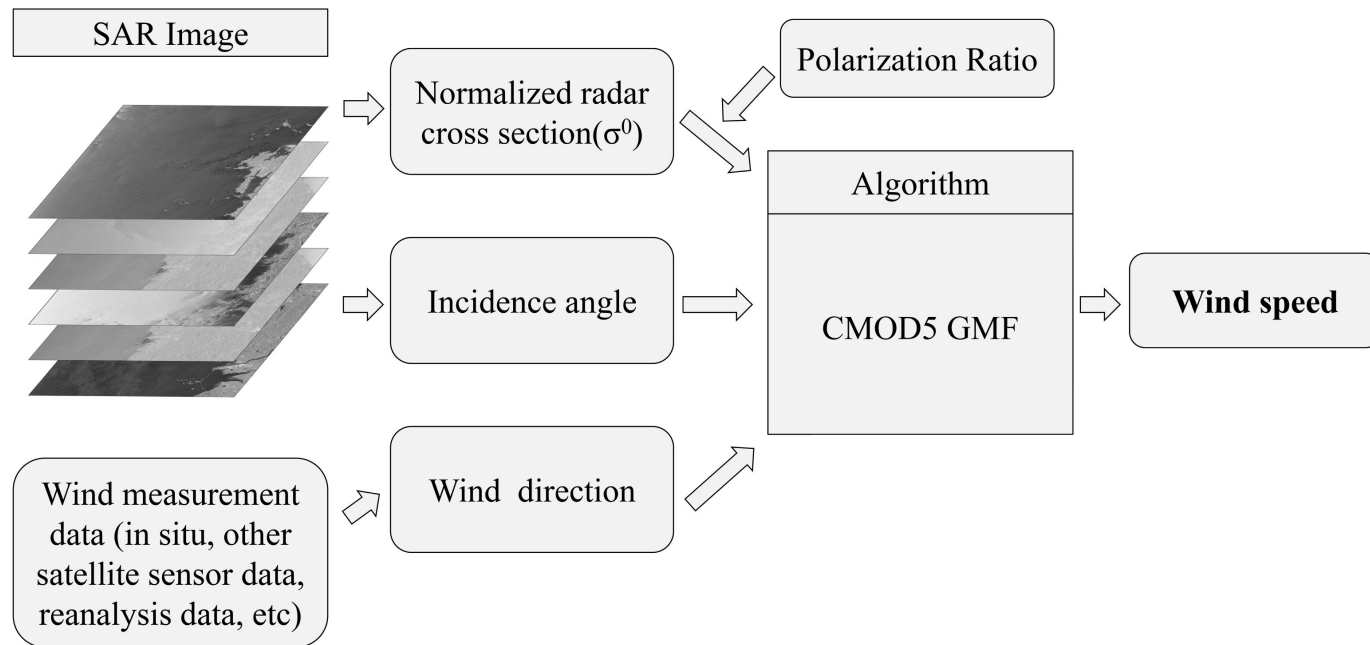


Fig. 3.3. Schematic flow chart of C-band SAR wind retrieval process.

3.2. Noise Reduction of ScanSAR Images

As shown in Fig. 3.2, the PALSAR images off the east coast of Korea include some band-like noises. These noises have been detected not only in the seas around Korea but also worldwide (Fig. 3.4). Although it has been reported that these kinds of band-like noise patterns could be originated from the interference signals of the ground radars so that the degraded components of SAR raw data might appear on the image (Shimada et al., 1999), the exact causes of the noises have yet to be clarified.

The locations of the noise patterns were distributed randomly, but it had the shape of km-scale thick band and relatively high uniformity of NRCS values along the range direction. Thus, it is assumed that NRCS values corresponding to the noise can be extracted by abrupt discontinuity in the azimuthal and range directions. Fig. 3.5a indicates an example of the subset image with band-like noise patterns. We extracted the noises from the image using spectral analysis, deriving uncorrelated signals from the neighboring signals of the range direction (Fig. 3.5b). To extract a consistent noise part from the subset, averaged Fourier transform values of each subset along the range direction were used. In turn, the subset images without noise patterns were retrieved by subtracting them from the original images. As shown in Fig. 3.5c, the magnitudes of the NRCS were decreased drastically since the noise part within the low frequency range having high energy were filtered out. For the retrieval of quantitative oceanic parameters, the reduced values were compensated by the mean value of the whole image in the range direction (Fig. 3.5d). Fig. 3.5e demonstrated the NRCS image of Fig. 3.5a

after the noise reduction procedure. As shown in Figs. 3.5e and 3.5f, there was little difference in the magnitudes of NRCS before and after the noise filtering, whose mean value was -0.14 dB. Although the staircase phenomena still appeared weakly, most of band-like noises were significantly diminished, and the genuine structure of the coastal region was preserved. The noise-reduced images were used for the calculation of SAR wind fields.

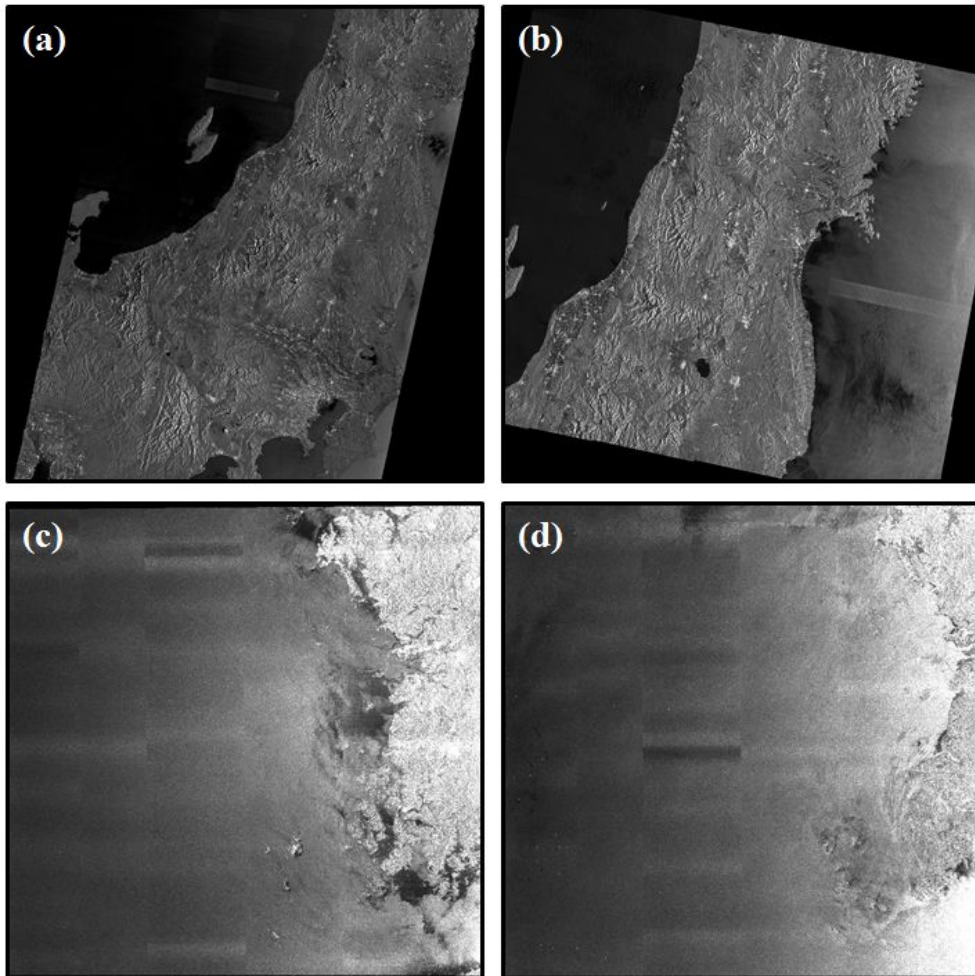


Fig. 3.4. Examples of ScanSAR mode images with band-like noises (a-b) in the seas around Japan and (c-d) in the Yellow Sea. These images were acquired on (a-b) and 17 April 2011, (c) 18 July 2007, and (d) 4 August 2007.

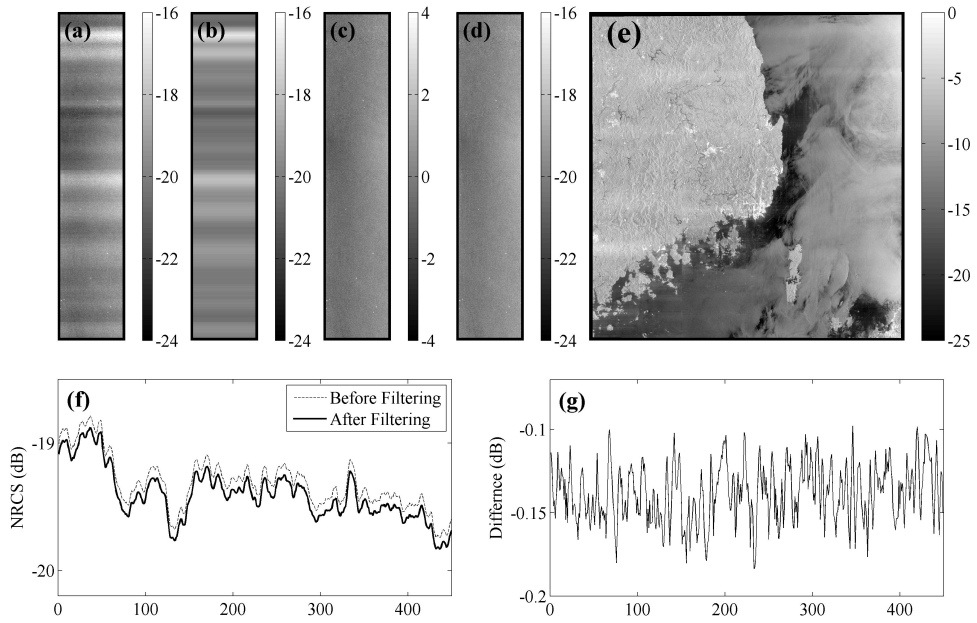


Fig. 3.5. An example of (a) band-like noises on ALOS PALSAR image, (b) extracted noises from (a) using the spectral analysis, (c) the normalized radar cross section (NRCS) without noise patterns be subtracting (b) from (a), (d) the retrieved NRCS after mean compensation, and (e) the NRCS image of Fig. 3.2a after noise reduction procedure. (f) Comparison of NRCS values (dB) before and after noise filtering and (g) its differences.

3.3. Conversion of Wind Speed to Neutral Wind

In general, the satellite-based wind measurements are derived by assuming the neutral atmospheric stratification at a height of 10 m (Geernaert and Katsaros, 1986). In-situ buoy wind data, however, were measured at around 4 m, requiring it to be converted to the equivalent wind speed at 10 m. Several algorithms for the adjustment of wind speed at an observed height to the standard height of 10 m have been developed, such as the Liu-Katsaros-Businger (LKB) model (Liu et al., 1979; Liu and Tang, 1996), the logarithmically varying profile model (Peixoto and Oort, 1992), and the Bourassa-Vincent-Wood (BVW) model (Bourassa et al., 1999). Among these algorithms, we applied the LKB model to obtain the 10-m wind speed.

The LKB model was designed to calculate the height-adjusted wind speed using an observed wind speed and ancillary parameters such as air temperature, humidity, and SST. The functional form of the LKB model is expressed as follows:

$$(U - U_s)/U^* = (\ln(z/z_o) - \psi_u)/k, \quad (3.10)$$

where U and U_s indicate the wind speed at 10 m and at the sea surface, respectively. The values of z and z_o are the referenced and observed height, respectively, and k is the von Karman constant. We used a value of 0.4 which is from Paulson (1970). The friction velocity at sea surface U^* was given by the relation between wind stress and air density. Under unstable

conditions, the Businger-Dyer model (Businger et al., 1971; Dyer, 1974) gives the following stability parameter function ψ_u as follow:

$$\psi_u = 2\ln((X+1)/2) + \ln(X^2+1)/2 - 2\tan^{-1}(X) + \pi/2, \quad (3.11)$$

where $X = (1 + a_u \xi)^{1/4}$ and $\xi = z/L$. The coefficient a_u was given a value of 10 and the Obukhov length L was derived using the potential temperature T and specific humidity Q (Liu and Tang, 1996). More details are in Liu and Tang (1996).

3.4. Estimation of Index of the Tidal Front

Due to the relatively strong tidal currents and shallow water depth in the Yellow Sea, transitions between the stratified and mixed regimes of the Yellow Sea are generally controlled by the magnitude of tidal mixing. Along the tidal front, steep gradients of the sea surface temperature and salinity have been readily found, and they invoke different types of vertical circulation mechanisms on each side (Takeoka et al., 1997). Thus, for a better understanding of the effect of vertical mixing on the evolution of oil spills, the locations of the tidal fronts and their magnitudes should be quantitatively estimated.

Simpson and Hunter (1974) demonstrated that a tidal front is formed by a change of the energy balance between the vertical mixing energy induced by tidal currents and the potential energy to maintain the mixing of the water column. This energy balance relationship can be written as

$$H/U^3 = 8c\rho k\epsilon/3\pi gQ, \quad (3.12)$$

where H is the water depth, U is the amplitude of the tidal current, c is the specific heat, ρ is the density of the water column, k is the drag coefficient, ϵ is the fraction of the kinetic energy, g is the rate of gravitational acceleration, and Q is a rate of heat input. Within the limited area of interest, parameters on the right-hand side can be regarded as having constant values. Thus, it is assumed that the formation of the tidal front is

determined by the distribution of H and U . Given that U at each spatial point varies with time depending on variations in the tidal elevation, we utilized the maximum value of U during the period, U_{\max} , to determine the tidal front from the spatial distribution of the ratio of H/U_{\max}^3 .

3.5. Estimation of Ekman Drift and Tidal Residual Current

The Ekman surface drift currents and the tidal residual currents were calculated to compare the impacts of wind and tide on the evolution of an oil spill. The residual tides were derived from a harmonic analysis of numerical model data over a time period of one month, with an interval of one hour. The analysis was conducted using the t-tide (Pawlowicz et al., 2002).

The Ekman drift current generated by wind stress was calculated from the following equation (Mao and Heron, 2008):

$$V_E = \frac{\rho_a C_D U_{10}^2}{\rho_w \sqrt{f A_z}}, \quad (3.13)$$

where ρ_a is the air density, C_D is the drag coefficient, U_{10} is the QuikSCAT wind speed at a height of 10 m, ρ_w is the sea water density, and f is the Coriolis parameter. The vertical eddy viscosity A_z is given by $0.005 \text{ m}^2 \text{ s}^{-1}$, as in Guo and Yanagi (1998). The drag coefficient, C_D , increases with the wind speed, and it was determined by Anderson (1993) for a more accurate calculation (Park et al., 2006).

3.6. Feature Detection Methods

Much research has been performed to develop a methodology for feature detection using spaceborne SAR imagery which is mainly focused on detection for oil spills due to its exceedingly high spatial resolution under all-weather conditions (Espedal and Wahl, 1999; Gade and Alpers, 1999; Fiscella et al., 2000; Jones, 2001; Brekke and Solberg, 2005; Nirchio et al., 2005; Shi et al., 2008; Topouzelis, 2008; Hu et al., 2009; Klemas, 2010; Liu et al., 2010; Cheng et al., 2011; Li et al., 2012; Mera et al., 2012; Minchew, 2012; Xu et al., 2013; Cheng et al., 2014; Nunziata et al., 2014). For single-polarized SAR images, three types of methods have been widely utilized for detection: an adaptive threshold method (Vachon et al., 1998; Solberg et al., 1999); a bimodal histogram method (Skøelv and Wahl, 1993; Kim et al., 2013); and a neural network method (Del Frate et al., 2000; Garcia-Pineda et al., 2009; Garcia-Pineda et al., 2013). SAR systems have improved in their ability to increasingly observe the oceanic surface at a full-polarized state (HH/HV/VH/VV), and new techniques for processing the full-polarized data have also developed rapidly. Representative methods for the multi-polarized SAR data, such as a decomposition analysis (Migliaccio et al., 2007; Liu et al., 2011; Li et al., 2014) and a conformity coefficient method (Zhang et al., 2011), have been attempted for monitoring oil spills.

Although the polarimetric approach was determined to be more accurate and more applicable to oil detection, particularly in the discrimination of oil slicks from look-alikes, such as low wind regions, rain cells, and shear zones (Velotto et al., 2011; Migliaccio et al., 2011; Li et al., 2014), a

limited number of multi-polarized SAR data were unable to be used extensively for operational monitoring and for diverse purposes of scientific understanding on the spatial distribution and temporal evolution of oil patches. Such infrequent measurements allowed us more opportunity to use the single-polarized SAR data. In light of this, we used a thresholding method and the neural network method for single-polarized SAR images in this study.

The adaptive threshold method, which is the most widely used methods among the thresholding methods, has the advantage of being able to reduce computation time, but it also has a disadvantage in terms of the difficulty of setting the threshold objectively. Thus, a more robust method that is capable of determining the threshold objectively and automatically for operational purposes is necessary. Therefore, in this study, we introduced the bimodal histogram method for oil spill detection from SAR images with a single polarization, and then compared this method with the adaptive threshold method.

3.6.1. Adaptive Threshold Method

The adaptive threshold method determines a threshold within each window with its statistical values (Vachon et al., 1998; Solberg et al., 1999). This is one of the most widely used methods for oil spill detection from SAR images because it does not require a high computation efficiency or prior environmental knowledge.

Fig. 3.6 shows a flow chart of the oil spill detection procedure with SAR data using the adaptive threshold method. Pixels in the land areas

were masked using DEM data, and then, the remains were averaged in a 5×5 window to reduce speckle noise. The adaptive threshold in a moving window was determined based on the mean and standard deviation of NRCS values. Each window shifted to the next one overlapping by 1/8 of window size to avoid the omission. The low NRCS pixels were denoted with dark spots according to the threshold. For better separation of the spill from its surroundings, the detected dark spots were clustered with connectivity in eight neighborhood directions. Among the clusters, dark spots that were smaller than the minimum cluster size were assumed to be look-alikes induced by noise and thus discriminated (Kim et al., 2013).

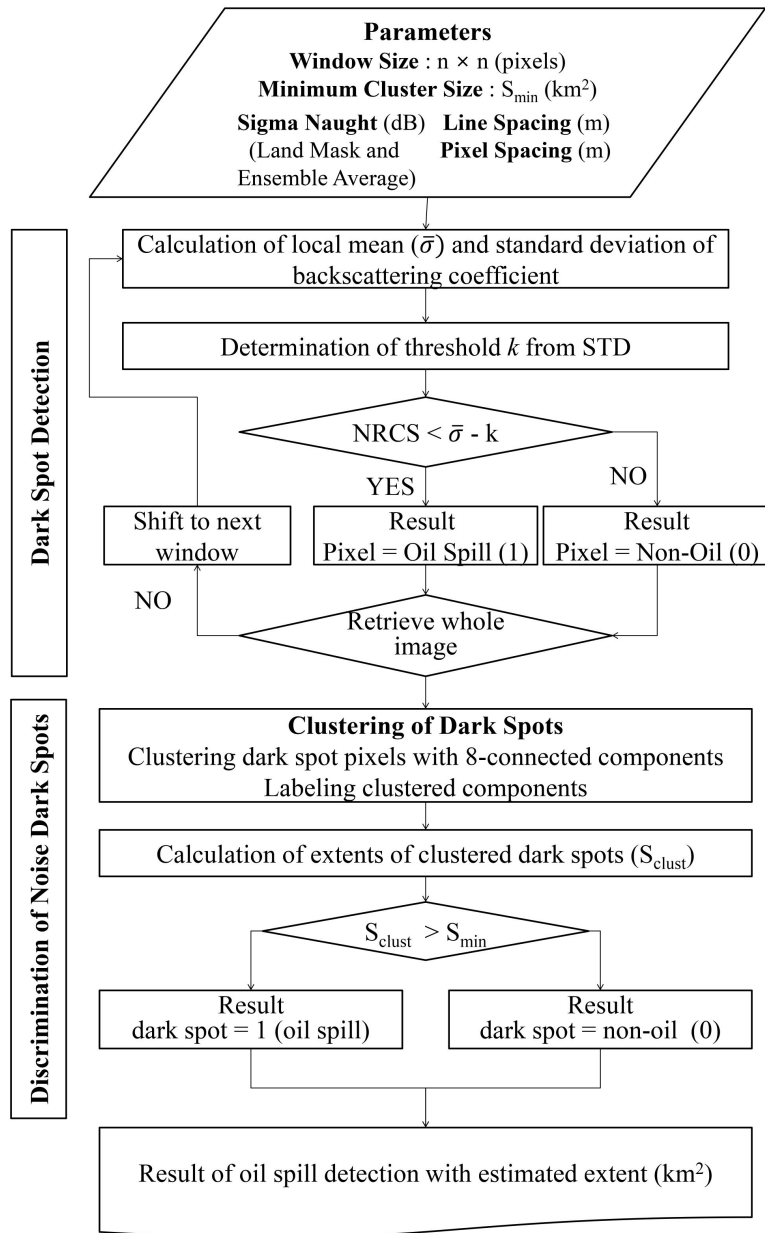


Fig. 3.6. Flow chart of the oil spill detection process using the adaptive threshold method.

3.6.2. Bimodal Histogram Method

The bimodal histogram method separates oil spills from the sea surface based on the distribution of NRCS in a window (Skøelv and Wahl, 1993). As shown in Figs. 3.7a and 3.7b, generally a sea surface without oil has a form of histogram with unimodal distribution. On the contrary, a sea surface with oil slicks shows a bimodal distribution which has two distinct peaks, since oil slicks typically have much lower NRCS values than the surrounding background (Figs. 3.7c and 3.7d). Thus, oil spills in SAR images can be identified by analyzing the form of histogram produced.

Fig. 3.8 shows the schematic flow chart of oil spill detection for SAR data using the bimodal histogram method. In general much of the procedure is similar to that of the adaptive threshold method, with the exception of histogram analysis and threshold determination. While the threshold of the former method was simply given based on the mean and standard deviation, that of the latter method was deduced from the characteristics of statistical distribution.

Before analyzing a form of distribution and calculating a threshold, a histogram in a moving window is fitted to multimodal Gaussian distribution functions as follows;

$$f_N(x) = \sum_{n=1}^N a_n e^{-\frac{(x-b_n)^2}{c_n^2}}, \quad (3.14)$$

where N is the total number of modes, which indicates unimodal (1-peak) and bimodal (2-peak) Gaussian distributions when $N=1$ and $N=2$,

respectively, and a_n , b_n , and c_n are coefficients for n th mode Gaussian fitted functions. By comparing calculated f_{1-3} and its coefficient of determination R^2 , it was determined which mode is the best fit to a form of histogram in a moving window.

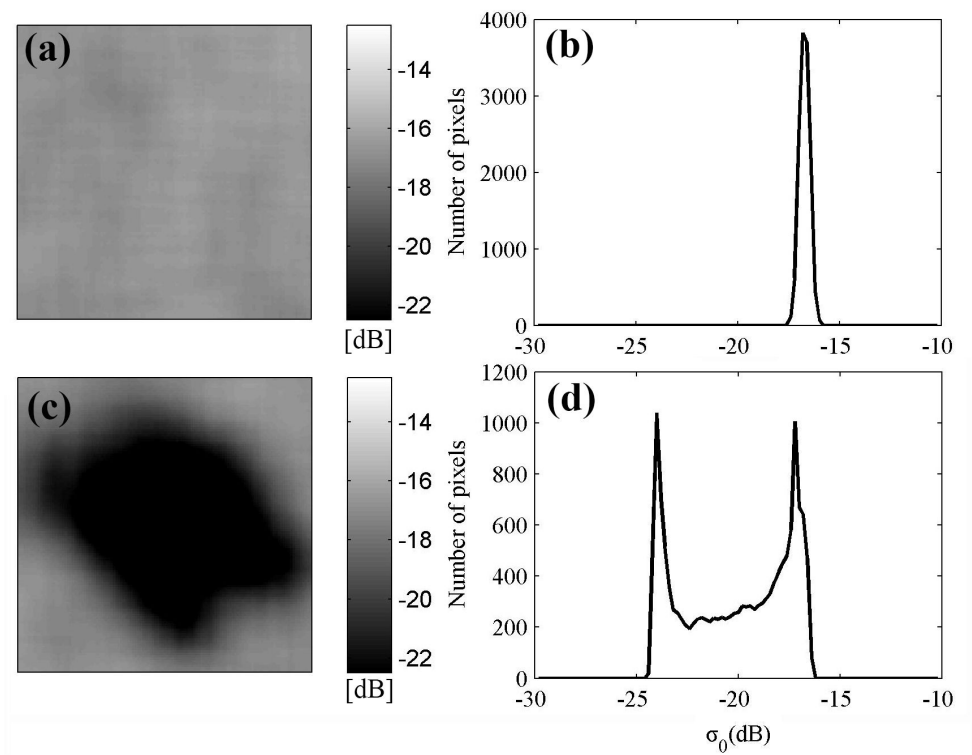


Fig. 3.7. (a) Spatial distribution of NRCS at a clean sea area without any oil spill and (b) its histogram, (c) NRCS at an area with oil slick and (d) its histogram.

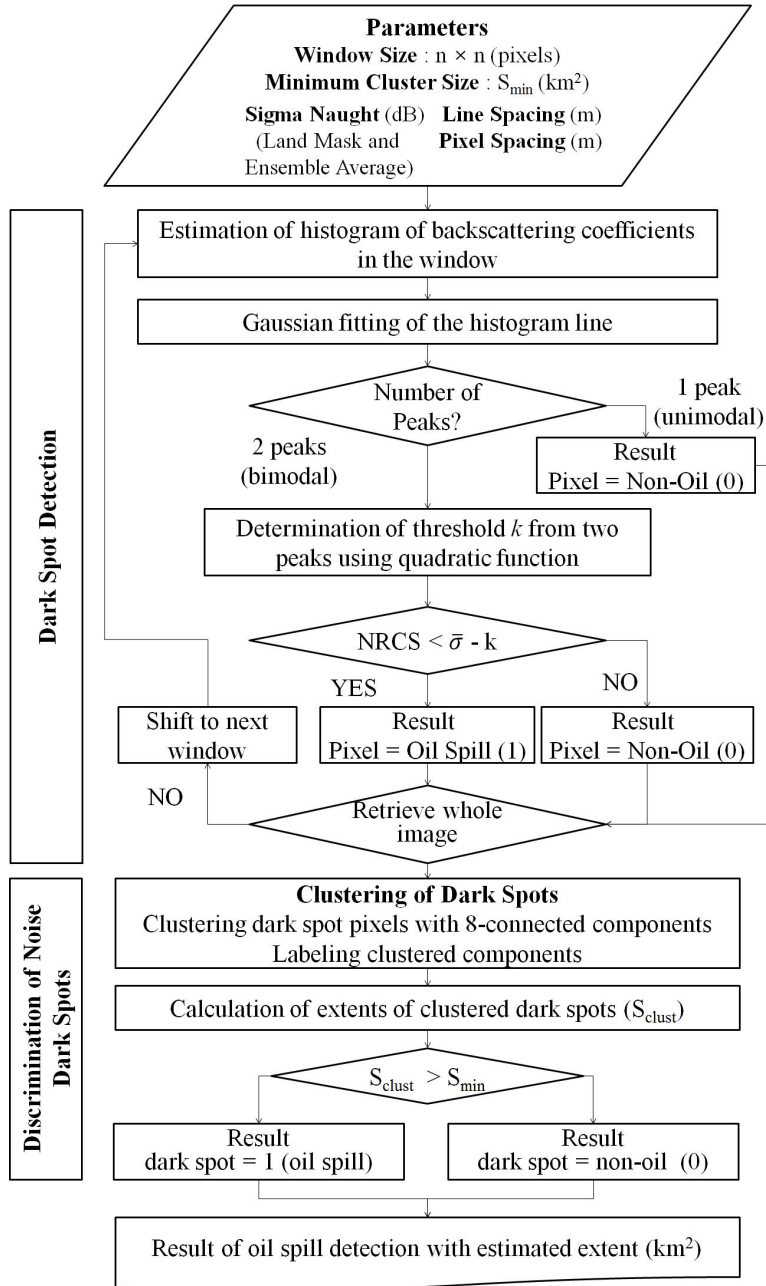


Fig. 3.8. Flow chart of the oil spill detection process using the bimodal histogram method.

3.6.3. Neural Network Method

Another approach for oil spill detection is based on neural network. It has been found that the application of neural networks in remote sensing offers effective pattern recognition, identification, and classification results, as neural networks can approximate the non-linear functions of their inputs (Yeom et al., 2008; Garcia-Pineda et al., 2009; Singha et al., 2013; Taravat et al., 2014). With the nonlinear mapping of a multidimensional input onto the output space, statistical complexities can be overcome (Del Frate et al., 2000).

In this study, we utilize a two-layer feed-forward back propagation neural network for pixel-by-pixel oil spill detection (Svozil et al., 1997; Haykin, 1999). Fig. 3.9 illustrates the architecture of the neural network method used in this study. The input layer consists of 14 neurons in three main parts, corresponding to the two values of the NRCS and the wind speed as estimated from the CMOD5 algorithm at a given SAR image pixel, and two sets of six textural values, i.e., the average intensity (m), average contrast (σ), smoothness (R), third moment (μ), uniformity (U), and entropy (e) at a centered pixel at two different window sizes of $N_1 \times N_1$, and $N_2 \times N_2$ for a textural classification. Each textural parameter is determined as follows:

$$m = \sum_{i=0}^{L-1} z_i p(z_i), \quad (3.15)$$

$$\sigma = \sqrt{\sum_{i=0}^{L-1} (z_i - m)^2 p(z_i)}, \quad (3.16)$$

$$R = 1 - 1/(1 + \sigma^2), \quad (3.17)$$

$$\mu = \sum_{i=0}^{L-1} (z_i - m)^3 p(z_i), \quad (3.18)$$

$$U = \sum_{i=0}^{L-1} p^2(z_i), \quad (3.19)$$

$$e = \sum_{i=0}^{L-1} p(z_i) \log_2 p(z_i), \quad (3.20)$$

where z_i is the pixel value, $p(z_i)$ is a histogram of the NRCS in the window, and L is the number of NRCS levels (Gonzalez et al., 2004). The bounding window sizes were determined to be 21×21 and 51×51 based on those in Garcia-Pineda et al. (2013).

Network optimization was performed using the Levenberg-Marquardt method (Hagan and Menhaj, 1994). For each training procedure, the weights and biases were updated and minimized using the mean square errors (Hagan et al., 1996). A number of neurons in the each layer can be determined by trial and error and based on computation efficiency (Atkinson and Tatnall, 1997; Garcia-Pineda et al., 2009; Singha et al., 2013). Based on the trial results, the numbers of neurons in the hidden layer and output

layer were set to 5 and 1, respectively.

To build a training function, four SAR images (as shown in Figs. 2.2b, 2.2d, 2.2e, and 2.2f) which contain clear dark spots and backgrounds were selected and databased into the training set. Using the training data, a learning process was undertaken to update the weights and biases of the training function until the mean square error reached 0.1 as a performance goal.

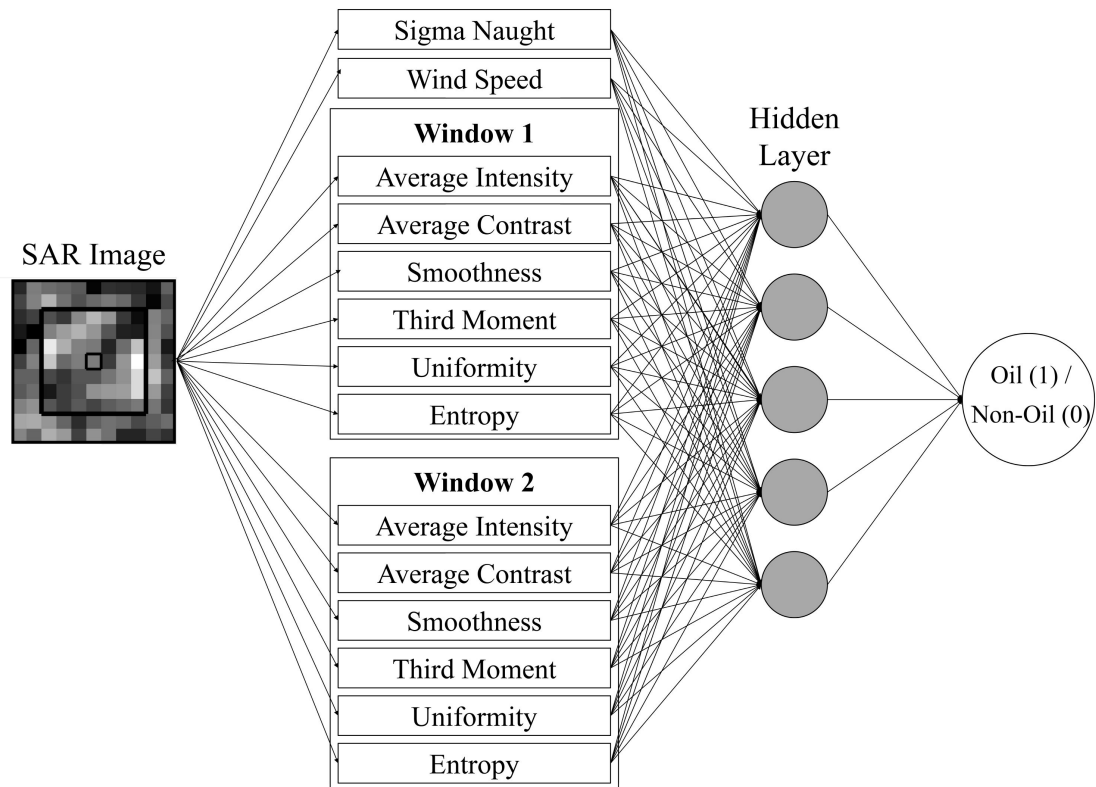


Fig. 3.9. Schematic diagram of the oil spill detection process based on a neural network.

Chapter 4. Coastal Wind Fields and Upwelling Response

4.1. Variations of Wind Fields during Coastal Upwelling

Fig. 4.1 shows the distributions of the NRCS from the PALSAR images during the coastal upwelling in 2007 after the noise reduction procedure. On 6 August 2007, the value of NRCS in the ocean ranged from -25 dB to -3 dB and the mean of the values for the entire dataset amounted to -12.9 dB. The right part of the image which was apart from the coast showed higher values of about -7 dB while the middle parts of the image along the coastline showed a significantly lower value of about -19 dB. These low NRCS features were associated with the coastal region where the upwelling events frequently appear.

Figs. 4.2a and 4.2b show the distribution of wind speeds retrieved from PALSAR data using the L-band HH GMF algorithm along the east coast of Korea on 6 and 23 August 2007, respectively. On 6 August 2007, the mean wind speed in the study area was 4.5 m s^{-1} . Moderate southerly winds of around 5 m s^{-1} were apparent off the east coast of Korea and relatively strong southeasterly winds ranging from 6 to 10 m s^{-1} appeared off the southern coast. By contrast, low winds of less than 3 m s^{-1} were dominantly distributed along the east coast. On the other hand, the spatial distribution of SAR wind field on 23 August 2007 showed a relatively uniform pattern overall with a prevailing strong southwesterly wind, except for in the upper right part of the image where a significant low wind patch

appeared, which stretched from the coast of cape Homi (red dot on Fig. 4.2) at 36°N to northeastward corresponding to the wind direction. The mean of wind speeds in Fig. 4.1b indicated a value of 6.3 m s⁻¹ whereas the wind speeds of the patch were less than 2.5 m s⁻¹. The retrieved SAR wind speed coincided well with buoy measurements (128.90°E, 34.76°N) by a difference of 0.7 m s⁻¹, which were 3.0 m s⁻¹ for the SAR wind and 2.3 m s⁻¹ for the buoy wind, respectively.

In order to investigate the causes of spatial distinction of SAR wind fields at the coastal regions, we analyzed the distributions of SST and wind conditions during upwelling events. Figs. 4.3a and 4.3b presented the spatial distribution of SST from NOAA AVHRR on 4 August 2007 and 23 August 2007, respectively. On 4 August 2007, low SSTs which were 5°C cooler than those off the coast appeared along the coast from 35°N to 36°N and spread out across the region beyond 36°N (Fig. 4.3a). In late August, SSTs seemed to have been advected to the northeast (Fig. 4.3b). The SST image was partly obscured by clouds, but those along-coast low SSTs were comparatively matched with the region where low magnitude of SAR-derived wind speeds were apparent. This implied that the spatial distinction of coastal winds was mostly related to variations in SST at the coastal area.

Moreover, it is known that the southeasterly wind blows predominantly from July to August along the east coast of Korea (Lee, 1983; Lee and Na, 1985). This year, stronger southerly winds blew longer than previous years (Park and Kim, 2010). As shown in Fig. 4.4, the time series of in-situ wind measurements from KMA AWS indicates that southerly wind, which tends to induce coastal upwelling in the Northern Hemisphere, was dominant

throughout August 2007. Significant southerly winds greater than 6 m s^{-1} blew over two periods from August 1st to 17th and partly from 20th to 26th, with cold water masses appearing after a time lag of approximately 1-3 days. It seems to be typical of the pattern of wind-induced upwelling events prevalent in the region (Lee and Na, 1985; Suh et al., 2001; Lee et al., 2003; Kim and Kim, 2008), though this particular duration was longer than the average year. In-situ SST measurements from the NFRDI coastal station demonstrated that SSTs along the coast started to decrease drastically from early August and lasted to nearly the end of the month, until the magnitude of southerly winds began to decrease to less than 2 m s^{-1} . Thus, the spatial distinctions of wind speeds associated with coastal upwelling were apparent on SAR-derived wind fields.

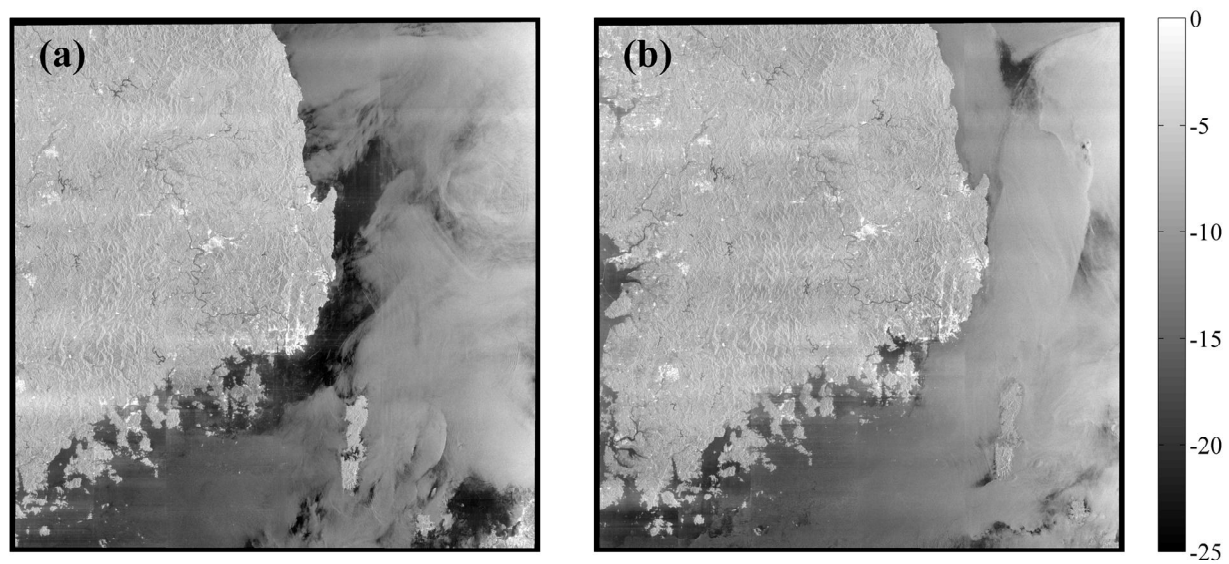


Fig. 4.1. The normalized radar cross section (dB) images of ALOS PALSAR acquired on (a) 6 August 2007 and (b) 23 August 2007 after the noise reduction procedure.

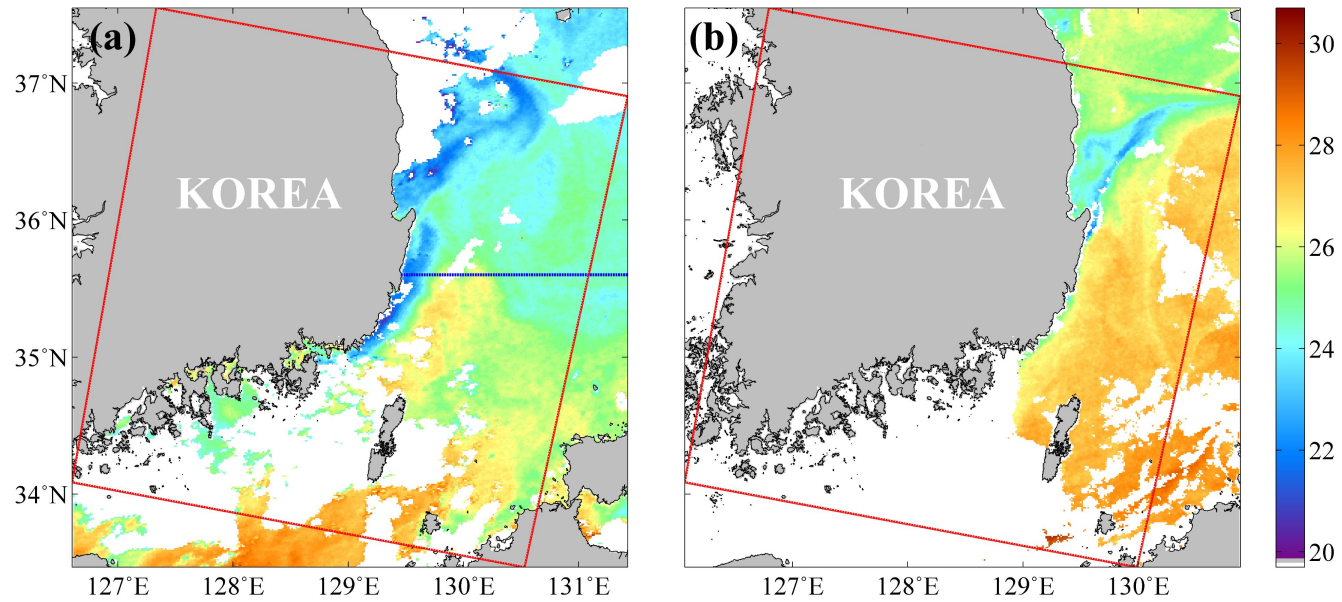


Fig. 4.3. Distributions of sea surface temperature ($^{\circ}\text{C}$) from NOAA AVHRR at (a) 12h 22m (UTC) on 4 August 2007 and (b) 06h 38m on 23 August 2007, where red box indicates the boundary of ALOS PALSAR images and the blue line represents the section for the comparison with sea surface temperature.

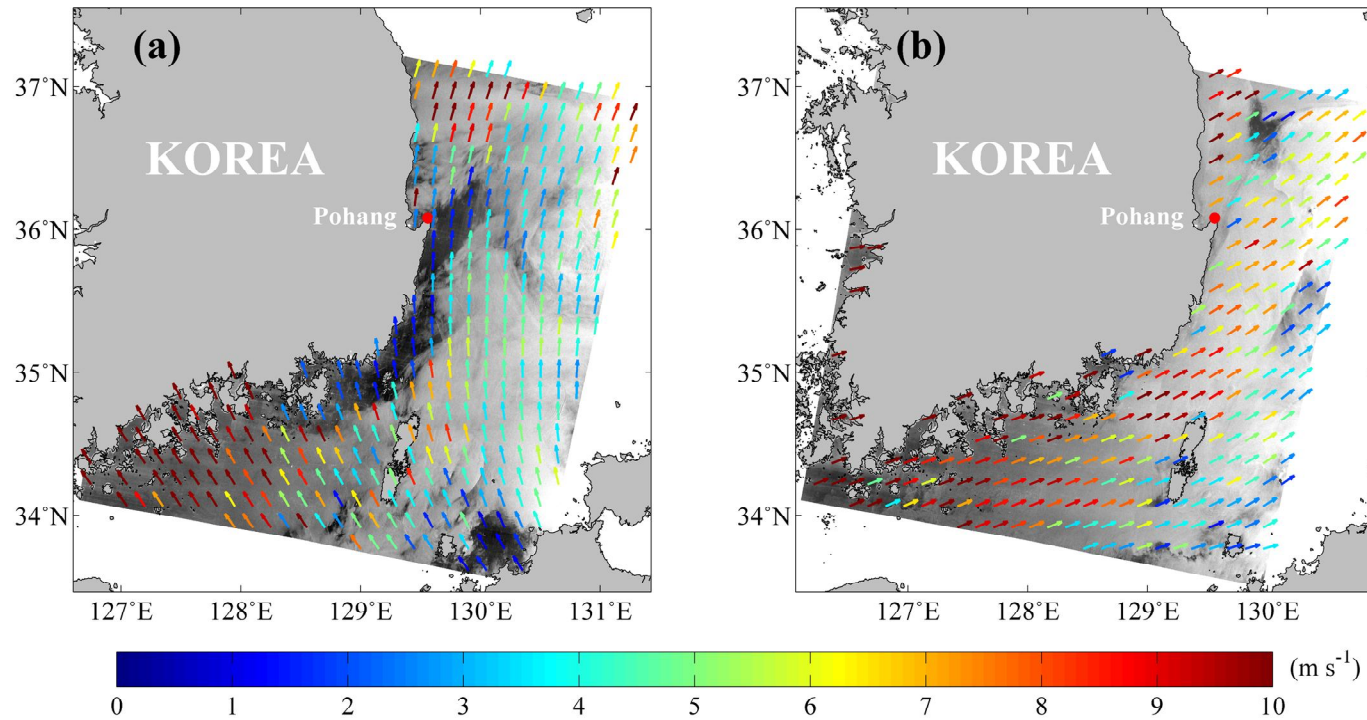


Fig. 4.2. Distributions of wind vectors retrieved from the PALSAR imagery at (a) 02h 00m (UTC) on 6 August 2007 and (b) 02h 02m on 23 August 2007, where the red dot indicate the location of Cape Homi.

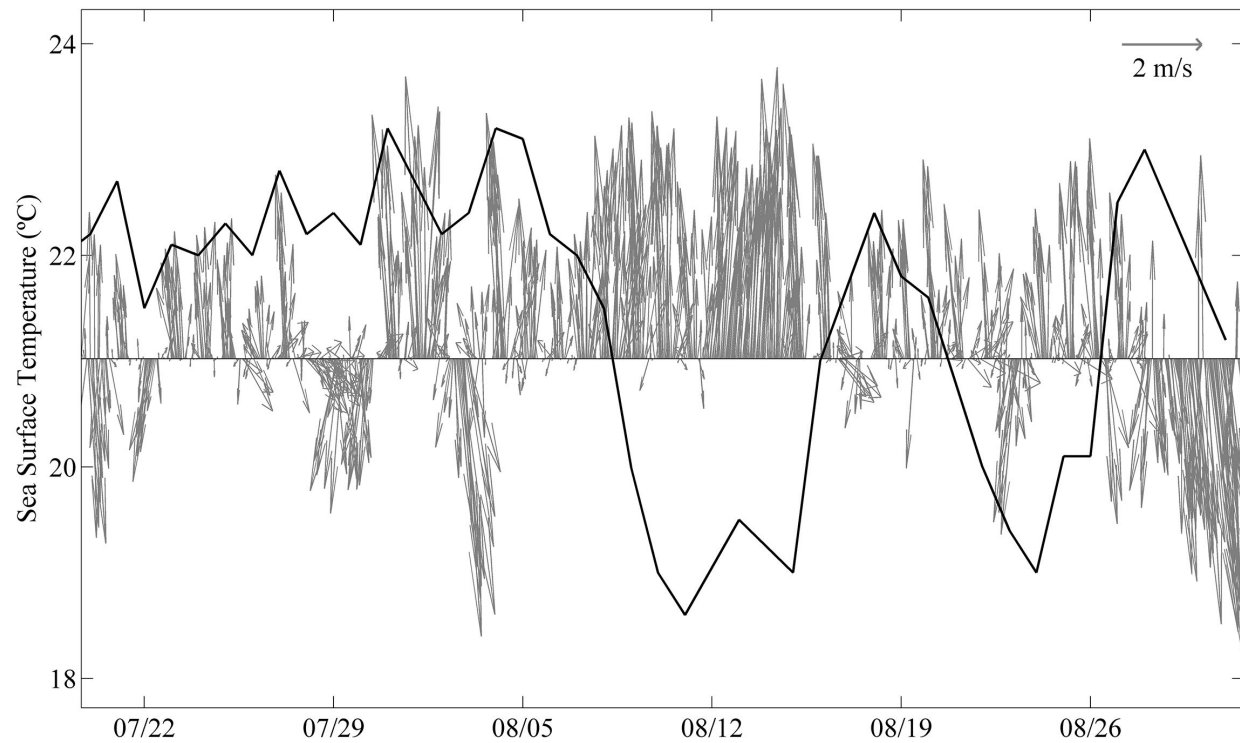


Fig. 4.4. Time series of wind vector (gray arrow, m s^{-1}) from AWS measurement of KMA and sea surface temperature (black solid, $^{\circ}\text{C}$) from NFRDI coastal station measurements.

4.2. Stability Effect on Wind Speed

Figs. 4.1a and 4.1b clearly showed small NRCS values in the upwelling zones off the coast, which were contrasted by high NRCS offshore regions. There have been many arguments as to whether the low wind speeds corresponding to small NRCSs were induced by low temperatures due to upwelled cold water or atmospheric stability within the marine atmospheric boundary layer (MABL). Clemente-Colón and Yan (1999) addressed the effect of changes in MABL stability and viscous properties of the sea surface on the variation of NRCS. Other researches have pointed out that the upwelled cold water has an effect on the initiation and dissipation of short gravity waves, which in turn leads to a decrease in radar backscattering and hence the magnitude of wind speeds (Weissman, 1990; Zheng et al., 1995).

A kind of the tendency like as the latter is also found in the study area. Fig. 4.5 presents a comparison of sea surface temperature (T_s , °C) and retrieved wind speed from the ALOS PALSAR image along the section in Fig. 4.3a. The wind speed magnitude showed a somewhat positive correlation with the SST ($R^2 = 0.59$). But more importantly, it is notable that large air-sea temperature differences induced by the strong coastal upwelling prevailed during the period.

In order to distinguish between the different effects on satellite measurements, we estimated changes in NRCS values and compared them with the dependence of radar backscattering on water viscosity based upon

the method of Zheng et al. (1995). The backscattering attenuation gradient of the section in Fig. 4.3a has a much larger gradient of about $1.2 \text{ dB } ^\circ\text{C}^{-1}$ than the threshold of $0.2 \text{ dB } ^\circ\text{C}^{-1}$ set by Zheng et al. (1995). Such a large difference implies that the attenuation gradient of NRCS was mainly induced by other additional factors. It has been reported that the sensitivity of the NRCS to SST, which is related to changes in the marine boundary layer stability, is estimated to be up to $1\text{-}2 \text{ dB } ^\circ\text{C}^{-1}$ based on analysis of the U.S. east coast upwelling feature (Clemente-Colón, 2001; Donato and Marmorino, 2002). Thus, it is inferred that the low wind speeds at the present upwelling region were caused by the modification of wind fields due to changes in MABL stability.

The stability of MABL can be indirectly estimated by the air-sea temperature difference. Fig. 4.6a presents a comparison of temperature difference ($^\circ\text{C}$) between sea surface temperature and air temperature, $T_s - T_a$, and SAR-derived wind speed along the section in Fig. 4.3a. For the analysis of wide coverage, air temperature data from the ECMWF reanalysis data was used. A mean value of T_a along the section indicated 25.1°C which was similar to the ten-year average (24.5°C) of in-situ measurements observed from 2001 to 2010 at the NFRDI coastal station (35.49°N , 129.44°E).

As shown in Fig. 4.6a, wind speed ranged from 1.5 m s^{-1} to 6.3 m s^{-1} and the SST-air temperature difference ranged from -1.7°C to 2.1°C . It is indeed, however, assumed that actual sea surface temperature at the upwelling event was much lower than those from the satellite observation. When strong upwelling occurs, coastal region is frequently covered with

clouds and fogs overall so that it is hard to observe low temperature at the time from satellite SST images (Clemente-Colón and Yan, 1999; Uiboupin and Laanemets, 2009). According to previous researches, when the cold water mass induced by coastal upwelling appeared, sea surface temperature at this region dropped to 11-16 °C (Lee and Na, 1985; Suh et al., 2001; Lee et al., 2003; Kim et al., 2010; Park and Kim, 2010). In spite of that, when compared to those at non-upwelling region in an unstable condition, the surface layer at the coastal region can be regarded as relatively stable state. This implies that the effect of MABL stability induced the modification of the derived wind field in this region. Johannessen et al. (1996) demonstrated that the variation of the radar backscattering near coastal fronts is attributed to the change in MABL stability under large air-sea temperature differences analogous to those of the study area.

Fig. 4.6b illustrates that wind speed magnitude has an obvious positive correlation with the difference between SST and air temperature ($R^2 = 0.63$). The wind speed tends to increase at a rate of as $0.73 \text{ m s}^{-1} \text{ }^{\circ}\text{C}^{-1}$ the temperature difference increases. As the difference between SST and surface air temperature increases, the instability of MABL increases. As MABL becomes more destabilized, higher momentum can be transferred, i.e., increasing wind stress, and thus amplifying the magnitude of surface winds (Park et al., 2006). Thus, the low wind speed of the upwelling zone is believed to have been induced by air-sea temperature differences and a change in MABL stability.

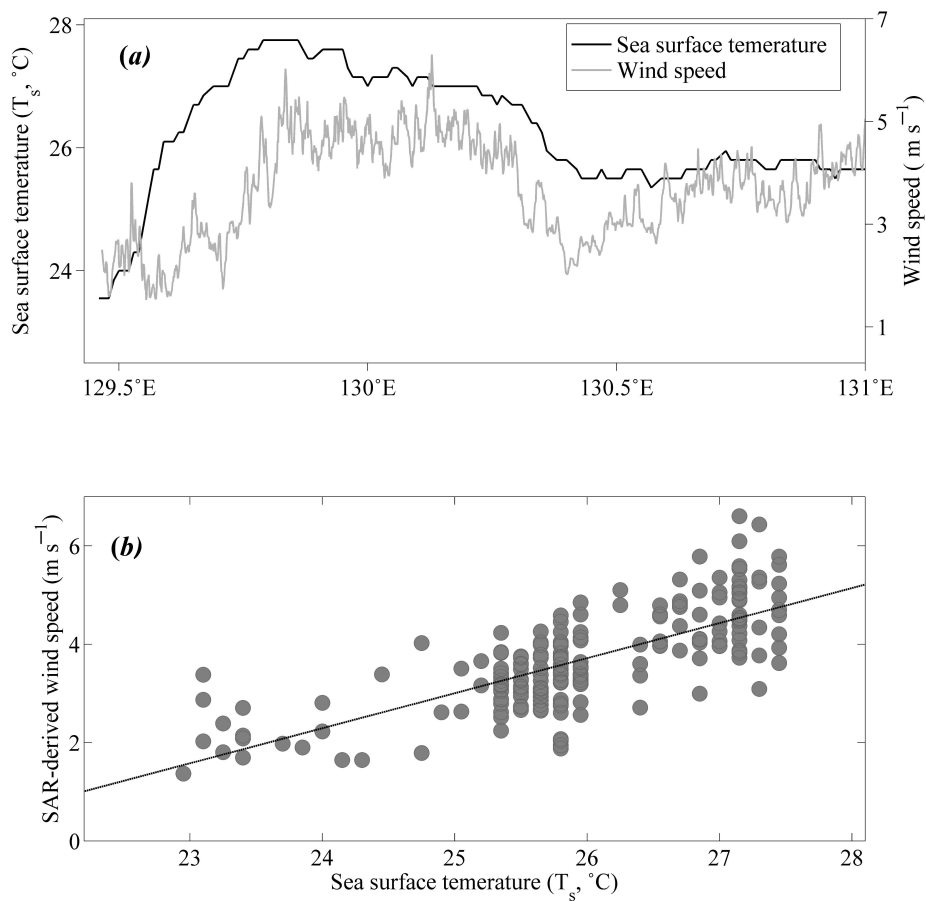


Fig. 4.5. (a) Comparison of sea surface temperature (°C) and SAR-derived wind speed (m s^{-1}) along 35.6°N ($<131^\circ\text{E}$) as shown in the blue line of Fig. 4.3 and (b) SAR-derived wind speeds as a function of sea surface temperature (T_s).

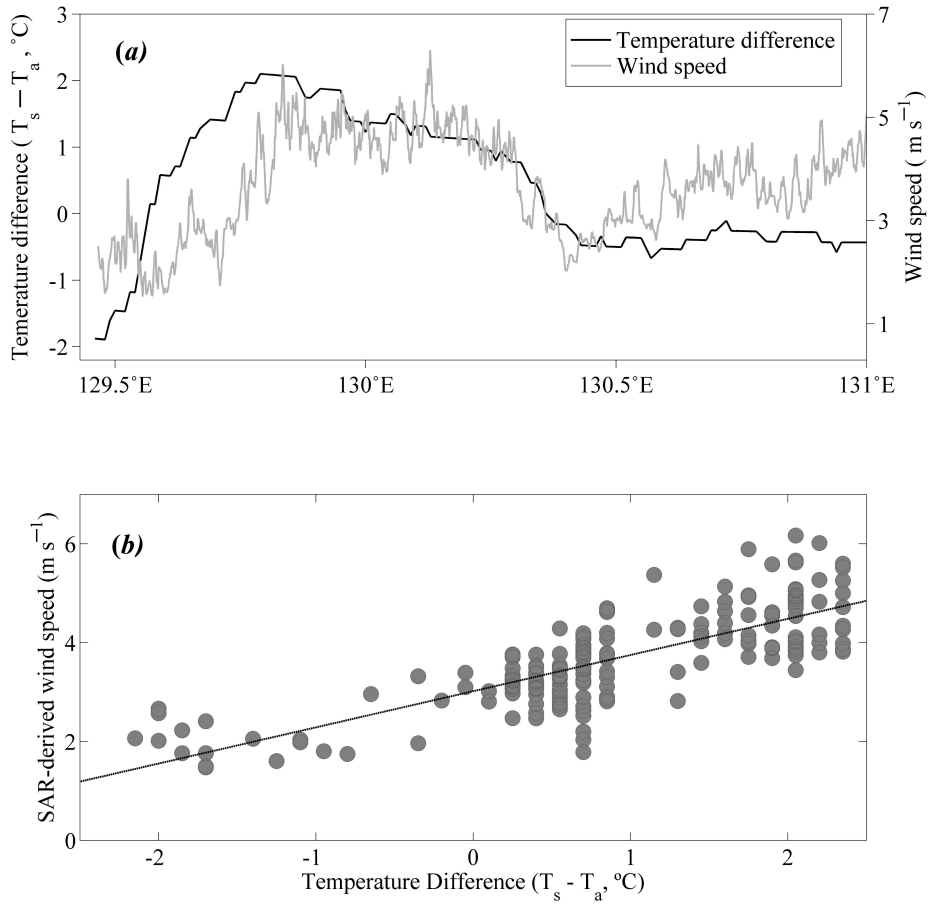


Fig. 4.6. (a) Comparison of sea surface and air temperature difference ($T_s - T_a$, °C) and SAR-derived wind speed (m s^{-1}) along 35.6°N ($< 131^\circ\text{E}$) as shown in the blue line of Fig. 4.3 and (b) SAR-derived wind speeds as a function of temperature difference (°C).

4.3. Biological Impact of Upwelling

The upwelling event along the east coast of Korea in the summer of 2007 was the strongest recorded in decades (Park and Kim, 2010). It appeared from southern part to northern part over 37°N , which was much farther north than the usual upwelling sites. While a cold water mass induced by upwelling was dominantly present at the southern part only in normal upwelling period, the strong upwelling events in the summer of 2007 were present both the southern and northern coast of Korea. Figs. 4.7a and 4.7c present the distributions of sea surface temperature which indicate one of the typical upwelling patterns off the east coast of Korea (Fig. 4.7a) and the distinct feature of upwelling after its predominant period from late July to early August 2007 (Fig. 4.7c), respectively. In the case of the normal upwelling in 2006, a cold water mass induced by upwelling was dominantly present from $35.5\text{--}36.5^{\circ}\text{N}$, and advected north-eastward within tens of km from the coast. On the contrary, the characteristic strong southerly winds were dominant in the summer of 2007, so that favorable conditions for upwelling maintained longer in this region. As a result, a cold band of water appeared along the coast from 36°N to 37.5°N , over 100 km north from the common upwelling site, and advected eastward much farther from the coast. The flow of advected cold water induced by upwelling formed significantly strong fronts corresponding to the flow of the second branch of the Tsushima Warm Current (Fig. 4.7c). The spatial distribution of SST gradients also revealed the eastward advection of low cold waters with a large spatial gradient greater than $0.5^{\circ}\text{C km}^{-1}$ in Figs. 4.7b and 4.7c.

Moreover, phytoplankton blooms on the coastal ocean surface were invoked by upwelling. The blooms of phytoplankton are highly dependent on surrounding environmental conditions. The upwelling brings nutrient-rich water with low temperature from the deep ocean. Since the light conditions for photosynthesis are normally favorable in the summer, the supply of nutrients by upwelling may be one of the most important factors in controlling the phytoplankton blooms. Fig. 4.8 shows the distribution of chlorophyll-a concentration from SeaWiFS data in the EJS during August 2007. The feature of the bloom extended to the northeast and then to the east, which was quite similar to the SST patterns in Fig. 4.7c. This supports our hypothesis on the bloom related to upwelling, cold water, and nutrients. As the upwelling activities become increasingly sustained, so too will the blooms be enhanced and subsequently advected offshore.

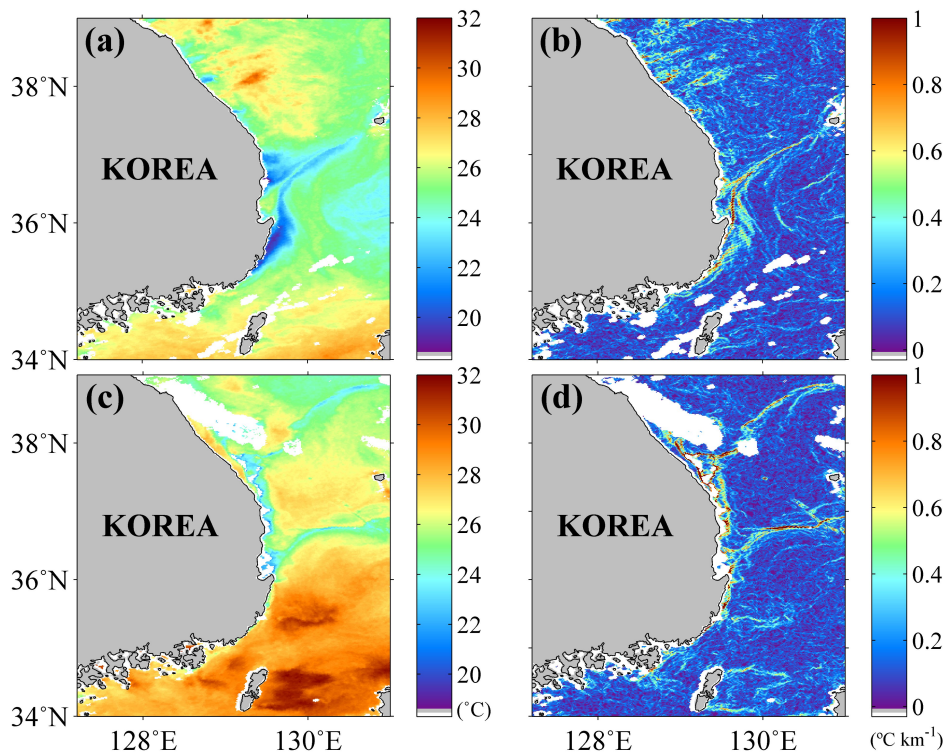


Fig. 4.7. Distributions of sea surface temperature ($^{\circ}\text{C}$) and its gradient ($^{\circ}\text{C km}^{-1}$) on 1 August 2006 ((a) and (c)) and 17 August 2007 ((b) and (d)), respectively.

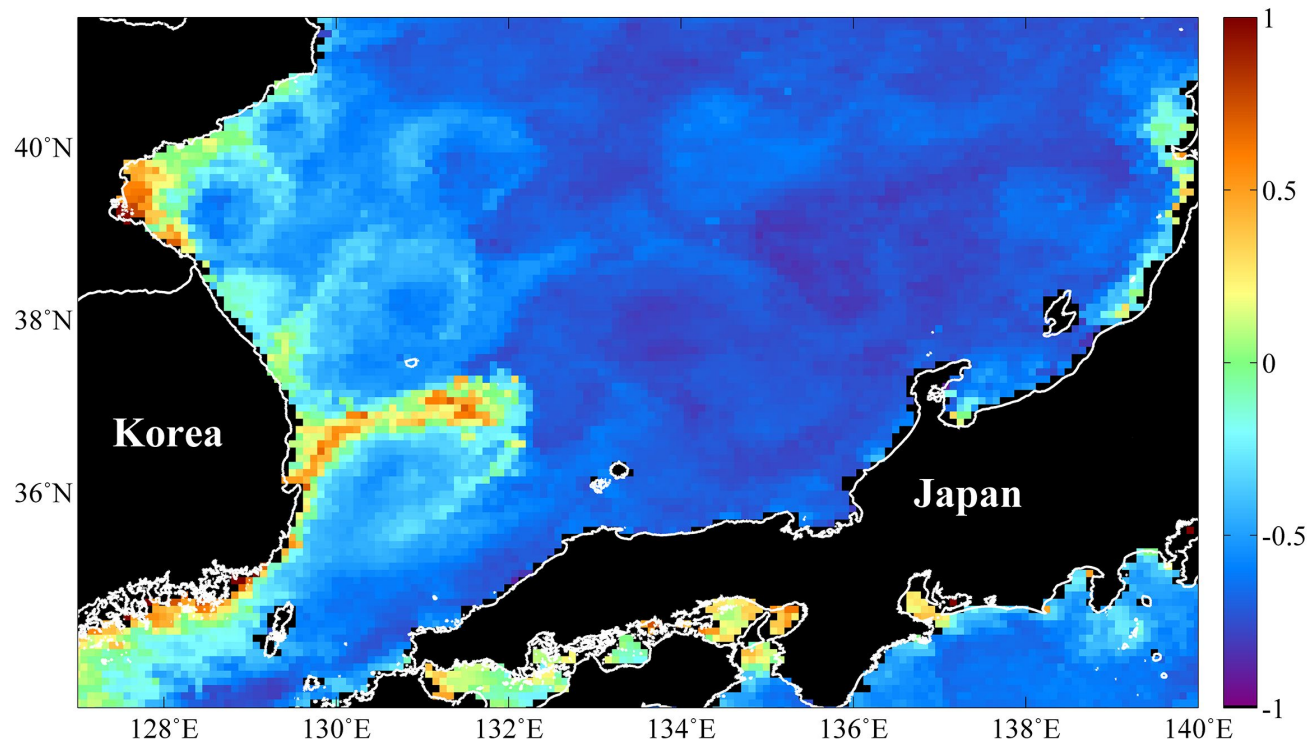


Fig. 4.8. Distribution of monthly-averaged chlorophyll-a concentration ($\log_{10} \text{ mg m}^{-3}$) from SeaWiFS in the East/Japan Sea in August 2007.

Chapter 5. Characteristics of Objective Feature Detection

5.1. Comparison of Thresholding Methods

Prior to the quantitative analysis of the oil spill detection results, we applied two thresholding methods on a SAR image with oil spills, and then compared the results from those methods with each other in order to verify the objective thresholding methods. For the test, a SAR image from ENVISAT ASAR off the coast of Libya in the Mediterranean Sea which showed obvious dark patches originated from natural oil seeps was utilized. Details of the ENVISAT ASAR image used in this study were summarized in Table 5.1. The ENVISAT ASAR image was taken at 9h 7m (UTC) on 17 September, 2006. The center of the study area is located at 14.66°E, 32.82°N.

Fig. 5.1 presented the distribution of NRCS at the study area and the derived results of oil spill detection based on the adaptive threshold method. Oil slicks with rounded shapes appeared around the upper middle part of the image. In addition, linear or dotted dark spots assumed to be artificial structures or noises (look-alikes) were also detected to some extent. These small dark spots can be discriminated by setting minimum cluster size. In this study, we set the minimum cluster size to a value of 0.1 km² in order to remove these look-alikes. After clustering and discrimination, the extent of the dark spots was calculated. The extent of the dark spots detected by the adaptive threshold method was estimated to be 1.87 km².

For the detection of oil spills, the bimodal histogram method was also applied. Fig. 5.2 demonstrates an example of a threshold determined using the bimodal threshold method. A histograms of a window shows a typical form of bimodal distribution. The values of R^2 for Gaussian fitted functions were 0.01 (f_1), 0.51 (f_2), and 0.87 (f_3), respectively. We fitted the histogram to the Gaussian function and found peaks of bimodal distribution.

A threshold in each window was set to the middle point of two peaks. While thresholds determined by the adaptive threshold method vary with a moving window (i.e., a value of threshold decreases as more pixels of oil are included in a window, and vice versa), locations of the peaks in a bimodal histogram are rarely affected by the size of the window. This method is not a subjective method, but rather an objective method that does not require any a prior knowledge of backscattering coefficients as a threshold. It can be automatically determined in a series of algorithms. Thus, the bimodal histogram method is seems to yield a more consistent result. It is known as an elaborate and efficient method for detecting oil spills which are not too thin (Brekke and Solberg, 2005).

For the ENVISAT ASAR image in Fig. 5.3a, we applied the bimodal histogram method described herein and obtained the analysis result of oil spill pixels in Fig. 5.3c. Number 1 corresponds to oil pixels. The two dark spots seem to be relatively well detected in comparison to the original backscattering coefficients (Fig. 5.3a). The result is similar to that obtained with the adaptive threshold method.

In order to illustrate the differences between the two detection methods, we compared the analysis results of the bimodal histogram method with

those of the adaptive threshold method. First of all, we subtracted the flag numbers of Fig. 5.3c from those of Fig. 5.3b. Differences ranged from -1 to 1 as shown in Fig. 5.3d. Dominant differences appeared at the boundaries of the detected dark spots.

The circular pattern in Fig. 5.3d exhibited both positive and negative values for both small and large oil spots. Detailed examination of the oil flags showed that pixels with a difference of 1 were a little larger than those of -1 . The total area of dark spots detected by the bimodal histogram method was estimated to be 1.74 km^2 , which were slightly smaller and more rounded than those detected by the adaptive threshold method.

The distribution of differences between the two methods indicated that the bimodal histogram method has a tendency to somewhat underestimate the extent of oil spills. However, those differences were fairly small, amounting to less than 8% of the total extent of oil spill. Therefore, it can be inferred that there is no substantial difference between the two methods in terms of their results.

Table 5.1. Information of the SAR image used in thresholding detection methods

ENVISAT ASAR	
Frequency (GHz)	5.331 (C-band)
Polarization state	Single-polarization (HH)
Swath width (km)	82.8
Azimuthal range (km)	46.0
Resolution (m)	12.5×12.5
Look angle (deg)	$25.7^\circ - 31.2^\circ$
Acquired time	09h 07m (UTC) on 17 September 2006
Central location	$14.66^\circ\text{E}, 32.82^\circ\text{N}$

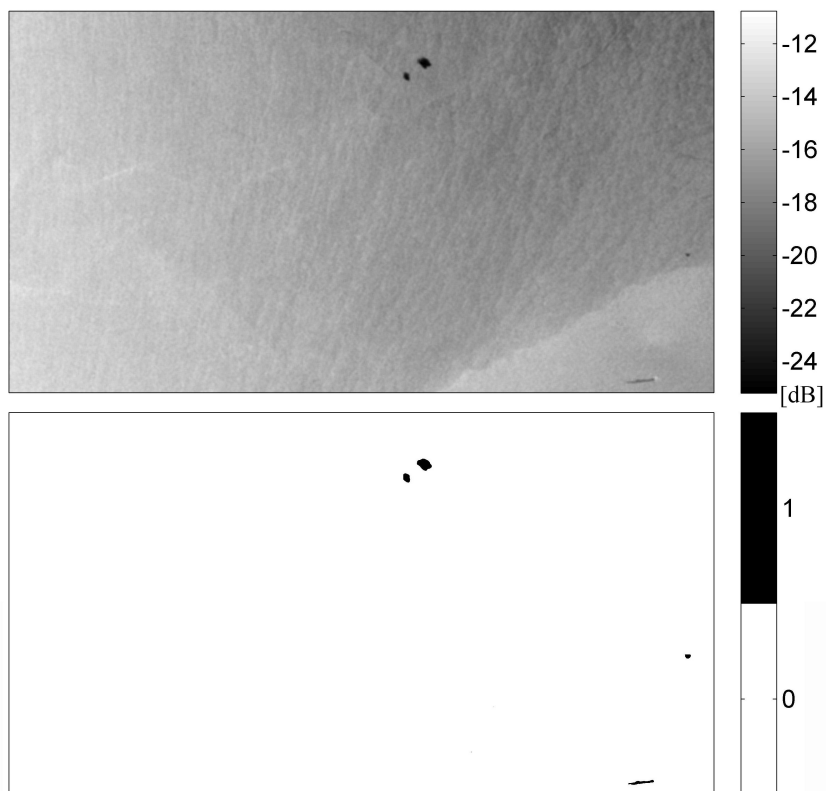


Fig. 5.1. (a) Spatial distribution of ENVISAT backscattering coefficient with oil spill and (b) the analysis results of oil spill pixels using the adaptive threshold method, where 1 is oil and 0 is a non-oil pixel.

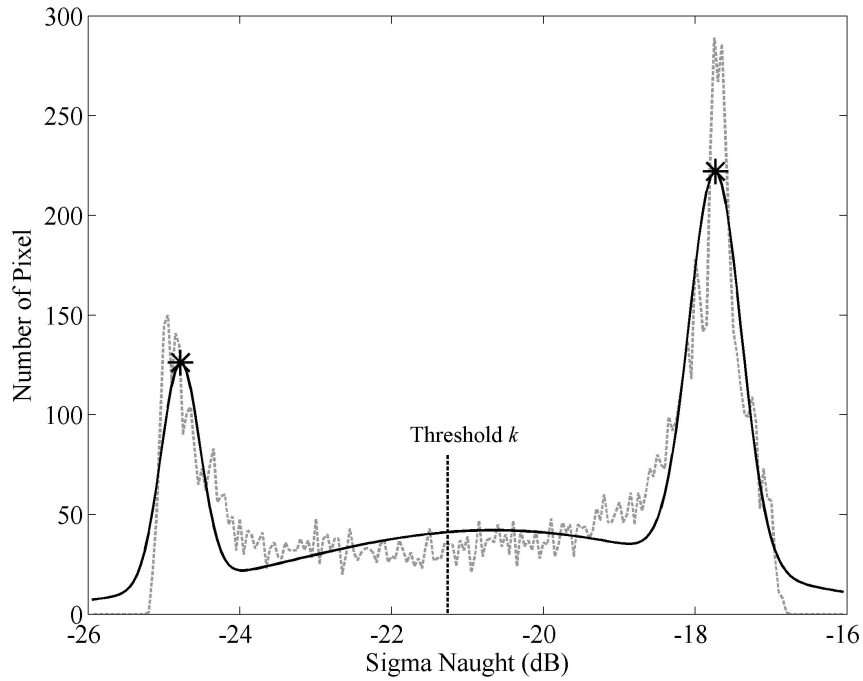


Fig. 5.2. An example of the bimodal histogram method by fitting Gaussian distribution functions with two peaks, marked as stars on the solid fitted line, onto a histogram of backscattering coefficients denoted with a dotted gray line.

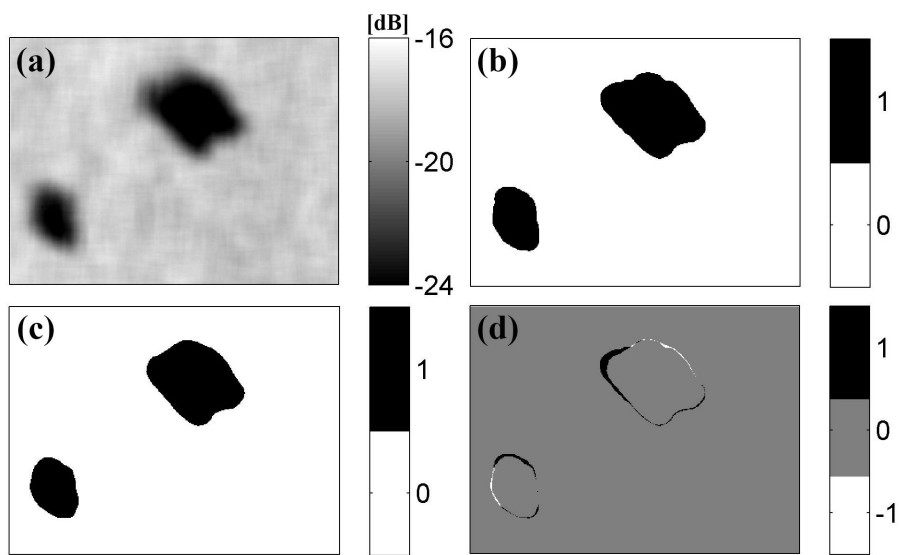


Fig. 5.3. (a) Spatial distribution of backscattering coefficient with oil spill and the analysis results of oil spill pixels using (b) the adaptive threshold method and (c) the bimodal histogram method, where 1 is oil and 0 is a non-oil pixel, and (d) their differences, (b)–(c).

5.2. Oil Spill of the Hebei Spirit by Thresholding Method

Fig. 5.4a presents the NRCS distribution acquired from an Envisat ASAR image at 01h 40m UTC on 11 December 2007. It contained dark pixels with oil slicks and a number of dotted spots with extremely low backscattering coefficients induced by speckle noise. First, we classified oil pixels by applying the adaptive threshold method and eliminated small look-alike dark spots by assigning a minimum cluster size of approximately 0.1 km^2 , as shown in Fig. 5.4b. The area of the dark spots amounted to 1079 km^2 after implementing a rejection scheme to the look-alike pixels. Considerable oil slicks with filament-like shapes extended from approximately 36.5°N to 37.0°N and from 125.7°E to 126.3°E near the Taean peninsula. The area of the slicks tended to be underestimated when compared with that of previous research (approximately 1400 km^2) using the same SAR image. However, the present results based on the objective method were assumed to be more reasonable than the previous study using a subjective adjustment approach.

The methodology of the oil spill required a moderate wind speed to enhance the accuracy of the detection result. Most of the SAR images from 9 to 15 December 2007 satisfied a limit of wind speed of approximately $3.2\text{--}9.1 \text{ m s}^{-1}$. However, the SAR image on 9 December 2007 was not expected to be a good classification due to an extremely low wind speed of approximately 2.9 m s^{-1} , as shown in Fig. 5.5. In general, when the wind speed was less than $2\text{--}3 \text{ m s}^{-1}$, the magnitude of backscattering from the clean sea surface tended to decrease at the sea surface covered with oil

(Bern et al., 1992; Perez-Marrodan, 1998). Similar errors can be generated under inadequately strong winds of approximately $10\text{-}14\text{ m s}^{-1}$ because the damping effect vanishes in the background noise of wind-generated short gravity-capillary waves (Demin et al., 1985; Bern et al., 1992; Litovchenko et al., 1999). In this respect, we investigated if the SAR images were obtained under moderate wind speeds. Three more SAR images (as shown in Figs. 2.2c, 2.2e, and 2.2f), except for the image with significant noise, satisfied the wind conditions. The ALOS PALSAR image acquired on 11 December 2007 in Fig. 2.2d was also utilized in the consecutive processes but excluded in the quantitative analysis because the upper part of main slicks was omitted.

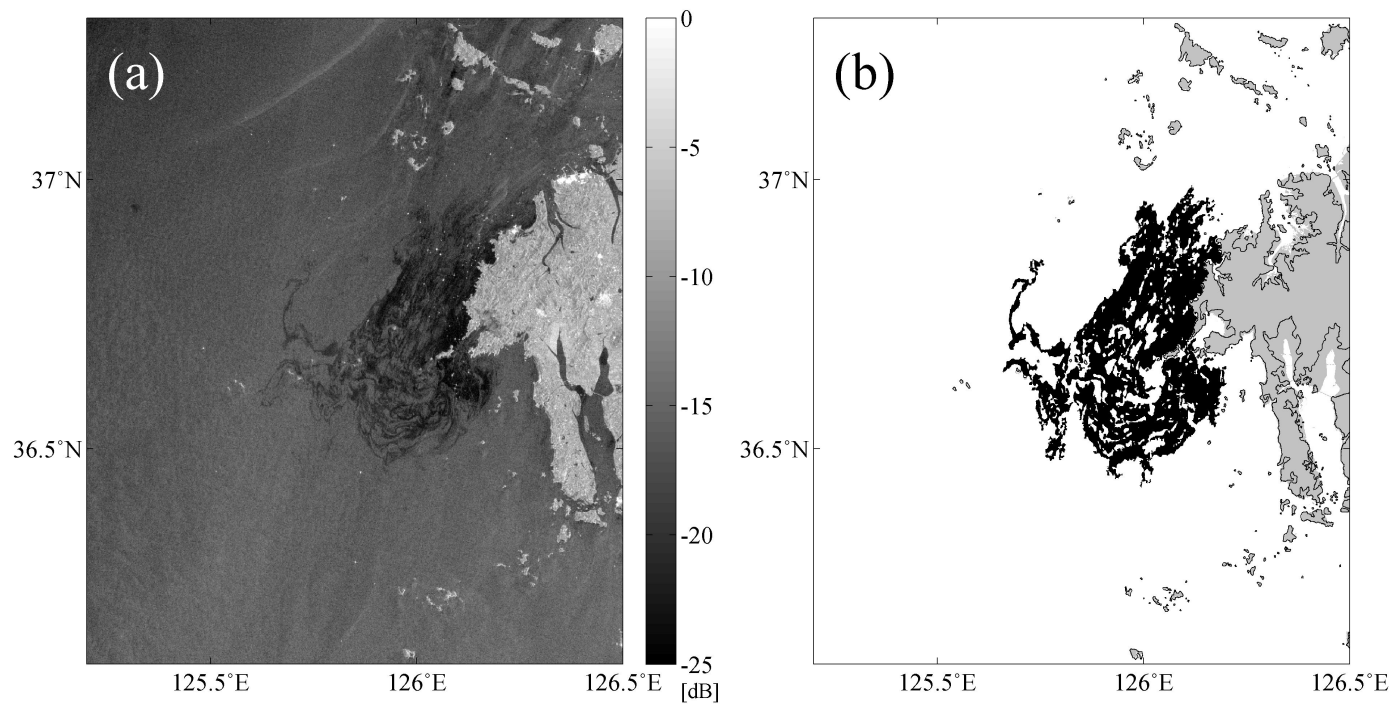


Fig. 5.4. (a) NRCS distribution of an Envisat ASAR image acquired at 01h 40m (UTC) on 11 December 2007, and (b) the detection results by the adaptive threshold method.

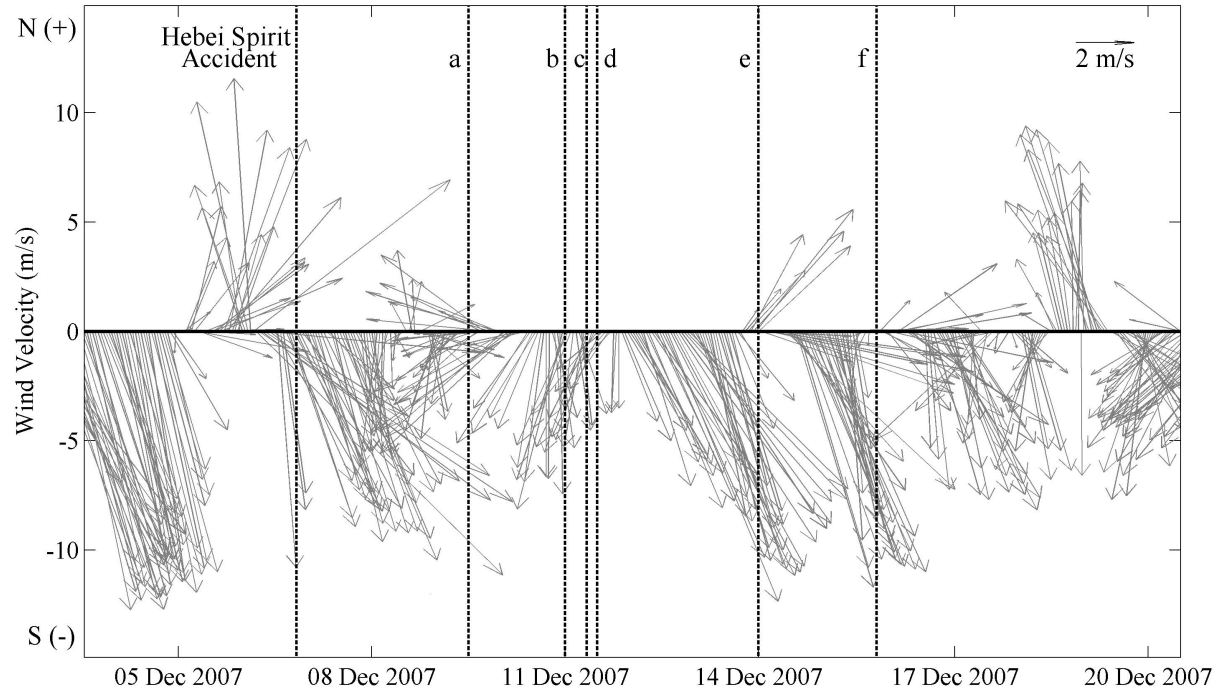


Fig. 5.5. Time series of in-situ wind measurements from the KMA buoy located at 126.02°E , 37.24°N (marked as the black triangle in Fig. 1.6b). The dashed lines indicate the time at the beginning of the Hebei Spirit oil spill accident and the acquisition times of the SAR images (Figs. 2.2a-2.2f).

5.3. Oil Spill by the Hebei Spirit by Neural Network Method

The oil spill detection method that is based on neural network was also applied to investigate the characteristics of the objective methods. Fig. 5.6a shows the result detected from the same image in Fig. 5.4a using the neural network method. Overall, it was well matched with the one from the adaptive threshold method, as illustrated in the main slick with eddy-like shape and some of stretched features on the left side. However, there were discrepancies between the two at the main slick and the coastal region.

For a more detailed comparison, we classified the oil pixels with a value of 1 and the non-oil pixels with a value of 0 for Fig. 5.4b and 5.6a. Fig. 5.6b presents the differences (adaptive threshold-neural network) between the results by the two methods, where a black area with a value of 1 indicates an oil pixel detected by the adaptive threshold only, while the opposite holds true for a gray area with a value of -1 . Overall, the black pixels (1) were congregated near the coast. On the contrary, the gray pixels tended to be scattered along the boundaries of the slicks, as determined by the neural network method, in the offshore and coastal regions. This implied that the neural network method could detect the oil pixels at the edges more adequately than the adaptive threshold method.

In total, the estimated extent of the oil spill, according to the neural network method, was 1094 km^2 , which is slightly larger than that determined by the adaptive threshold method (1079 km^2). Such a difference

of approximately 15 km² can be fairly small, accounting for less than 2% of the total extent of the oil spill. Therefore, it can be inferred that there was no significant difference between the two objective methods.

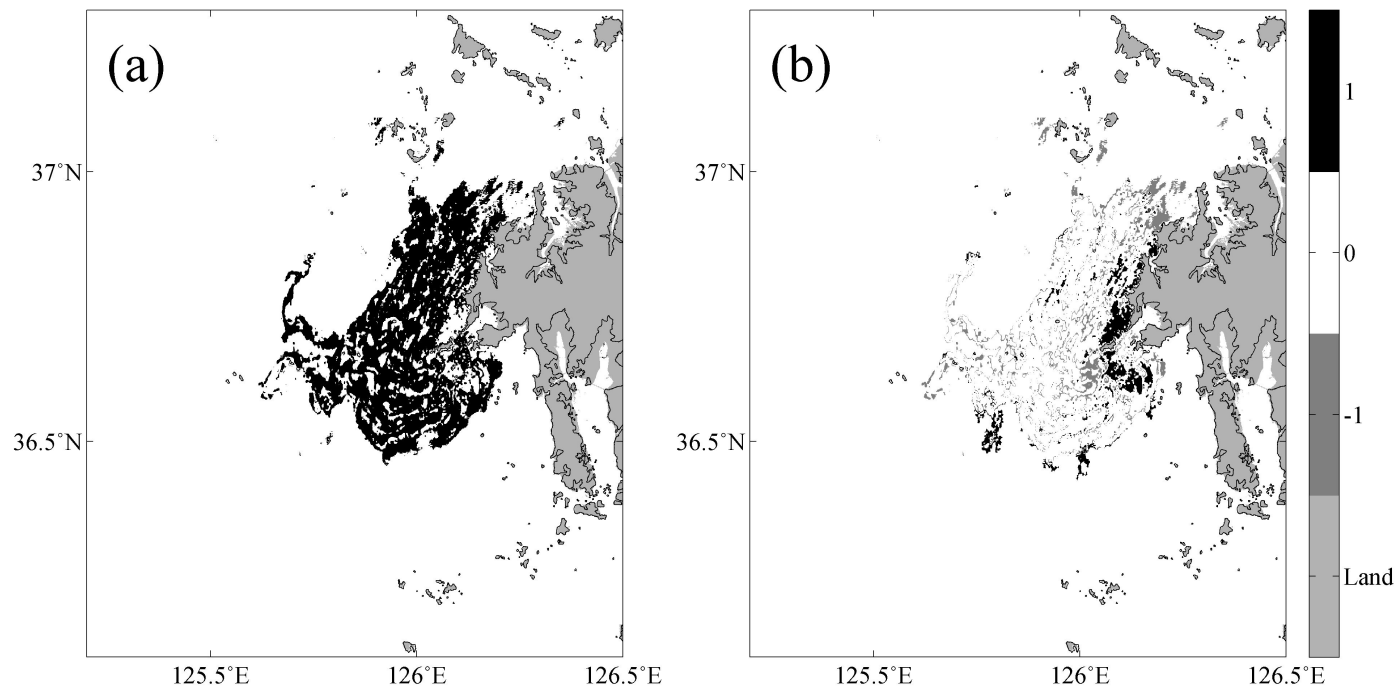


Fig. 5.6. (a) The detection results from the SAR image same as Fig. 5.4a by neural network method, and (b) the differences between the results of the two methods, with the values indicating oil pixels with only the adaptive threshold method (1) or with only the neural network method (-1).

5.4. Differences by Detection Methods

The results from the neural network and adaptive threshold methods showed somewhat of a discrepancy in the estimated extents. Major differences between the two methods were detected at the boundaries of the slicks. Except for some pixels adjacent to the coastal region and the edge of the main slick, the adaptive threshold method tended to underestimate the oil pixels along the boundaries compared to the neural network method. It was assumed that most of the differences possibly originated from the fact that the neural network method was a pixel-based approach, whereas the adaptive threshold method was a window-based one.

In the neural network method, the oil slick candidates were mainly analyzed by applying a predetermined training function to every pixel. This type of method does not usually generate great differences in pixels along a slick body and a boundary. On the contrary, a threshold of the adaptive thresholding method is determined by the distribution of NRCS in a given window, irrespective of the shape of slicks. However, according to the size of the window and the shape of slicks, the patterns of the NRCS distribution tended to remain unimodal, especially when an oil slick had an elongated and irregular shape, which frequently appeared at the boundaries in this case. The tendency found in this study coincided with the previous study by Solberg et al. (2007). The filament-shaped and irregular slicks, which were relatively small compared to the window of interest, could be neglected in the procedure of the adaptive threshold method. Therefore, such differences between the two methods were believed to be substantially

induced by inherent characteristics of the window-based adaptive threshold method.

Chapter 6. Evolution of Oil Spill at the Coastal Region

6.1. Temporal Evolution of the Hebei Spirit Oil Spill

Figs. 6.1a-6.1d present the oil spill detection results by the adaptive threshold method from 11 to 15 December 2007. The oil pixels by the neural network method are presented in Figs. 6.1e-6.1h using the same SAR images as Figs. 6.1a-6.1d. There were no great differences between the results from the two methods, except for the case shown in Fig. 6.1g. The discrepancy between Figs. 6.1c and 6.1g was assumed to be induced by the abrupt discontinuity of the NRCS associated with burst noise in the SAR image (Fig. 2.2e). This may be ascribed to the general characteristics of the noise, which lead to serious problems in the implementation of the neural network method due to uncorrelated variations in the textural features. Excluding the case of Fig. 6.1g, the results detected by both methods showed a high similarity in terms of the overall features of the oil spill pixels. An enormous amount of crude oil leaked in only a few hours after the collision on 6 December 2007, and rapidly spread due to the strong southeastward wind and currents, such that oil slicks appeared widely in the seas around the Taean Peninsula on 11 December 2007 (Figs. 6.1a and 6.1e). The oil slicks dissipated substantially in the region off the coast of Taean (Figs. 6.1b and 6.1f) and then drifted steadily in a similar direction for 4 days, reaching 36.2°N south of the Taean peninsula on 15 December 2007 (Figs. 6.1c, 6.1d, 6.1g, and 6.1h). These results were in good

agreement with the aerial observations made by the Korean Coast Guard. All of the oil pixels were incorporated into the map in Fig. 6.2. The map shows the obvious movement of the main patches of the oil slicks over time. The result from the ALOS PALSAR images, marked as green dots within the rectangular box in Fig. 6.1b, was excluded in the following quantitative analysis because its coverage was restricted at the lower part of the main slicks.

To investigate the evolution of the oil slicks, we obtained the geolocation information by averaging all of the latitudes and longitudes of the oil pixels, as denoted by the red dots in Fig. 6.1. Fig. 6.3a shows the temporal variations of the central positions of oil spill patches from 11 to 15 December 2007, based on the two methods. The two methods showed no great differences in their oil spill estimation results (Fig. 6.3b), which indicated extents of 1079 km² (Fig. 6.1a), 670 km² (Fig. 6.1b), 449 km² (Fig. 6.1c), and 365 km² (Fig. 6.1d) by the adaptive threshold method and 1094 km² (Fig. 6.1e), 702 km² (Fig. 6.1f), and 410 km² (Fig. 6.1h) by the neural network method for the four respective cases (excluding that in Fig. 6.1g). The estimated extents of the oil slicks are summarized in Table 6.1.

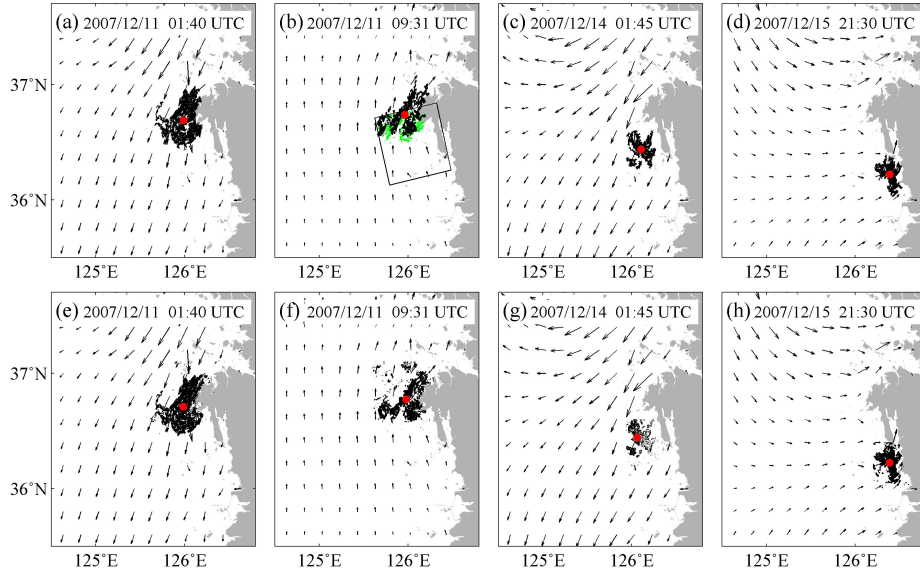


Fig. 6.1. Oil slicks detected by (a)-(d) the adaptive threshold method and by (e)-(h) the neural network method from 11 to 15 December 2007, where the red dots represent the central location of the oil spill and green dots in (b) indicate oil slicks detected from ALOS PALSAR image within the black box acquired on 11 December 2007. The vectors indicate tidal currents from the model data at the same time of the SAR data acquisition.

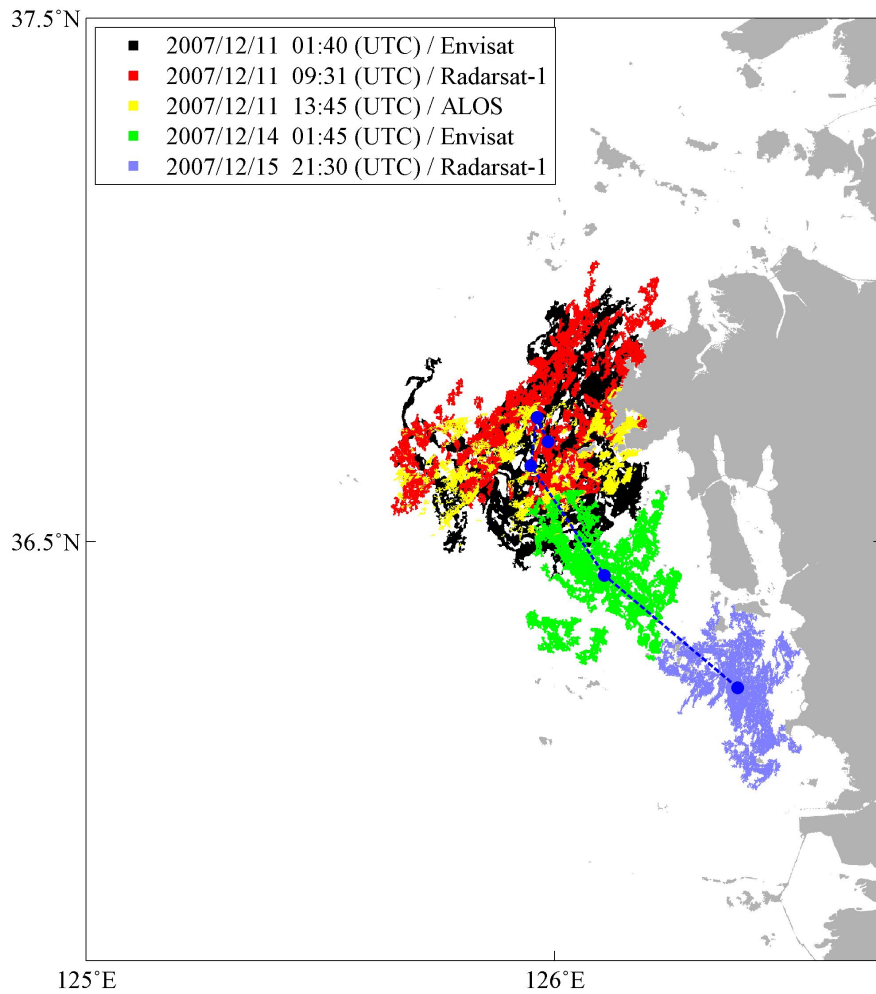


Fig. 6.2. A map of incorporated oil slicks during the period, where each color indicates the result on 11th (black, red, and yellow), 14th (green), and 15th (light purple) December 2007. The blue dots and dashed line indicate the central location of the detected oil spill and its trajectory.

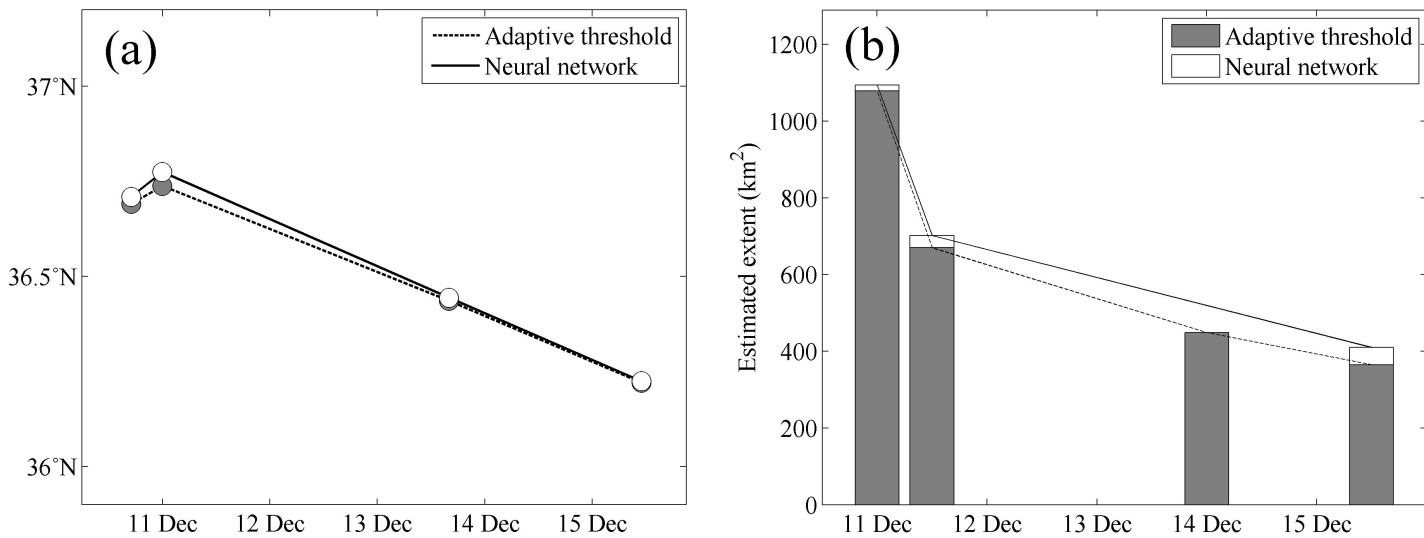


Fig. 6.3. (a) Latitude points (°N) at the central location of the detected oil spill and (b) estimated extents (km²) of the oil spill according to the two methods.

Table 6.1. Estimated extent of the oil spill from SAR images

SAR data	Extent of oil spill (km ²)	
	Adaptive threshold	Neural network
2007/12/11 01:40 (Envisat ASAR)	1079	1094
2007/12/11 09:31 (Radarsat-1)	670	702
2007/12/14 01:45 (Envisat ASAR)	449	-
2007/12/15 21:30 (Radarsat-1)	365	410

6.2. Effect of Artificial Factor on the Evolution

It is noted that the extent of the oil spill abruptly decreased within the first two acquisition times at only 8 hours, after which it decreased at a steady rate (Fig. 6.3b). Except the polarization state (VV-polarization for ENVISAT ASAR image and HH-polarization for Radarsat-1 image), there is no great difference between both SAR images. Both of two SAR images were acquired at C-band frequency and in the moderate incidence angle range (31.7° - 35.4° for the ENVISAT ASAR image and 35.1° - 38.4° for the Radarsat-1 image). As shown in Fig. 5.5, wind speeds and directions maintained almost consistently during the period as well (5.3 m s^{-1} and 10° at the acquisition time of the ENVISAT ASAR image and 5.9 m s^{-1} and 13° for the Radarsat-1 image). In general, the VV image shows more significant contrast of backscattering due to the interaction with the small gravity-capillary waves so that it tends to be more suitable for the detection of oil spills (Migliaccio et al., 2005; Girard-Ardhuin et al., 2005; Migliaccio et al., 2009; Fingas, 2015). But, it has been reported that the detected results by the each polarization state showed a negligible difference less than 5% of the estimated extent (Matkan et al., 2013). Therefore, it is assumed that the abrupt decrease of the oil spills was originated from the change of the environmental factors at the accident site.

In the meantime, this drastic reduction of the oil spill extent was regarded as the consequences from the extensive clean-up work at the time (Kim et al., 2010). However, according to official daily reports from the Korean Coast Guard, the major intensive clean-up efforts took place near

the coastal region, not in the offshore regions. Most of the work was concentrated on preventing the contamination of the mud flats and of fish farming sites along the coast. Moreover, the amounts of the emulsifier used for the removal of the oil spills in the sea declined over time, showing daily values of 24 m³, 20 m³, 3.9 m³, and 4.3 m³ from 8 December, 9 December, 10 December, and 11 December 2007, respectively. This implied that the substantial dissipation of the oil spill that occurred on the first SAR image was mainly induced by other environmental factors, such as strong tidal mixing.

Chapter 7. Effect of Environmental Factors on the Oil Spill

7.1. Effect of Tidal Mixing

The rapid dissipation of oil spills on 11 December 2007 was occurred at the coastal region near Taean peninsula as shown in Fig. 7.1. Unlike aspects of regional clean-up works, the extent of the whole oil slick was decreased at a similar rate irrespective of its location. A ratio of extent changes at the main slick and its boundary was 50.4% (main slick) : 49.6% (boundary). Therefore, it was assumed that environmental factors prevailing at this area induced the dissipation of the oil spill.

The study area off the coast of the Taean peninsula is well known for strong tidal currents throughout the year. The spatial distribution of the tidal fronts in the study area was analyzed to investigate the effects of tidal currents on the evolution of the oil spill. Fig. 7.2 illustrates the contour of the tidal front index $\log_{10}(H/U_{\max}^3)$ on 11 December 2007. Considering the spatial distribution of the index in this particular region, index values lower than 2 were anticipated to be the well-mixed layer due to the effect of the tidal current at the coastal shallow region, which contrasted the offshore region (>2) that was associated with relatively high stratification and weak mixing by the tidal current. One of the lowest indices (about 1.6) was found along the Taean peninsula, where the oil slicks were located on the

same date. This can possibly explain why not a few oil slicks disappeared rapidly during the initial period. The extensive submergence of the oil spills was likely to occur due to the strong vertical mixing by tidal currents in this region during the initial period.

The effect of the strong vertical mixing of the water column by the tidal current can be seen from the vertical structure of the water temperature in summer. Figs. 7.3a and 7.3b present the distributions of the mean sea water temperature (°C) from KODC serial oceanographic observations from 2001 to 2010 along the section at 36.9°N in summer (August) and winter (December). In winter, when the vertical mixing readily occurred due to the shallow bathymetry and strong seasonal northerly winds at that time, a vertically homogenous temperature structure was noted in the coastal region at approximately 126°E, where the tidal front was aligned. In summer, the water column was most strongly stratified (Fig. 7.3a). This implied that tidal mixing had a considerable influence on the sinking of the oil slicks from the sea surface into the water column. Previous literature mentioned the biological impact of the submerged oil droplets on a mass die-off of sea urchins on the sea floor (Lee, 2007). Thus, it is believed that the strong vertical mixing by tidal currents prevailing in this region could have strongly promoted the sinking of the oil slicks, such that the extent of the oil spill decreased rapidly in a short time.

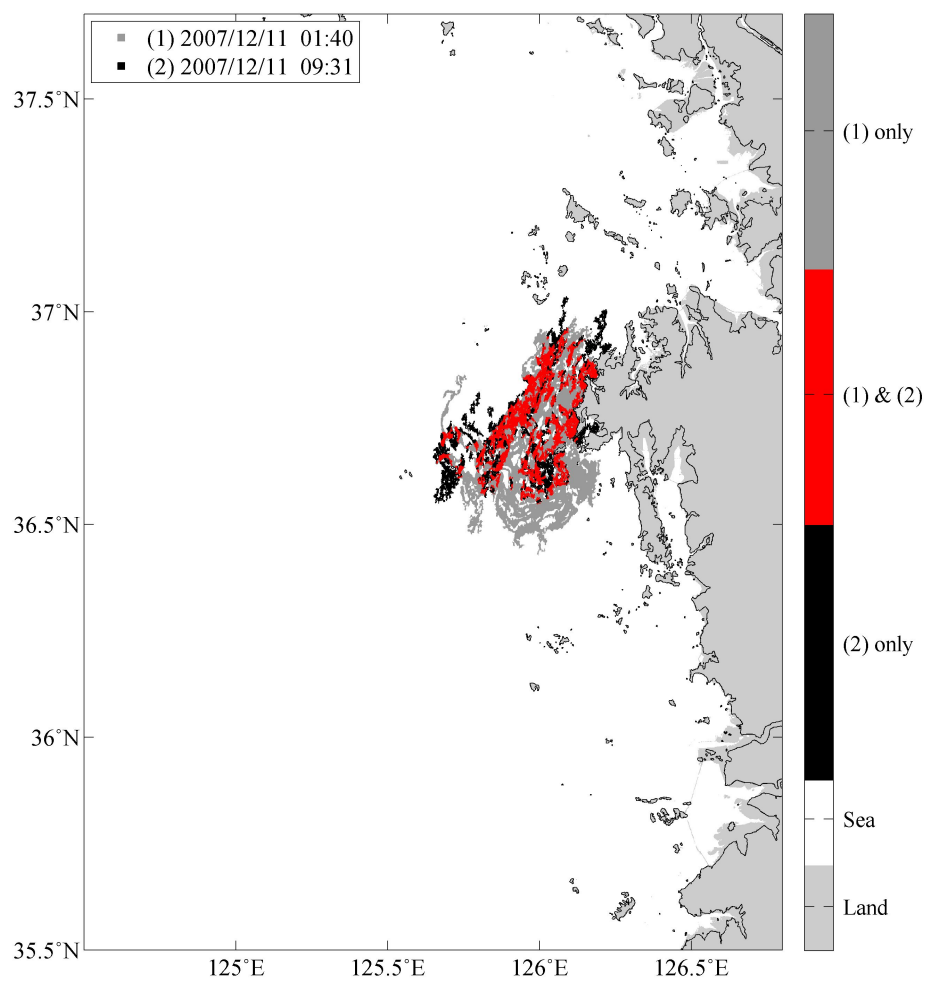


Fig. 7.1 Comparison of detected oil spills at (1) 01h 40m and (2) 09h 31m (UTC) on 11 December 2007.

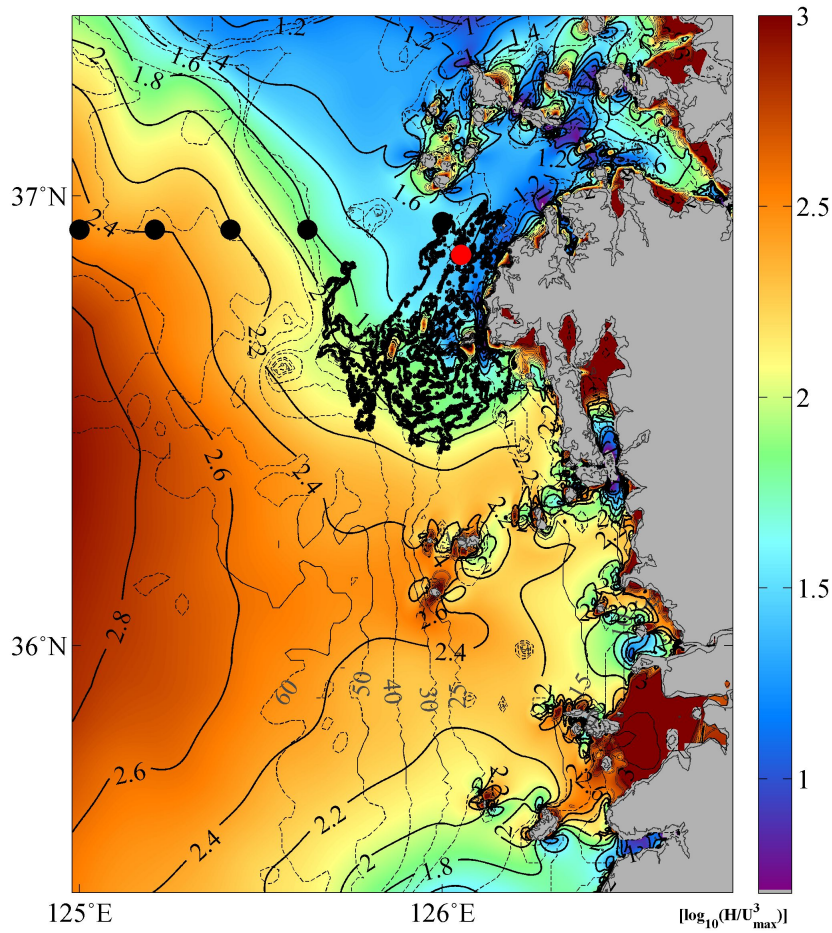


Fig. 7.2. Contour of the tidal mixing parameter $\log_{10}(H/U_{\max}^3)$ on 11 December 2007, where the red and black circles present the locations of the Hebei Spirit collision and KODC stations, respectively. The black solid and dotted lines indicate the contours of the tidal mixing parameter and depth (m), respectively. The black bold line presents the edge of the oil spill at 01h 40m on the same date.

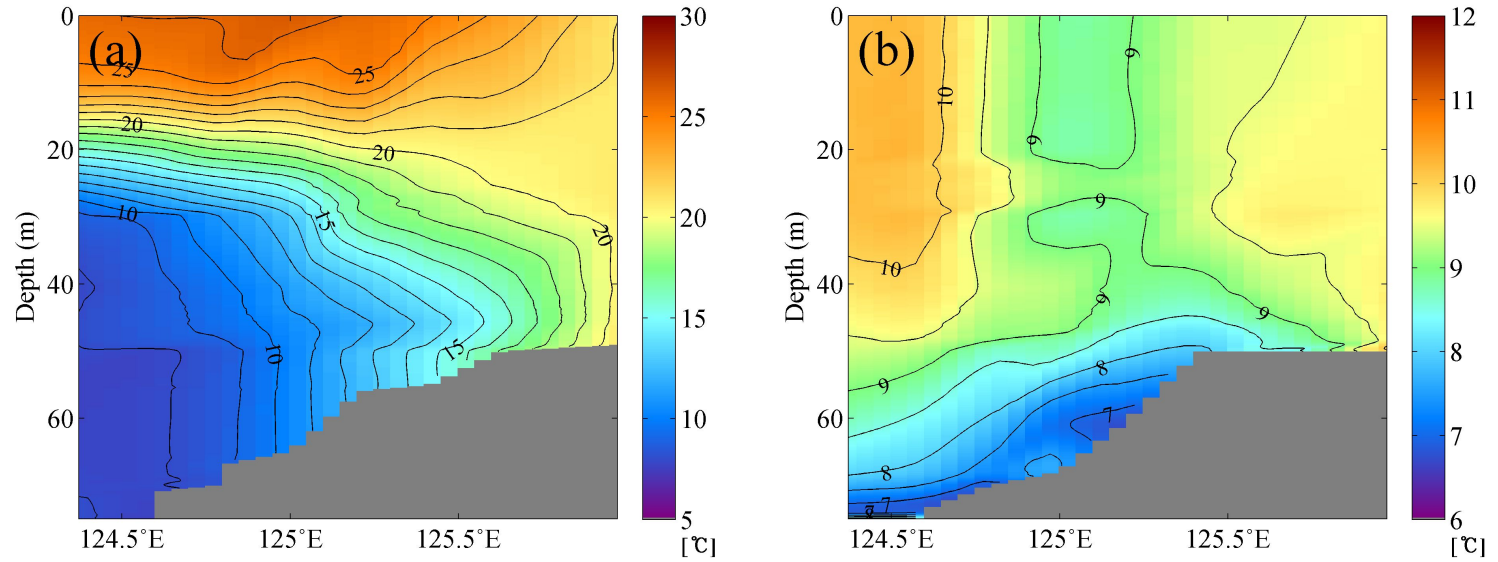


Fig. 7.3. The vertical structure of the mean sea water temperature (°C) from KODC stations along the section of 36.9°N are marked as black dots in Fig. 7.2, in (a) summer (August) and (b) winter (December) from 2001 to 2010.

7.2. Effect of Wind and Tidal Current

The oil slicks moved slightly in the northeast direction at the initial stage and then later moved to the south in the opposite direction (Fig. 6.3a). What caused this peculiar movement at the initial stage of the dispersion of oil slicks? The direction of the movement seemed to be analogous to the typical direction of tidal flows in the region. As shown in Fig. 7.4a, the distribution of the tidal ellipse off the west coast of Korea on 11 December 2007 and a time series of the tidal currents at the collision point of the Hebei Spirit on the same date demonstrated that a significant pattern of a strong northeastward (southwestward) flood (ebb) current prevailed at the upper coastal region, in the vicinity of the collision point over 36.7°N. Furthermore, low winds in the range of 2.5 m s^{-1} to 4.5 m s^{-1} dominated at the KMA buoy station between 1 a.m. and 10 a.m. (Fig. 5.5). Due to the comparatively low wind condition (Fig. 5.5) and the timely strong tidal flow in the region (Fig. 7.4b), the oil spill was expected to drift to the northeast, corresponding to the direction of the flood currents at that time.

After the oil slicks moved to the northeast at the initial stage, they exhibited a significant drift to the south, as shown in the successive images (Fig. 6.2). In addition to the tidal effect, the direction may be related to northerly or northeasterly winds exceeding 7 m s^{-1} (Fig. 5.5). To examine the effect of wind, we estimated the magnitude and direction of the satellite-observed wind field during the study period. Fig. 7.5 presents the spatial distribution of the wind fields from QuikSCAT measurements during the period from 10 to 15 December 2007. At this time of the year,

northwesterly winds associated with the winter monsoon commonly prevailed over the entire study region. The wind field varied at a range of magnitude from 3 m s^{-1} to 15 m s^{-1} . If the oil slicks moved in proportion to the wind speeds, the wide range of winds would have resulted in a different horizontal movement of the oil patches. For an analysis of the role of the wind field on the movements of the oil spill, we compared the drift pattern of the detected oil spill with wind speed and direction (Fig. 7.6).

The directional histograms of scatterometer wind vectors overlaid on the center point of the detected oil spill are shown in Fig. 7.6a. The main directions in the wind diagram were 195° (10 December), 171° (11 December), 121° (14 December), and 157° (15 December) from north clockwise, with the wind varying from NNE to NW. The overall direction showed good agreement with the passage of the oil spill drift, as shown in Fig. 6.2. The rate of the movement of the oil spill (km day^{-1}) showed a linear correlation with the mean wind speed (m s^{-1}) at the time (Fig. 7.6b). The oil spill tended to drift farther as the wind speed increased ($r=0.59$ within 95% confidence level). In addition to the effects of the wind field and tidal mixing on the movement, the tidal currents were believed to be another cause responsible for the oil drift.

The tidal residual currents and Ekman surface drift currents by wind were compared for a more quantitative investigation of the effects (Fig. 7.7). At the time of the Hebei Spirit oil spill, the mean tidal residual current field showed relatively large spatial variations, in which weak flows of less than 3 cm s^{-1} were dominant offshore, while significant southward flows of approximately $7\text{-}8 \text{ cm s}^{-1}$ appeared along the coast near the oil spill area

(Fig. 7.7a). The mean velocities of the tidal residual currents ranged from only 3.2 cm s^{-1} to 3.9 cm s^{-1} during the period. In contrast, the Ekman surface drift was much higher, at approximately 20 cm s^{-1} (Fig. 7.7d).

As shown in Figs. 7.7b and 7.7e, the general directions of both the surface currents driven by the tide and the wind corresponded to the southward and southeastward movements of the oil spill on SAR images. The mean values of the directions at the time were 177.9° (tide) and 153.7° (wind). However, there was a great difference between their magnitudes. Most of the tidal residual current velocities were distributed in a range of less than 5 cm s^{-1} (Fig. 7.7c), while those of the Ekman surface drift current mostly ranged from 10 cm s^{-1} to 25 cm/s (Fig. 7.7f). The mean values of the velocity were 2.0 cm s^{-1} (tide) and 17.0 cm s^{-1} (wind). Although the magnitudes of the Ekman surface current were relatively weak by 11 December 2007, when the mean values were less than 10 cm s^{-1} (8.4 cm s^{-1} for 11 December 2007), this value reached 34.4 cm s^{-1} on 12 December 2007, after which strong flows that exceeded 10 cm/s lasted until 14 December 2007. Therefore, except for the short northeastward drift on 11 December 2007, with low wind and the timely strong tidal flow condition for a short period as described above, it was assumed that the horizontal drift of the oil spill in the area was mainly induced by the winter monsoon.

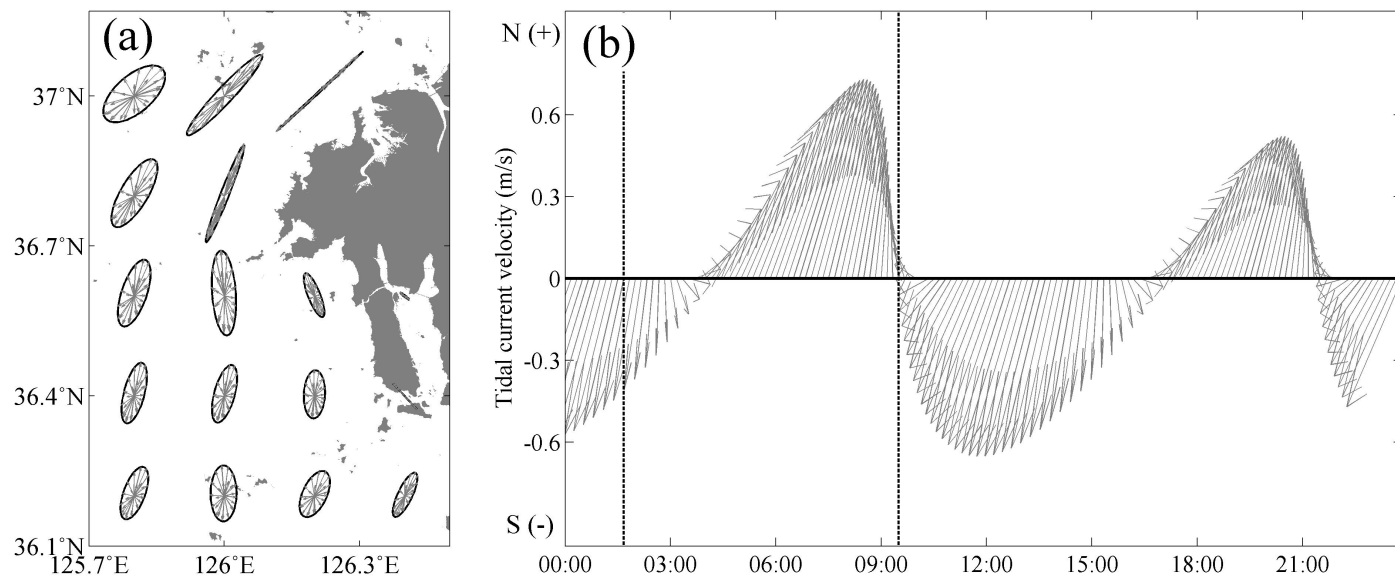


Fig. 7.4. (a) Distribution of the tidal ellipses off the west coast of Korea on 11 December 2007. (b) Time series of the tidal currents at the collision point of the Hebei Spirit on the same day, where the positive (negative) value indicates northward (southward) direction. The two dotted lines indicate the times of 01h 40m and 09h 31m UTC, respectively.

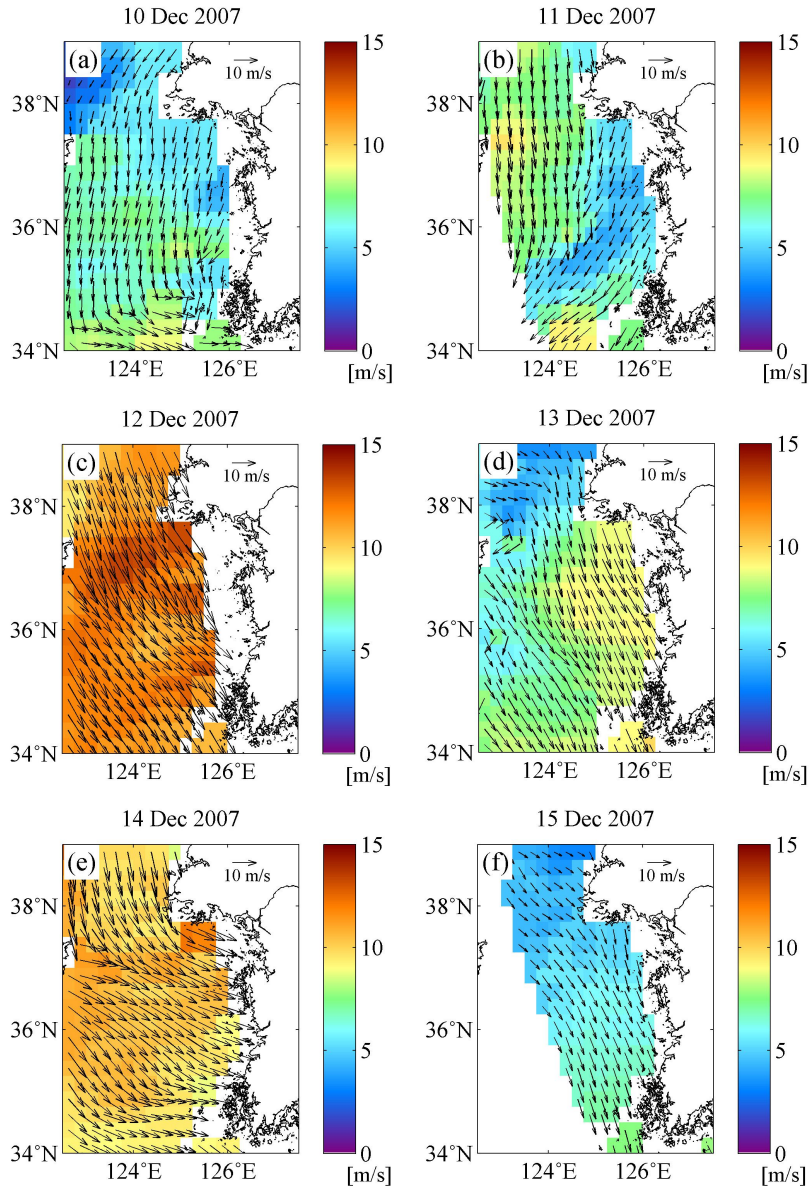


Fig. 7.5. (a) Distributions of the wind vector field off the west coast of Korea from QuikSCAT, where the background colors and arrows indicate the magnitude (m s^{-1}) and the direction of the wind vector, respectively.

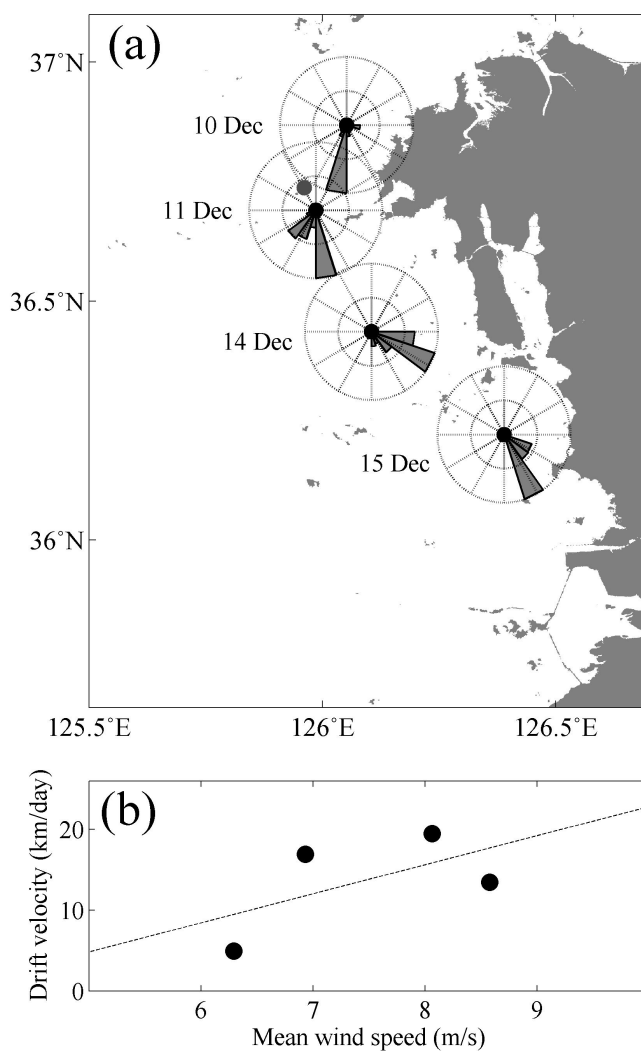


Fig. 7.6. (a) Directional histograms of scatterometer wind vectors centered at the location of the Hebei Spirit collision and the central point of the detected oil spill in SAR images on each date, as marked with a black dot. (b) The relationship between the mean wind speed (m s^{-1}) and the drift velocity (km day^{-1}) of the oil spill.

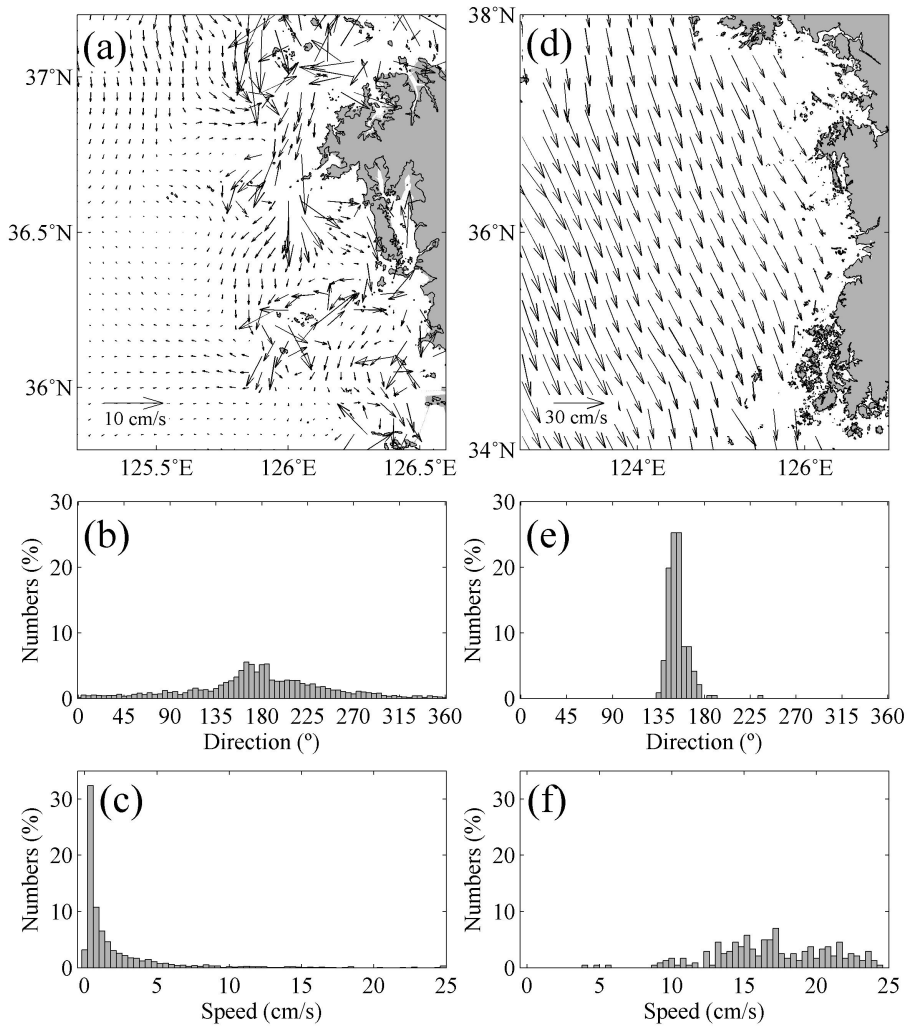


Fig. 7.7. (a) Mean tidal residual current vectors from numerical model data off the western coast of Korea from 10 to 15 December 2007, corresponding histograms of (b) the current directions in degrees from north clockwise, and (c) current speed (cm s^{-1}). (d) Mean Ekman surface drift currents from QuikSCAT winds and their histograms of (e) the directions and (f) speed in the same period as (a)-(c).

Chapter 8. Summary and Conclusion

The SAR-derived wind fields presented the detailed structure of wind fields along the coastal areas, which had heretofore been unobtainable from scatterometer observation. To identify the relationship between the modification of SAR-derived coastal wind data and upwelling events along the east coast of Korea in the EJS, high-resolution coastal wind fields were retrieved from SAR imagery. Comparison of the retrieved SAR wind speeds with in-situ buoy wind measurements showed a small difference of less than 1 m s^{-1} , which implied that the results of SAR wind retrieval satisfied the limit of accuracy of satellite scatterometry.

The retrieved SAR wind fields off the east coast of Korea during August 2007 showed the distinct patterns of low wind along the coastal region. The analysis of SAR wind fields with coincided SST images indicated that these spatial distinctions of SAR wind fields were associated with the upwelling events, which were induced by strong southerly winds in 2007. Based on wind and SST data from satellite data and in-situ measurements, it was found that significant wind-driven upwellings were prevalent in the summer, and that dominant low SSTs along the coastal region appeared to indicate a large difference of air-sea temperature which reached around -6°C .

The low wind speeds may be the result of changes in MABL stability or sea water viscosity. In most of cases, however, it is hard to determine which one is the major factor due to difficulty in distinguishing their contributions from one another. For the more precise comparison, indeed, the additional effect of the modulation of capillary wave induced by the

upwelling should be quantitatively assessed as well. But under the particular circumstance of large air-sea temperature differences, as in the study area, the variation of the radar backscattering near coastal fronts was much higher than the threshold suggested by previous literature. SAR data showed a large backscattering attenuation to SST ratio at the upwelling region, which was much greater than the dependence of water viscosity on radar backscattering, while the wind speed magnitude showed a positive correlation with the difference between SST and air temperature, which indirectly indicated MABL stability. The analyzed results of SAR and SST data provide convincing evidence for this hypothesis. Therefore, it can be concluded that the changes in MABL stability caused by upwelling events dominantly generated the variation of SAR wind fields at the coastal regions.

The upwelling off the east coast of Korea in 2007 took place unprecedentedly due to long-term changes in the atmospheric environment, such as the North Pacific High and tropical depression. According to the previous literature, long-term changes in SST showed a negative trend, that is, the cold water mass would appear more frequently and more strongly at the eastern coast of Korea including the present upwelling region. Moreover, the upwelling activities also induced a significant biological impact on the strong blooms in 2007. Thus, monitoring high-resolution sea surface wind fields and sea surface temperatures will continue to increase in importance when it comes to understanding the process of upwelling and its connection to large-scale and remote forcings.

Oil spills that occur along coastal regions can cause considerable damage

to the environment, marine ecology, and human health. To detect oil spills and monitor their evolution, it is necessary to develop a objective method with an acceptable level of accuracy. Numerous detection techniques for oil spills using SAR data have been developed, with most of the previous examples relying on a threshold method due to its efficient computations, giving this method priority for urgent monitoring. However, the thresholds used tended to be determined subjectively in most cases, leading to inconsistent accuracy levels in the results, depending on the case. Therefore, a more objective method should be adopted for precise oil spill detection.

To verify the applicability of the thresholding methods, this study attempts to apply an additional objective threshold method based on the statistical characteristics of histogram, and then compared the results with those from the adaptive threshold method. The results from two thresholding methods shows good agreement enough for verifying an applicability for oil spill detection in other SAR imagery in other oceanic regions.

In addition, we applied a neural network method to detect the oil slicks resulting from the Hebei Spirit accident and to monitor their evolution. We then compared these results with those from the objective thresholding method. In this comparison, the results from the neural network method used here showed no significant differences, with the exception of negligible small errors at the boundaries of the dark spots used to denote areas of interest. This implied that a method that utilizes a neural network was applicable for oil spill detection purposes with other SAR imagery from other oceanic regions.

We investigated the evolution of the oil spill from the Hebei Spirit

incident and the potential causes of the oil spill evolution based on the results of the two methods. The results clearly showed variations in the extent of the oil spill and its movement as affected by currents and winds. In particular, it also demonstrated that the abrupt reduction in the number of oil slicks on 11 December 2007, left unexplained in the literature, was mainly caused by the effects of strong tidal mixing along the onshore tidal front region in the coastal region of the Yellow Sea. A quantitative comparison of the horizontal drifts by the tide and the wind confirmed that the wind-driven current was the main factor influencing the evolution of this spill on a regional scale.

This study attempted to demonstrate the applicability of SAR on monitoring of oceanic phenomena in the coastal region and interpretation of its mechanisms. Usually coastal regions are frequently covered clouds and fogs in the upwelling period so that it has long been difficult to observe the areas by using optical or IR-sensored satellite observation. In this respect, utilization of SAR data gives opportunities to investigate various oceanic phenomena along the coastal region with its all-weather high-resolution imaging capability. Although it should be dealt with carefully in the interpretation of oceanic features on SAR image, it is anticipated that the applicability of SAR data with the use of other satellite observations and in-situ measurements will contribute to our understanding of the characteristics of small-scale oceanographic phenomena, particularly at coastal areas without satellite scatterometer observations, as well as further our understanding of oceanic dynamics related to air-sea interaction at the sea surface.

Reference

- An, H.S., 1974. On the cold water mass around the southeast coast of Korean peninsula. *The Journal of the Oceanological Society of Korea*, 9(1–2), 10–18.
- Anderson, R.J., 1993. A study of wind stress and heat flux over the open ocean by the inertial-dissipation method. *Journal of Physical Oceanography*, 23, 2153–2161.
- Atkinson, P.M., and Tatnall, A.R.L., 1997. Introduction neural networks in remote sensing. *International Journal of remote sensing*, 18(4), 699–709.
- Bakun, A., 1990. Global climate change and intensification of coastal ocean upwelling. *Science*, 247(4939), 198–201.
- Barth, J.A., and Wheeler, P.A., 2005. Introduction to special section: coastal advances in shelf transport. *Journal of Geophysical Research*, 110, C10S01. doi: 10.1029/2005JC003124.
- Beal, R.C., Gerling, T.W., Irvine, D.E., Monaldo, F.M., and Tilley, D.G., 1986. Spatial variations of ocean surface wave directional spectra. *Journal of Geophysical Research*, 91(C2), 2433–2449.
- Bern, T.-I., Wahl, T., Andersson, T., and Olsen, R., 1992. Oil spill detection using satellite based SAR: Experience from a field

- experiment. *In Proceedings of the first ERS-1 Symposium*, 829–834.
- Bisagni, J.J., and Sano, M.H., 1993. Satellite observations of sea surface temperature variability on southern georges bank. *Continental Shelf Research*, 13, 1045–1064.
- Bourassa, M.A., Vincent, D.G., and Wood, W.L., 1999. A flux parameterization including the effects of capillary waves and sea state. *Journal of the Atmospheric Sciences*, 56(9), 1123–1139.
- Brekke, C., and Solberg, A.H., 2005. Oil spill detection by satellite remote sensing. *Remote Sensing of Environment*, 95(1), 1–13. doi:10.1016/j.rse.2004.11.015.
- Brown, R.A., and Liu, W.T., 1982. An operational large-scale marine planetary boundary layer model. *Journal of Applied Meteorology*, 21(3), 261–269.
- Businger, J.A., and Shaw, W.J., 1984. The response of the marine boundary layer to mesoscale variations in sea-surface temperature. *Dynamics of Atmospheres and Oceans*, 8, 267–280.
- Businger, J.A., Wyngaard, J.C., Izumi, Y., and Bradley, E.F., 1971. Flux - profile relationships in the atmospheric surface layer. *Journal of the Atmospheric Science*, 28, 181–189.
- Campbell, J.W., Blaisdell, J.M., and Darzi, M., 1995. Level-3 SeaWiFS Data Products: Spatial and Temporal Binning Algorithms. In NASA Technical Memorandum 104566, 32, NASA Goddard Space Flight

Center, Maryland.

- Cheng, Y., Li, X., Xu, Q., Garcia-Pineda, O., Andersen, O.B., and Pichel, W.G., 2011. SAR observation and model tracking of an oil spill event in coastal waters. *Marine Pollution Bulletin*, 62(2), 350–363. doi:10.1016/j.marpolbul.2010.10.005.
- Cheng, Y., Liu, B., Li, X., Nunziata, F., Xu, Q., Ding, X., Migliaccio, M., and Pichel, W.G., 2014. Monitoring of oil spill trajectories with COSMO-SkyMed X-band SAR images and model simulation. *IEEE Journal of Selected Topics in Applied Earth Observations and Remote Sensing*, 7(7), 2895–2901. doi:10.1109/JSTARS.2014.2341574.
- Cho, Y.-K., Kim, M.-O., Kim, B.-C., 2000. Sea for around the Korean peninsula. *Journal of Applied Meteorology*, 39(12), 2473–2479.
- Choisnard, J., Bernier, M., and Lafrance, G., 2003. RADARSAT-1 SAR scenes for wind power mapping in coastal area: Gulf of St-Lawrence case. In *Proceedings of IEEE International Geoscience and Remote Sensing Symposium*, 4, 2700–2702.
- Christiansen, M.B., Koch, W., Horstmann, J., Hasager, C.B., and Nielsen, M., 2006. Wind resource assessment from C-band SAR, *Remote Sensing of Environment*, 105(1), 68–81.
- Clemente-Colón, P., 2001. Evolution of upwelling-associated biological features in the middle atlantic bight as captured by SAR, SST, and

ocean color sensors. In *2001 IEEE Geoscience and Remote Sensing Proceedings*, 2616–2618. New Jersey: Institute of Electrical and Electronics Engineers.

Clemente-Colón, P., and Yan, X.-H., 1999. Observations of east coast upwelling conditions in synthetic aperture radar imagery. *IEEE Transactions on Geoscience and Remote Sensing*, 37(5), 2239–2248.

Da Silva, J.C., Jeans, D.R.G., Robinson, I.S., and Sherwin, T.J., 1997. The application of near real-time ERS-1 SAR data to the prediction of the location of internal waves at sea. *International Journal of Remote Sensing*, 18(16), 3507–3517.

Del Frate, F., Petrocchi, A., Lichtenegger, J., and Calabresi, G., 2000. Neural networks for oil spill detection using ERS-SAR data. *IEEE Transactions on Geoscience and Remote Sensing*, 38(5), 2282–2287. doi:10.1109/36.868885.

Demin, B.T., Ermakov, S.A., Pelinovsky, N.Y., Talipova, T.G., and Sheremet'yeva, A.I., 1985. Study of the elastic properties of sea surface-active films. *Atmospheric and Oceanic Physics*, 21, 312–316.

Dobson, F.W., and Vachon, P.W., 1994. The Grand Banks ERS-1 SAR wave spectra validation experiment: Program overview and data summary. *Atmosphere-Ocean*, 32(1), 7–29. doi:10.1080/07055900.1994.9649488.

- Donato, T.F., and Marmorino, G.O., 2002. The surface morphology of a coastal gravity current. *Continental Shelf Research*, 22(1), 141–146.
- Dyer, A.J., 1974. A review of flux-profile relationships. *Boundary-Layer Meteorology*, 7, 363–372.
- Espedal, H.A., and Wahl, T., 1999. Satellite SAR oil spill detection using wind history information. *International Journal of Remote Sensing*, 20(1), 49–65. doi:10.1080/014311699213596.
- Feng, Q., Fang, M., Liu, Y., and Wang, L., 2004. Wind retrieval over the China Seas using satellite synthetic aperture radar. In *Proceedings of IEEE International Geoscience and Remote Sensing Symposium*, 5, 3169–3171.
- Fingas, M., 2015, *Handbook of Oil Spill Science and Technology*, John Wiley & Sons. Inc., New Jersey.
- Fiscella, B., Giancaspro, A., Nirchio, F., Pavese, P., and Trivero, P., 2000. Oil spill detection using marine SAR images. *International Journal of Remote Sensing*, 21(18), 3561–3566. doi:10.1080/014311600750037589.
- Fragiacomo, C., and Parmiggiani, F., 2002. An upwelling event in the Central Mediterranean Sea detected by Quikscat and by AVHRR. *International Journal of Remote Sensing*, 23(24), 5151–5153.
- Friedman, K.S., Sikora, T.D., Pichel, W.G., Clemente-Colón, P., and Hufford, G., 2001. Using spaceborne synthetic aperture radar to

- improve marine surface analyses. *Weather Forecast*, 16, 270–276.
- Furevik, B.R., and Espedal, H.A., 2002. Wind energy mapping using synthetic aperture radar. *Canadian Journal of Remote Sensing*, 28(2), 196–204.
- Gade, M., and Alpers, W., 1999. Using ERS-2 SAR images for routine observation of marine pollution in European coastal waters. *Science of the Total Environment*, 237/238, 441–448.
- Garcia-Pineda, O., MacDonald, I., Li, X., Jackson, C., and Pichel, W., 2013. Oil spill mapping and measurement in the Gulf of Mexico with Textural Classifier Neural Network Algorithm (TCNNA). *IEEE Journal of Selected Topics in Applied Earth Observations and Remote Sensing*, 6(6), 2517–2525. doi:10.1109/JSTARS.2013.2244061.
- Garcia-Pineda, O., Zimmer, B., Howard, M., Pichel, W., Li, X., and MacDonald, I.R., 2009. Using SAR images to delineate ocean oil slicks with a texture-classifying neural network algorithm (TCNNA). *Canadian Journal of Remote Sensing*, 35(5), 411–421. doi:10.5589/m09-035.
- Gasparovic, R.F., Apel, J.R., and Kasischke, E.S., 1988. An overview of the SAR internal wave signature experiment. *Journal of Geophysical Research*, 93(C10), 12304–12316. doi:10.1029/JC093iC10p12304.
- Geernaert, G.L., and Katsaros, K.B., 1986. Incorporation of stratification

effects on the oceanic roughness length in the derivation of the neutral drag coefficient. *Journal of Physical Oceanography*, 16, 1580–1584.

Girard-Ardhuin, F., Mercier, G., Collard, F., and Garello, R., 2005. Operational oil-slick characterization by SAR imagery and synergistic data. *IEEE Journal of Oceanic Engineering*, 30(3), 487–495.

Gonzalez, R.C., Woods, R.E., and Eddins, S.L., 2004. *Digital Image Processing Using Matlab*. Pearson Education Inc., New Jersey.

Guo, X., and Yanagi, T., 1998. Three-dimensional structure of tidal current in the East China Sea and the Yellow Sea. *Journal of Oceanography*, 54, 651–668.

Hagan, M.T., and Menhaj, M., 1994. Training feed-forward networks with the Marquardt algorithm. *IEEE Transactions on Neural Networks*, 5(6), 989–993.

Hagan, M.T., Demuth, H.B., and Beale, M.H., 1996. *Neural Network Design*. PWS Publishing Co., Boston.

Hamrick, J.M., 1996. User's manual for the Environmental Fluid Dynamics Computer Code. The College of William and Mary, Virginia Institute of Marine Science, Virginia.

Hasager, C.B., Dellwik, E., Nielsen, M., and Furevik, B., 2004. Validation of ERS-2 SAR offshore wind-speed maps in the North Sea.

International Journal of Remote Sensing, 25, 3817–3841.

Haykin, S., 1999. *Neural Networks: A Comprehensive Foundation*. Pearson Education Inc., New Jersey.

Hersbach, H., Stoffelen, A., and De Haan, S., 2007. An improved C-band scatterometer ocean geophysical model function: CMOD5. *Journal of Geophysical Research*, 110(C3), C03006. doi:10.1029/2006JC003743.

Hooker, S.B., Esaias, W.E., Feldman, G.G., Gregg, W.W., and McClain, C.R., 1992. An Overview of SeaWiFS and Ocean Color. In NASA Technical Memorandum 104566, 1, NASA Goddard Space Flight Center, Maryland.

Horstmann, J., and Koch, W., 2004. Evaluation of an operational SAR wind field retrieval algorithm for ENVISAT ASAR. In *Proceeding of IEEE International Geoscience and Remote Sensing Symposium*, 1, doi:10.1109/IGARSS.2004.1368940.

Horstmann, J., Koch, W., Lehner, S., and Tonboe, R., 2000. Wind retrieval over the ocean using synthetic aperture radar with C-band HH polarization. *IEEE Transactions on Geoscience and Remote Sensing*, 38(5), 2122–2131.

Horstmann, J., Thompson, D.R., Monaldo, F., Iris, S., and Graber, H.C., 2005. Can synthetic aperture radars be used to estimate hurricane force winds?. *Geophysical Research Letters*, 32, L22801. doi:10.1029/2005GL023992

- Hsu, M.-K., Mitnik, L.M., and Liu, C.-T., 1995. Upwelling area northeast of Taiwan on ERS-1 SAR images. *Acta Oceanographica Taiwanica*, 34(3), 27–38.
- Hu, C., Li, X., Pichel, W.G., and Muller-Karger, F.E., 2009. Detection of natural oil slicks in the NW Gulf of Mexico using MODIS imagery. *Geophysical Research Letters*, 36(1), L01604. doi:10.1029/2008GL036119.
- Isoguchi, O., and Shimada, M., 2009. An L-band ocean geophysical model function derived from PALSAR. *IEEE Transactions on Geoscience and Remote Sensing*, 47, 1925–1936.
- Isoguchi, O., Shimada, M., and Kawamura, H., 2011. Characteristics of ocean surface winds in the Lee of an isolated island observed by synthetic aperture radar. *Monthly Weather Review*. 139(6), 1744–1761.
- Johannessen, J.A., Shuchman, R.A., Digranes, G., Lyzenga, D.R., Wackerman, C., Johannessen, M., and Vachon, P.W., 1996. Coastal ocean fronts and eddies imaged with ERS-1 synthetic aperture radar. *Journal of Geophysical Research*, 101(C3), 6651–6667.
- Jones, B., 2001. A comparison of visual observations of surface oil with synthetic aperture radar imagery of the Sea Empress oil spill. *International Journal of Remote Sensing*, 22(9), 1619–1638. doi:10.1080/713861238.

- Kang, M.-K., and Lee, H., 2007. Estimation of ocean current velocity near Incheon using Radarsat-1 SAR and HF-radar data. *Korean Journal of Remote Sensing*, 23(5), 421–430.
- Kara, A.B., Wallcraft, A.J., and Bourassa, M.A., 2008. Air-sea stability effects on the 10 m winds over the global ocean: Evaluations of air-sea flux algorithms. *Journal of Geophysical Research*, 113, C04009. doi:10.1029/2007JC004324.
- Kawamura, H., Shimada, T., Shimada, M., Kortcheva, A., and Watabe, I., 2002. L-band SAR wind-retrieval model function and its application for studies of coastal surface winds and wind waves. *In Proceedings of IEEE International Geoscience and Remote Sensing Symposium*, 3, 1884–1886.
- Kerbaol, V., Chapron, B., and Queffeulou, P., 1998. Analysis of the wind field during the Vendée Globe race: A kinematic SAR wind speed algorithm. *Earth Observation Quarterly*, 59, 16–19.
- Kim, D.-J., 2009. Wind retrieval from X-band SAR image using numerical ocean scattering model. *Korean Journal of Remote Sensing*, 25(3), 243–253.
- Kim, D.-J., Moon, W.M., and Kim, Y.-S., 2010. Application of TerraSAR-X data for emergent oil-spill monitoring. *IEEE Transactions on Geoscience and Remote Sensing*, 48(2), 852–863. doi:10.1109/TGRS.2009.2036253.

- Kim, D.-S., and Kim, D.-H., 2008. Numerical simulation of upwelling appearance near the southeastern coast of Korea. *Journal of the Korean Society of Marine Environment and Safety*, 14(1), 1–7.
- Kim, J.C., Kim, D.H., and Kim, J.-C., 2003. Observation of coastal upwelling at Ulsan in summer 1997. *Journal of the Korean Society of Oceanography*, 38(3), 122–134.
- Kim, K., Kim, K.-R., Min, D.H., Volkov, Y., Yoon, J.H., and Takematsu, M., 2001. Warming and structural changes in the East (Japan) Sea: a clue to future changes in global oceans?. *Geophysical Research Letters*, 28(17), 3293–3296.
- Kim, S.-W., Go, W.-J., Kim, S.-S., Jeong, H.-D., and Yamada, K., 2010. Characteristics of ocean environment before and after coastal upwelling in the southeastern part of Korean Peninsula using an in-situ and multi-satellite data. *Journal of the Korean Society of Marine Environment and Safety*, 16(4), 345–352.
- Kim, T.H., Yang, C.S., Oh, J.W., and Ouchi, K., 2014. Analysis of the contribution of wind drift factor to oil slick movement under strong tidal condition: Hebei Spirit oil spill case. *PloS one*, 9(1), e87393. doi:10.1371/journal.pone.0087393.
- Kim, T.-R., 1999. Some applications of SAR imagery to the coastal waters of Korea. *Journal of the Korean Society of Remote Sensing*, 15(1), 61–71.

- Kim, T.-S., Park, K.-A., and Moon, W., 2010. Wind vector retrieval from SIR-C SAR data off the east coast of Korea. *Journal of Korean Earth Science Society*, 31(5), 475–487.
- Kim, T.-S., Park, K.-A., Choi, W.-M., Hong, S., Choi, B.-C., Shin, I., and Kim, K.-R., 2012. L-band SAR-derived sea surface wind retrieval off the east coast of Korea and error characteristics. *Korean Journal of Remote Sensing*, 28(5), 477–487.
- Kim, T.S., Park, K.A., Lee, M.S., Park, J.J., Hong, S.W., Kim, K.L., and Chang, E.M., 2013. Application of bimodal histogram method to oil spill detection from a satellite synthetic aperture radar image. *Korean Journal of Remote Sensing*, 29(6), 645–655.
- Klemas, V., 2010. Tracking oil slicks and predicting their trajectories using remote sensors and models: Case studies of the Sea Princess and Deepwater Horizon oil spills. *Journal of Coastal Research*, 26(5), 789–797. doi:10.2112/10A-00012.1.
- Korsbakken, E., Johannessen, J.A., and Johannessen, O.M., 1997. Coastal wind field retrievals from ERS SAR images. In *Proceedings of IEEE International Geoscience and Remote Sensing Symposium*, 3, 1153–1155.
- Lathuilière C., Echevin, V., and Lévy, M., 2008. Seasonal and intraseasonal surface chlorophyll-a variability along the northwest African coast. *Journal of Geophysical Research*, 113, C05007. doi:10.1029/2007JC004433.

- Lee, D.-K., Kwon, J.-I., and Hahn, S.-B., 1998. The wind effect on the cold water formation near Gampo-Ulgi coast. *Journal of the Korean Fisheries Society*, 31(3), 359–371.
- Lee, H.-W., Ji, H.-E., and Lee, S.-H., 2009. A study of interrelationships between the effect of the upwelling cold water and sea breeze in the southeastern coast of the Korean Peninsula. *Journal of Korean Society for Atmospheric Environment*, 25(6), 481–492.
- Lee, J.C., 1983. Variations of sea level and sea surface temperature associated with wind-induced upwelling in the southeast coast of Korea in summer. *Journal of the Oceanological Society of Korea*, 18, 149–160.
- Lee, J.C., 2011. Upwelling-response of the cold water off Haeundae in summer. *Journal of the Korean Society of Oceanography*, 16(4), 206–211.
- Lee, J.C., and Na, J.Y., 1985. Structure of upwelling off the southeast coast of Korea. *Journal of the Oceanological Society of Korea*, 20(3), 6–19.
- Lee, J.C., Kim, D.H., and Kim, J.-C., 2003. Observations of coastal upwelling at Ulsan in summer 1997. *Journal of the Korean Society of Oceanography*, 38(3), 122–134.
- Lee, K.-B., 1978. Study on the coastal cold water near Ulsan. *The Journal of Oceanological Society of Korea*, 13(2), 5–10.

- Lee, Y.-S., 2007. Oil spills spread on sea floor caused a mass mortality of thousands of sea urchin. Seoul Broadcasting System (SBS) News, available from http://news.sbs.co.kr/news/endPage.do?news_id=N1000355406 (in Korean), 27 December 2007.
- Lehner, S., Schulz-Stellenfleth, J., Schattler, B., Breit, H., and Horstmann, J., 2000. Wind and wave measurements using complex ERS-2 SAR wave mode data. *IEEE Transactions on Geoscience and Remote Sensing*, 38(5), 2246–2257.
- Leite, G.C., Ushizima, D.M., Medeiros, F.N.S., and de Lima, G.G., 2010. Wavelet analysis for wind fields estimation. *Sensors*, 10, 5994–6016. doi:10.3390/s100605994.
- Li, X., Pichel, W., Clemente-Colon, P., Krasnopolsky, V., and Sapper, J., 2001. Validation of coastal sea and lake surface temperature measurements derived from NOAA/AVHRR data. *International Journal of Remote Sensing*, 22(7), 1285–1303. doi:10.1080/01431160151144350.
- Li, X., Pichel, W., Maturi, E., Clemente-Colon, P., and Sapper, J., 2001. Deriving the operational nonlinear multi-channel sea surface temperature algorithm coefficients for NOAA-15 AVHRR/3. *International Journal of Remote Sensing*, 22(4), 699–704. doi:10.1080/01431160010013793.
- Li, X., Zhang, J.A., Yang, X., Pichel, W.G., DeMaria, M., Long, D., and Li, Z., 2012. Tropical cyclone morphology from spaceborne

- synthetic aperture radar. *Bulletin of the American Meteorological Society*, 94(2), 215–230. doi:10.1175/BAMS-D-11-00211.1.
- Li, X.M., Li, X.F., and He, M.X., 2009. Coastal upwelling observed by multi-satellite sensors. *Science in China Series D: Earth Sciences*, 52(7), 1030–1038.
- Li, Y., Zhang, Y., Chen, J., and Zhang, H., 2014. Improved compact polarimetric SAR quad-pol reconstruction algorithm for oil spill detection. *IEEE Geoscience and Remote Sensing Letters*, 11(6), 1139–1142. doi:10.1109/LGRS.2013.2288336.
- Li, X., Li, C., Yang, Z., and Pichel, W., 2012. SAR imaging of ocean surface oil seep trajectories induced by near inertial oscillation. *Remote Sensing of Environment*, 130, 182–187. doi: 10.1016/j.rse.2012.11.019.
- Litovchenko, K., Ivanov, A., and Ermakov, S., 1999. Detection of oil slicks parameters from ALMAZ-1 and ERS-1 SAR imagery. *In Proceedings of IEEE International Geoscience and Remote Sensing Symposium*, 3, 1484–1486. doi:10.1109/IGARSS.1999.771995.
- Liu, B., Yang, H., Zhao, Z., and Li, X., 2014. Internal solitary wave propagation observed by tandem satellites. *Geophysical Research Letters*, 41, 2077–2085. doi:10.1002/2014GL059281.
- Liu, G., Yang, X., Li, X., Zhang, B., Pichel, W., Li, Z., and Zhou X., 2013. A Systematic comparison of the effect of polarization ratio

- models on sea surface wind retrieval from C-band synthetic aperture radar. *IEEE Journal of Selected Topics in Applied Earth Observations and Remote Sensing*, 6(3), 1100–1108. doi:10.1109/JSTARS.2013.2242848.
- Liu, P., Li, X., Qu, J.J., Wang, W., Zhao, C., and Pichel, W., 2011. Oil spill detection with fully polarimetric UAVSAR data. *Marine Pollution Bulletin*, 62, 2611–2618. doi:10.1016/j.marpolbul.2011.09.036.
- Liu, P., Zhao, C., Li, X., He, M., and Pichel, W.G., 2010. Identification of ocean oil spills in SAR imagery based on fuzzy logic algorithm. *International Journal of Remote Sensing*, 31(17), 4819–4833. doi:10.1080/01431161.2010.485147.
- Liu, W.T., 1984. The effects of the variations in sea surface temperature and atmospheric stability in the estimation of average wind speed by SEASAT-SASS. *Journal of Physical Oceanography*, 14, 392–402.
- Liu, W.T., and Tang, W., 1996. Equivalent Neutral Wind. In JPL Publication 96-17, NASA Jet Propulsion Laboratory, Pasadena.
- Liu, W.T., Katsaros, K.B., and Businger, J.A., 1979. Bulk parameterization of air-sea exchanges of heat and water vapor including the molecular constraints at the interface. *Journal of the Atmospheric Science*, 36, 1722–1735.

- Lyzenga, D.R., and Marmorino, G.O., 1998. Measurement of surface currents using sequential synthetic aperture radar images of slick patterns near the edge of the Gulf Stream. *Journal of Geophysical Research*, 103, 18769–18777.
- Mao, Y., and Heron, M.L., 2008. The influence of fetch on the response of surface currents to wind studied by HF ocean surface radar. *Journal of Physical Oceanography*, 38, 1107–1121. doi:10.1175/2007JPO3709.1.
- Marín, V.H., Delgado, L.E., and Escribano, R., 2003. Upwelling shadows at Mejillones Bay (northern Chilean coast): A remote sensing, in situ analysis. *Investigaciones Marinas*, 31(2), 47–55.
- Matkan, A.A., Hajeb, M., and Azarakhsh, Z., 2013. Oil spill detection from SAR image using SVM based classification. *In Proceedings of International Archives of the Photogrammetry, Remote Sensing and Spatial Information Sciences*, XL-1/W3, 55–60.
- Matsumoto, K., Takanezawa, T., and Ooe, M., 2000. Ocean tide models developed by assimilating TOPEX/POSEIDON altimeter data into hydrodynamical model: A global model and a regional model around Japan. *Journal of Oceanography*, 56, 567–581.
- McClain, C.R., Pietrafesa, L.J., and Yoder, J.A., 1984. Observations of Gulf stream-induced and wind-driven upwelling in the Georgia bight using ocean color and Infra-red imagery. *Journal of Geophysical Research*, 89, 3705–3723.

- McClain, E.P., 1989. Global sea surface temperatures and cloud clearing for aerosol optical depth estimates. *International Journal of Remote Sensing*, 10(4–5), 763–769. doi:10.1080/01431168908903917.
- McClain, E.P., Pichel, W.G., and Walton, C.C., 1985. Comparative performance of AVHRR-based multichannel sea surface temperatures. *Journal of Geophysical Research*, 90(C6), 11587–11601.
- Mera, D., Cotos, J.M., Varela-Pet, J., and Garcia-Pineda, O., 2012. Adaptive thresholding algorithm based on SAR images and wind data to segment oil spills along the northwest coast of the Iberian Peninsula. *Marine Pollution Bulletin*, 64, 2090–2096. doi:10.1016/j.marpolbul.2012.07.018.
- Migliaccio, M., Gambardella, A., and Tranfaglia, M., 2007. SAR polarimetry to observe oil spills. *IEEE Transactions on Geoscience and Remote Sensing*, 45(2), 506–511. doi:10.1109/TGRS.2006.888097.
- Migliaccio, M., Nunziata, F., and Gambardella, A., 2009. On the co-polarized phase difference for oil spill observation, *International Journal of Remote Sensing*, 30(6), 1587–1602. doi:10.1080/01431160802520741.
- Migliaccio, M., Nunziata, F., Montuori, A., Li, X., and Pichel, W.G., 2011. A multifrequency polarimetric SAR processing chain to observe oil fields in the Gulf of Mexico. *IEEE Transactions on Geoscience and Remote Sensing*, 49(12), 4729–4737. doi:10.1109/TGRS.2011.2158828.
- Migliaccio, M., Tranfaglia, M., and Ermakov, S.A., 2005. A physical approach

- for the observation of oil spills in SAR images. *IEEE of Oceanic Engineering*, 30(3), 496–507.
- Minchew, B., 2012. Determining the mixing of oil and sea water using polarimetric synthetic aperture radar. *Geophysical Research Letters*, 39, L16607. doi:10.1029/2012GL052304.
- Ministry of Land, Transport and Maritime Affairs of Korea (MLTM), 2008. Environmental impact assessment of the Hebei Spirit oil spill. MLTM report number 11-1611000-000392-01 (in Korean).
- Monaldo, F.M., Li, X., Pichel, W.G., and Jackson, C.R., 2014. Ocean wind speed climatology from spaceborne SAR imagery. *Bulletin of the American Meteorological Society*, 95(4), 565–569. doi:10.1175/BAMS-D-12-00165.1.
- Monaldo, F.M., Thompson, D.R., Beal, R.C., Pichel, W.G., and Clemente-Colon, P., 2001. Comparison of SAR-derived wind speed with model predictions and ocean buoy measurements. *IEEE Transactions on Geoscience and Remote Sensing*, 39(12), 2587–2600.
- Monaldo, F.M., Thompson, D.R., Beal, R.C., Pichel, W.G., and Clemente-Colon, P., 2002. Comparison of SAR-derived wind speed with model predictions and ocean buoy measurements. *IEEE Transactions on Geoscience and Remote Sensing*, 39(12), 2587–2600.
- Moon, W.M., Staples, G., Kim, D.J., Park, S.E., and Park, K.A., 2010.

- RADARSAT-2 and coastal applications: Surface wind, waterline, and intertidal flat roughness. *Proceedings of the IEEE*, 98(5), 800–815.
- Nirchio, F., Sorgente, M., Giancaspro, A., Biamino, W., Parisato, E., Ravera, R., and Trivero, P., 2005. Automatic detection of oil spills from SAR images. *International Journal of Remote Sensing*, 26(6), 1157–1174. doi:10.1080/01431160512331326558.
- Nunziata, F., Migliaccio, M., and Li, X., 2014. Sea oil slick observation using hybrid-polarity SAR architecture. *IEEE Journal of Oceanic Engineering*, 40(2), 426–440. doi:10.1109/JOE.2014.2329424.
- Nykjaer, L., and Van Camp, L., 1994. Seasonal and interannual variability of coastal upwelling along northwest Africa and Portugal from 1981 to 1991. *Journal of Geophysical Research*, 99(C7), 14197–14207.
- Park, K.-A., and Kim, K.-R., 2010. Unprecedented coastal upwelling in the East/Japan sea and linkage to long term large scale variations. *Geophysical Research Letters*, 37, L09603. doi:10.1029/2009GL042231.
- Park, K.-A., Cornillon, P., and Codiga, D.L., 2006. Modification of surface winds near ocean fronts: Effects of Gulf Stream rings on scatterometer (QuikSCAT, NSCAT) wind observations. *Journal of Geophysical Research*, 111, C03021. doi:10.1029/2005JC003016.
- Park, K.-A., Lee, E.-Y., Li, X., Chung, S.-R., Sohn, E.-H., and Hong, S., 2015. NOAA/AVHRR sea surface temperature accuracy in the

East/Japan Sea. *International Journal of Digital Earth*, 8(10), 784–804. doi:10.1080/17538947.2014.937363.

Paulson, C.A., 1970. The mathematical representation of wind speed and temperature profiles in the unstable atmospheric surface layer. *Journal of Applied Meteorology*, 9(6), 857–861.

Pawlowicz, R., Beardsley, B., and Lentz, S., 2002. Classical tidal harmonic analysis including error estimates in MATLAB using T_TIDE. *Computers and Geosciences*, 28, 929–937.

Peixoto, J.P., and Oort, A.H., 1992. *Physics of Climate*. American Institute of Physics, New York.

Perez-Marrodan, M., 1998. ENVISYS environmental monitoring warning and emergency management system. In *Proceedings of the AFCEA Kiev Seminar*, 122–132. doi:10.1016/S1353-2561(96)00023-0.

Pradhan, Y., Lavender, S.J., Hardman-Mountford, N.J., and Aiken, J., 2006. Seasonal and inter-annual variability of chlorophyll-a concentration in the Mauritanian upwelling: observation of an anomalous event during 1998 - 1999. *Deep Sea Research Part II*, 53, 1548–1559.

Romeiser, R., Breit, H., Eineder, M., and Runge, H., 2002. Demonstration of current measurements from space by along-track SAR interferometry with SRTM data. In *Proceedings of IEEE International Geoscience and Remote Sensing Symposium*, 1, 158-160.

- Santos, M.P., Kazmin, A.S., and Peliz, A., 2005. Decadal changes in the canary upwelling system as revealed by satellite observations: their impact on productivity. *Journal of Marine Research*, 63(2), 359–379.
- Shen, H., Perrie, W., and He, Y., 2007. On SAR hurricane wind speed ambiguities. In *Proceedings of IEEE International Geoscience and Remote Sensing Symposium*, 2531–2534. doi:10.1109/IGARSS.2007.4423359.
- Shi, L., Ivanov, A.Y., He, M., and Zhao, C., 2008. Oil spill mapping in the western part of the East China Sea using synthetic aperture radar imagery. *International Journal of Remote Sensing*, 29(21), 6315–6329. doi:10.1080/01431160802175447.
- Shimada, M., Nakatani, H., Isono, K., and Kawada, T., 1999. Removal of the interference appeared within the SAR image. *Advances in Space Research*, 23, 1505–1508.
- Shimada, T., 2010. Structures and seasonal variations of surface winds blowing through the Tsushima strait. *Journal of Applied Meteorology and Climatology*, 49, 1714–1727. doi:10.1175/2010JAMC2301.1.
- Simpson, J.H., and Hunter, J.R., 1974. Fronts in the Irish Sea. *Nature*, 250, 404–406. doi:10.1038/250404a0.
- Singha, S., Bellerby, T.J., and Trieschmann, O., 2013. Satellite oil spill

- detection using artificial neural networks. *IEEE Journal of Selected Topics in Applied Earth Observations and Remote Sensing*, 6(6), 2355–2363. doi:10.1109/JSTARS.2013.2251864.
- Skøelv, Å., and Wahl, T., 1993. Oil spill detection using satellite based SAR. Phase 1B Competition Report, Technical Report, Norwegian Defence Research Establishment, Norway.
- Smith, R.L., 1968. Upwelling. In *Oceanography and Marine Biology-An Annual Review*, 6, George Allen and Unwin, London.
- Solberg, A.H.S., Brekke, B., and Husoy, P.O., 2007. Oil spill detection in Radarsat and Envisat SAR images. *IEEE Transactions on Geoscience and Remote Sensing*, 45(3), 746–755. doi:10.1109/TGRS.2006.887019.
- Solberg, A.H.S., Storvik, G., Solberg, R., and Volden, E., 1999. Automatic detection of oil spills in ERS SAR images. *IEEE Transactions on Geoscience and Remote Sensing*, 37(4), 1916–1924. doi:10.1109/36.774704.
- Stoffelen, A., and Anderson, D., 1997. Scatterometer data interpretation: Estimation and validation of the transfer function CMOD4. *Journal of Geophysical Research*, 102(C3), 5767–5780. doi:10.1029/96JC02860.
- Strong, A., and McClain, E.P., 1984. Improved ocean surface temperatures from space—Comparisons with drifting buoys. *Bulletin of the*

American Meteorological Society, 65(2), 138–142. doi:10.1175/1520-0477(1984)065<0138:IOSTFS>2.0.CO;2.

Suh, Y.S., Jang, L.-H., and Hwang, J.D., 2001. Temporal and spatial variations of the cold waters occurring in the eastern coast of the Korean Peninsula in summer season. *Korean Journal of Fisheries and Aquatic Sciences*, 34(5), 435–444.

Svejkovsky, J., and Shandley, J., 2001. Detection of offshore plankton blooms with AVHRR and SAR imagery. *International Journal of Remote Sensing*, 22(2–3), 471–485.

Svozil, D., Kvasnicka, V., and Pospichal, J., 1997. Introduction to multi-layer feed-forward neural networks. *Chemometrics and Intelligent Laboratory Systems*, 39(1), 43–62.

Takeoka, H., Kaneda, A., and Anami, H., 1997. Tidal fronts induced by horizontal contrast of vertical mixing efficiency. *Journal of Oceanography*, 53, 563–570.

Taravat, A., Latini, D., and Del Frate, F., 2014. Fully automatic dark-spot detection from SAR imagery with the combination of nonadaptive weibull multiplicative model and pulse-coupled neural networks. *IEEE Transactions on Geoscience and Remote Sensing*, 52(5), 2427–2435. doi:10.1109/TGRS.2013.2261076.

Thomas, A.C., Blanco, J.L., Carr, M.E., Strub, P.T., and Osses, J., 2001. Satellite-measured chlorophyll and temperature variability off

- northern Chile during the 1996 - 1998 La Niña and El Niño. *Journal of Geophysical Research*, 106(C1), 899–915.
- Thompson, D., Elfouhaily, T., and Chapron, B., 1998. Polarization ratio for microwave backscattering from the ocean surface at low to moderate incidence angles. In *Proceedings of IEEE International Geoscience and Remote Sensing Symposium*, 3, 1671–1673. doi:10.1109/IGARSS.1998.692411.
- Topouzelis, K.N., 2008, Oil spill detection by SAR images: dark formation detection, feature extraction and classification algorithms. *Sensors*, 8, 6642–6659. doi:10.3390/s8106642.
- Turrell, W.R., 1994. Modelling the Braer oil spill - A retrospective view. *Marine Pollution Bulletin*, 28(4), 211–218.
- Turrell, W.R., 1995. Modelling the Braer oil spill—A comment on Proctor et al. (1994). *Marine Pollution Bulletin*, 30(1), 92–93.
- Uiboupin, R., and Laanemets, J., 2009. Upwelling characteristics derived from satellite sea surface temperature data in the Gulf of Finland, Baltic sea. *Boreal Environment Research*, 14, 297–304.
- Vachon, P., and Dobson, F., 2000. Wind retrieval from RADARSAT SAR images: selection of a suitable C-band HH polarization wind retrieval model. *Canadian Journal of Remote Sensing*, 26(4), 306–313.
- Vachon, P.W., Thomas, S.J., Cranton, J.A., Bjerkelund, C., Dobson, F.W.,

- and Olsen, R.B., 1998. Monitoring the coastal zone with the RADARSAT satellite. *In Proceedings of Oceanology International*, 98, 29–38.
- Van Camp, L., Nykjaer, L., Mittelstaedt, E., and Schlittenhardt, P., 1991. Upwelling and boundary circulation off northwest Africa as depicted by infrared and visible satellite observations. *Progress in Oceanography*, 26(4), 357–402.
- Vandemark, D., Vachon, P.W., and Chapron, B., 1998. Assessment of ERS-1 SAR wind speed estimates using an airborne altimeter. *Earth Observation Quarterly*, 59, 5–8.
- Velotto, D., Migliaccio, M., Nunziata, F., and Lehner, S., 2011. Dual-polarized TerraSAR-X data for oil-spill observation. *IEEE Transactions on Geoscience and Remote Sensing*, 49(12), 4751–4762. doi:10.1109/TGRS.2011.2162960.
- Wackerman, C., Rufenach, C., Schuchman, R., Johannessen, J., and Davidson, K., 1996. Wind vector retrieval using ERS-1 synthetic aperture radar imagery. *Journal of Geophysical Research*, 34, 1343–1352. doi:10.1109/36.544558.
- Weissman, D.E., 1990. Dependence of the microwave radar cross section on ocean surface variables: comparison of measurements and theory using data from the frontal air-sea interaction experiment. *Journal of Geophysical Research*, 95(C3), 3387–3398.

- Xu, Q., Li, X., Wei, Y., Tang, Z., Cheng, Y., and Pichel, W.G., 2013. Satellite observations and modeling of oil spill trajectories in the Bohai Sea, *Marine Pollution Bulletin*, 71(1–2), 107–116. doi:10.1016/j.marpolbul.2013.03.028.
- Yang, C.S., Kim, D.Y., and Oh, J.H., 2009. Study on improvement of oil spill prediction using satellite data and oil-spill model: Hebei Spirit oil spill. *Korean Journal of Remote Sensing*, 25(5), 435–444.
- Yang, X., Li, X., Pichel, W.G., and Li, Z., 2011. Comparison of ocean surface winds from ENVISAT ASAR, Metop ASCAT scatterometer, buoy measurements and NOGAPS model. *IEEE Transactions on Geoscience and Remote Sensing*, 49(12), 4743–4750. doi:10.1109/TGRS.2011.2159802.
- Yang, X., Li, X., Zheng, Q., Gu, X., Pichel, W.G., and Li, Z., 2011. Comparison of ocean surface winds retrieved from QuikSCAT scatterometer and Radarsat-1 SAR in offshore waters of the US West Coast. *IEEE Geoscience and Remote Sensing Letters*, 8(1), 163–167. doi:10.1109/LGRS.2010.2053345
- Yeom, J.-M., Han, K.-S., Kim, Y.-S., and Jang, J.-D., 2008. Neural network determination of cloud attenuation to estimate insolation using MTSAT-1R data. *International Journal of Remote Sensing*, 29(21), 6193–6208. doi:10.1080/01431160802175421.
- Young, G.S., Sikora, T.D., Winstead, N.S., 2000. Inferring marine atmospheric boundary layer properties from spectral characteristics of

satellite-borne SAR imagery. *Monthly Weather Review*, 128, 1506 – 1520.

Zabeline, V., Neil, L., Perrie, W., Vachon, P.W., Fogarty, C., Khurshid, S.K., Komarov, S., and Zhang, B., 2011. RADARSAT application in ocean wind measurements. *In Proceedings of IEEE International Geoscience and Remote Sensing Symposium*, 3622 – 3625.

Zhang, B., Perrie, W., Li, X., and Pichel, W.G., 2011. Mapping sea surface oil slicks using RADARSAT-2 quad-polarization SAR image. *Geophysical Research Letters*, 38, L10602. doi:10.1029/2011GL047013.

Zheng, Q., Yan, X.-H., Ho, C.-R., Klemas, V., Wang, Z., and Kuo, N.-J., 1998. Coastal lee waves on ERS-1 SAR images. *Journal of Geophysical Research*, 103(C4), 7979 – 7993.

Zheng, Q., Yan, X.-H., Klemas, V., Huang, N.E., Pan, J.-Y., and Yuan, Y.-I., 1995. Laboratory measurements of the effects of viscosity on short water wave spectra and implication for radar remote sensing of the ocean surface. *Chinese Journal of Oceanology and Limnology*, 13(3), 193 – 205.

국문 요약

본 논문은 한반도 주변해 연안 해양 현상 이해에 대한 합성개구 레이더(SAR)의 활용가능성을 제시한다. 이를 위해 SAR 산출 연안 해상풍의 시공간 변동성 및 SAR 영상에 나타난 대규모 기름유출 사고의 분포 변동 양상과 대기-해양 환경요인의 관계성을 실측 및 위성관측자료를 활용해 정량적으로 분석하였다.

2007년 8월 용승 시기 동해 연안을 관측한 고해상도 SAR 바람장 산출 결과, 연안을 따라 풍속 분포 차이가 나타났다. 이러한 연안의 저풍속대 영역은 용승으로 인한 냉수대 분포와 일치하였으며, 풍속과 수온 시계열 실측자료 분석 결과를 통해 해당 시기 연안용승 현상은 바람장으로 인해 발생했음을 밝혔다. SAR 자료에 나타난 이 지역의 수온 대비 후방산란계수 감소율은 $1.2 \text{ dB } ^\circ\text{C}^{-1}$ 로 일반적으로 알려진 점성도 효과보다 상대적으로 매우 큰 값을 보였다. 또한 용승 지역의 풍속 변화는 해수면과 대기 온도차와 뚜렷한 양의 상관관계를 나타냈다. 이는 동해 용승 시기 SAR 바람장에서 나타나는 저풍속대가 주로 대기-해양 온도차로 인한 대기안정도 변화에 의한 것임을 의미한다.

SAR 영상을 활용하여 서해 태안 연안에서 발생한 허베이 스피리트호 사고 당시의 기름유출영역을 탐지하고 그 시공간 변동특성을 분석하였다. 정량적 분석을 위해 최적임계값과 인공신경망을 기반으로 한 객관적 탐지기법을 비교 검증한 후 적용하였다. 각 기법들의 탐지결과는 경계지역의 미미한 차이를 제외하고는 큰 차

이를 보이지 않았으며 면적산출과 궤적 추적을 하기에 충분한 수준의 결과를 보였다. 탐지 결과의 정량적 분석 결과, 유출된 기름은 당시 서해 겨울철의 바람과 조류의 흐름에 따른 남동향 이동 패턴을 보였으며, 유출 초기 단시간 내의 대규모 감소를 제외하고는 유출면적이 지속적으로 일정하게 감소하는 경향이 나타났다. 조석혼합지수 비교를 통해 초기 면적감소는 태안 연안 조석전선역 내의 강한 조석혼합 영향에 의한 것임을 밝혔다. 또한 기름유출영역 이동에 대한 풍속과 조류의 영향을 정량적으로 검증하였으며 조석잔차류보다 에크만 취송류의 영향이 더 큰 것으로 나타났다.

주요어: SAR, 해상풍, 용승, 안정도 효과, 기름유출, 허베이 스피리트, 인공신경망, 조류, 에크만취송류

학번: 2010-31101